

https://dspace.org/

On the toughening mechanisms present in boron suboxide materials with sintering aids.

Bush, Peter Robert

2011-10-06
http://hdl.handle.net/10539/10492

Downloaded from a DSpace repository. https://dspace.org/

On the Toughening Mechanisms Present in Boron Suboxide Materials with Sintering Aids

Peter Robert Bush

A dissertation submitted to the Faculty of Engineering and the Built Environment, University of the Witwatersrand, Johannesburg, in fulfilment of the requirements for the degree of Master of Science in Engineering.

May 2011

Declaration

I declare that this dissertation is my own unaided work. It is being submitted to the degree of Master of Science in Engineering to the University of the Witwatersrand, Johannesburg. It has not been submitted before for any degree or examination to any other University.

Peter Robert Bush

---------- day of ---------- 2011

Extracts from this body of work have been presented at:

- Sigalas, I., Johnson, O.T., Bush, P. and Freemantle, C. Boron suboxide composites: Thermal stability and tribological assessment. 12th International Ceramics Conference (Cimtec, Montecatini Terme, Italy) 6-11 June 2010
- Sigalas, I., Johnson, O.T., Bush, P. and Freemantle, C. Boron suboxide composites: Recent developments. 5th International Workshop on Spinel Nitrides and Related Materials (Rüdersheim/Rhine, Germany). 29 August – 3 September 2010.

Abstract

The fracture toughness of polycrystalline boron suboxide has been substantially improved through the addition of a low amount of various sintering aids Determining the reasons behind the small amount of secondary phase increasing the toughness of boron suboxide to such an extent was the focus of this project.

Fracture toughness testing was conducted on pure boron suboxide and boron suboxide containing CaO, NiO, Y_2O_3-Al_2O_3 TiB_2-Y_2O_3-Al_2O_3 additions. Determining the fracture toughness through the SEVNB, IFT and COD methods, it was shown that these additives increase the toughness of boron suboxide significantly. Additionally, hardness testing of pure boron suboxide revealed a significant indentation size effect.

Analysis of crack interaction with the microstructure was performed. Insufficient mechanical toughening events were observed to explain the increase in fracture toughness. Although the mechanism behind the increase in fracture toughness was not discovered, it was concluded that the sintering aids must change the surface energy of the boron suboxide matrix.

Acknowledgements

I would like to acknowledge the following people for the valuable contributions which facilitated the completion of this research work.

i. Professor Sigalas, for overseeing this body of research
ii. Doctor Herrmann, for his contributions to this body of work
iii. Element Six (PTY) Ltd. for their financial support
iv. DST/NRF Centre of Excellence in Strong Materials for their financial support
v. The staff at Element Six (PTY) Ltd. who assisted in this project, namely, Dr. T. Heiligers, Dr. F. Van Staden, Mr. R. Cruz and Mr. S. Masete
vi. Mr. O.T. Johnson for his assistance in obtaining decent SEM images
vii. The support staff in the School of Chemical and Metallurgical Engineering, especially Mr. A. Xoseka and Mr. B. Mothebeli, for their technical assistance
viii. My family and friends for their patience and understanding during this period

Contents

Declaration ..... **i**

Abstract ..... **ii**

Acknowledgements ..... **iii**

List of Figures ..... **vii**

List of Tables ..... **x**

List of Symbols ..... **xii**

1.0 Introduction & Motivation **1**

2.0 Literature Survey **3**

2.1 Super hard materials 3

2.2. Structure of boron suboxide 5

2.3. Synthesis 10

2.4. Sintering 17

2.4.1 Pure boron suboxide 17

2.4.2. Composites 18

2.5 Thermodynamics of boron suboxide 25

2.5.1 Enthalpy and heat capacity 25

2.5.2 Static interactions with CGI 27

2.5.3 Oxidation resistance 29

2.6. Hardness 31

2.6.1. Hardness testing 31

2.6.2. Hardness of boron suboxide 33

2.7. Fracture Toughness 35

2.8. Toughening of ceramics 38

2.8.1 Crack deflection 40

2.8.3 Zone shielding 42

2.8.4 Contact shielding 44

3.0 Experimental Procedure **46**

3.1 Introduction 46

3.2 Hot press runs 46
3.2.1 Capsule assembly 47
3.2.2 Densifying boron suboxide powder 48
3.3 Materials to be tested 49
3.4 Production of boron suboxide discs by SPS/FAST technology 50
3.5 LASER cutting 52
3.6 Lapping and grinding 54
3.7 Grinding and polishing 56
3.8 Density and Porosity 57
3.9 Microscopy 60
3.10 XRD analysis 61
3.11 Hardness Testing 61
3.12 Indentation size effect 63
3.13 Indentation fracture toughness 64
3.14 Distinguishing the crack regime 69
3.15 Crack opening displacement analysis 72
3.16 Single-edge-V-notch beam test 75
3.17 Introducing the V-notch 78
4.0 Results 80
4.1 Introduction 80
4.2 Analysis of hot pressed boron suboxide materials 80
4.2 Analysis of Spark Plasma Sintered samples 82
4.2.1 Density 82
4.2.2 Phase analysis of samples 84
4.3 Indentation Size Effect 89
4.3.1 Hardness Measurements 89
4.3.2 Meyer's law 90
4.4 Hardness of SPS densified materials 93
4.5 Crack regime 94
4.6 Indentation fracture toughness 95
4.7 SEVNB 97
4.8 Mode of failure 98
4.9 Crack opening displacement analysis 101
4.10 Toughening mechanisms 102

4.10.1 Angles of crack deflection 103
4.10.2 Distance between toughening events 105
5.0 Discussion 107
5.1 Introduction 107
5.2 Densification 107
5.3. Hardness 113
5.3.1 Hardness of boron suboxide materials with additives 113
5.3.2 Indentation size effect 115
5.4 Comparison of fracture toughness data 118
5.5 Toughening mechanisms 127
5.5.1 Crack branching 128
5.5.2 Crack deflection 131
5.5.3 Crack bridging 140
5.5.4 Frictional toughening 142
5.5.5 Transformation toughening 143
5.5.6 Crack arrest 143
5.5.7 Surface Energy 145
6.0 Conclusions and Recommendations 154
References 156
Appendix A 167
Appendix B 172
Appendix C: 189

List of Figures

Figure 2-1: Rhombohedral cell of boron suboxide. (Hubert (1998))..... 6
Figure 2-2: Electron density map for boron suboxide (calculated) Letsoabe, Lowther (2008)..... 7
Figure 2-3: Occupancy of the 6c position in B_6O by oxygen. From Lundström (1997)..... 8
Figure 2-4: Indented apex, indicative of twinning, observed by Hubert et al (1997) 10
Figure 2-5: (a) SEM of B_6O platelets (Yu (2010))(b) a cross-section of a nanowire with the proposed star geometry (Jiang (2006)); (c) a schematic of the cross-section showing the planes of twinning (Jiang (2006)) 16
Figure 2-6: Densification of boron suboxide during hot pressing and reactive sintering (indicated by a *). Figure from Brodhag, C et al (1986)..... 18
Figure 2-7: The effect of alumina on the fracture toughness and hardness of boron suboxide. Taken from Kleebe et al (2008)..... 22
Figure 2-8: TEM images showing the clean interface between grains (a) (Andrews (2008)) and the multiple twinning within the B6O grains (b) (Shabalala et al (2008))..... 23
Figure 2-9: Hardness and fracture toughness values for various B_6O composites (Johnson (2008) and Ogunmuyiwa (2009))..... 24
Figure 2-10: A B_6O-TiB_2 (without yttria additions) composite showing the TiB_2 grains (light phase) and partial removal of oxide grain boundary (Herrmann et al. (2009))..... 25
Figure 2-11: Standard enthalpy of formation as a function of atomic radius of X species in B_6X (Makarov and Ugai (1986))..... 26
Figure 2-12: The effect of temperature upon heat capacity for B_6Si, B_6O (extrapolated experimental) and for B_6O after correction. (Andrews (2008))..... 27
Figure 2-13: The B-O-Fe ternary phase diagram calculated for 700°C (Freemantle (2009))..... 28
Figure 2-14: Optical micrographs after 10 hours of heat treatment. A and B are from the pure B_6O sample. C and D are from the B_6O-Al_2O_3-Y_2O_3 sample. Freemantle (2009)..... 30
Figure 2-15: Temperature (a) and kinetic (b) curves for the reaction of powdered boron suboxide (1) and boron (2) under isothermal conditions at 900 (3), 800 (4) and 700°C (5) (Karlamov (2002))..... 31
Figure 2-16: Effect of load on microhardness (Stevenson et al (2002))..... 32
Figure 2-17: Hardness against load for various ceramics (Ellison-Hayashi (US

Patent 5330937)) 35
Figure 2-18: Modes of failure: I: Opening, II: Sliding III: Shear (Atkinson (1995)) 37
Figure 2-19: The three types of toughening mechanisms (Steinbrech (1992)) 40
Figure 2-20: Ductile bridging in the wake of a crack (Evans (1990)) 44
Figure 2-21: Ligaments toughening a brittle ceramic by frictional action. (Roesler (2007)) 45
Figure 3-1: Capsule assembly and punch and die configuration 48
Figure 3-2: Schematic drawing of an SPS configuration (Hungria et al. (2009)). 51
Figure 3-3: Schematic of the layout of the rectangular bars as cut out of the composite discs 53
Figure 3-4: Schematic of the layout of the rectangular bars as cut out of the pure B_6O discs 54
Figure 3-5: Schematic of arrangement used for lapping 55
Figure 3-6: An indentation, showing measured dimensions for IFT 65
Figure 3-7: (a) Half-penny and (b) Palmqvist cracks as introduced by a Vickers indenter 69
Figure 3-8: Schematic of an indentation showing measured dimensions for COD analysis 73
Figure 3-9: An approximation of the diagonal lengths for indent in pure boron suboxide 74
Figure 3-10: Schematic of SEVNB testing layout 77
Figure 4-1: XRD trace of B_6O (HP1) 81
Figure 4-2: Structure (a,b), accompanying EDS spectrum (c) and XRD trace of pure B_6O. EDS spectrum mapped image b. 84
Figure 4-3: Structure (a,b), accompanying EDS spectrum (c) and XRD trace of B_6O-Y_2O_3-Al_2O_3-TiB_2. EDS spectrum mapped image b. 85
Figure 4-4: Structure (a,b), accompanying EDS spectrum (c) and XRD trace of B_6O-CaO. EDS spectrum mapped image b. 86
Figure 4-5 Structure (a,b), accompanying EDS spectrum (c) and XRD trace of B_6O-NiO. EDS spectrum mapped image b 87
Figure 4-6: Structure (a,b), accompanying EDS spectrum (c) and XRD trace of B_6O-Y_2O_3-Al_2O_3. EDS spectrum mapped image b. 88
Figure 4-7: Effect of load on the measured diagonal length during hardness testing 91
Figure 4-8: Effect of load on the measured Vickers hardness of hot-press, pure B_6O 92
Figure 4-9: An indentation in Y_2O_3-Al_2O_3-B_6O before (a) and after (b) polishing. The white arrows indicate where the cracks are still attached indentation. 95
Figure 4-10: Optical image of a B_6O-NiO sample after SEVNB testing. The height of the sample is 4mm. 98
Figure 4-11: SEM images of the fracture surfaces of (a) pure B_6O; (b) B_6O – NiO;

(c) B_6O-Y_2O_3-Al_2O_3; (d) B_6O-CaO and (e) B_6O – Y_2O_3 - Al_2O_3 – TiB_2 100
Figure 4-12: COD analysis for pure boron suboxide 101
Figure 4-13: Crack deflection angles for the various boron suboxide based materials 103
Figure 4-14: Crack deflection angles from Figure 12, redrawn between 15 and 45° 104
Figure 5-1: Comparison of the hardness of the SPS sintered boron suboxide materials 114
Figure 5-2: Fracture toughness data for pure boron suboxide with and without different sintering additives. Note that pure B_6O was tested under a 1kg load .. 119
Figure 5-3: SEVNB fracture toughness of boron suboxide materials as a function of additive content 121
Figure 5-4: Effect of open porosity upon the COD measurements deviation from SEVNB measurements 123
Figure 5-5: Schematic of trend of the effect of Y_2O_3-Al_2O_3 content upon the fracture toughness of boron suboxide materials. (Herrmann (2010)) 126
Figure 5-6: Crack branching in the B_6O-Al_2O_3-Y_2O_3-TiB_2 sample 130
Figure 5-7: Crack deflection around a pore in pure boron suboxide 132
Figure 5-8: Crack deflection density for the boron suboxide materials 133
Figure 5-9: A crack running through the B_6O-Y_2O_3-Al_2O_3-TiB_2 sample. The red arrows indicated where the crack has sheared a TiB_2 grain. 135
Figure 5-10: Crack bridging in (a) the B_6O-Y_2O_3-Al_2O_3-TiB_2 and (b) B_6O-Y_2O_3-Al_2O_3 composites 141
Figure 5-11: Crack arrest by a pore in pure boron suboxide 145
Figure 5-12: Illustration of a transgranular crack deflecting along a twin plane 147
Figure 5-13: Lattice parameter plot of the various boron suboxide materials, boron and boron carbide 150
Figure 5-14: Figure 5-12 redrawn, excluding boron and boron carbide 150
Figure 5-15: c to a ratio for the boron based materials. 152
Figure B1: COD analysis for B_6O-Y_2O_3-Al_2O_3 185
Figure B2: COD analysis for B_6O-NiO 186
Figure B3: COD analysis for B_6O-CaO 187
Figure B4: COD analysis for theTiB_2-Y_2O_3-Al_2O_3 –B_6O composite. $K_{Ic,\ COD}$ = 2.8MPa.$m^{0.5}$ 188

List of Tables

Table 2-1: Previously recorded hardness values of boron suboxide 34
Table 3-1: Samples examined for fracture toughness experiments 49
Table 3-2: Grinding and polishing conditions 56
Table 3-3: Density of individual phases present in sintered discs 59
Table 3-4: Theoretical densities of each of the samples. Includes 1.5wt% B_2O_3 . 60
Table 3-5: Elastic moduli of boron suboxide materials 68
Table 4-1: Density and porosity of hot pressed boron suboxide materials 81
Table 4-2: Density and porosity of the samples received from the IKTS 83
Table 4-3: Hardness measurements for hot-pressed pure boron suboxide 90
Table 4-4: Vickers hardness for the spark plasma sintered boron suboxide materials 93
Table 4-5: Fracture toughness of boron suboxide materials, determined by the IFT method 96
Table 4-6: Fracture toughness of boron suboxide materials, as determined by the SEVNB method 97
Table 4-7: Fracture toughness of boron suboxide materials, determined by the COD method 102
Table 4-8: Distance between toughening events in boron suboxide based materials 106
Table 5-1: Comparison of hardness values of literature and this study for pure B_6O 117
Table 5-2: Data used for calculation of residual stress in the composites 137
Table B1: Hardness vales and diagonal lengths for hot-pressed pure boron suboxide under a 100g load 172
Table B2: Hardness vales and diagonal lengths for hot-pressed pure boron suboxide under a 200g load 173
Table B3: Hardness vales and diagonal lengths for hot-pressed pure boron suboxide under a 300g load 173
Table B4: Hardness vales and diagonal lengths for hot-pressed pure boron suboxide under a 500g load 174
Table B5: Hardness vales and diagonal lengths for hot-pressed pure boron suboxide under a 1kg load 174
Table B6: Hardness vales and diagonal lengths for hot-pressed pure boron suboxide under a 2kg load 175
Table B7: Hardness measurements for pure boron suboxide 176
Table B8: Hardness and IFT measurements for B_6O – 1.16NiO 176

Table B9: Hardness and IFT measurements for B_6O – 1.13CaO 177
Table B10: Hardness and IFT measurements for B_6O – 1.54Y_2O_3 – 1.45Al_2O_3 177
Table B11: Hardness and IFT measurements for B_6O – 1.57Y_2O_3 – 1.49Al_2O_3 – 18.69TiB_2 178
Table B12: SEVNB data for pure B_6O 179
Table B13: SEVNB data for B_6O – 1.54Y_2O_3 – 1.45Al_2O_3 180
Table B14: SEVNB data for B_6O – 1.57Y_2O_3 – 1.49Al_2O_3 – 18.69TiB_2 181
Table B15: SEVNB data for B_6O – 1.13CaO 182
Table B16: SEVNB data for B_6O – 1.16NiO..... 183

List of Symbols

a –Radial-median crack length (μm)

A –Notch length (mm)

α – Thermal expansion coefficient (K^{-1})

B – Specimen breadth (mm)

c – Radial crack length (μm)

CL – SEM image taken in cathodoluminescene mode

δ – Crack opening displacement (nm)

d –Length of indentation diagonal (μm)

E – Young's modulus (GPa)

V – Volume fraction

F – Fracture load (MN)

H_v – Vickers hardness (GPa)

KIc – Fracture toughness ($MPa.m^{0.5}$)

KIc,IFT – Fracture toughness determined by the indentation method ($MPa.m^{0.5}$)

KIc,SEVNB – Fracture toughness determined by the SEVNB method ($MPa.m^{0.5}$)

KIc,COD – Fracture toughness determined by the COD method ($MPa.m^{0.5}$)

L – Specimen length (mm)

m_a – Apparent mass (g)

m_d – Dry mass (g)

m_w – Saturated mass (g)

ρ – Density (g/cm^3)

P – Applied load (N)

P_o – Open porosity (%)

S – Support span (mm)

SE – SEM image taken in secondary electron mode

σ – Applied stress (MN)

T – Temperature (K)

θ – Indenter angle (°)

ν – Poisson’s ratio

W – Specimen width (m)

Y – Stress intensity factor

x –Distance from indentation crack tip (μm)

§ – Material constant for Vickers induced indentation cracks

1.0 Introduction & Motivation

Diamond and cubic boron nitride are the current super-hard materials used for industrial applications. However, the main method for the manufacture of diamond and cubic boron nitride utilises ultra-high temperature and pressure, which renders the manufacture of these materials expensive. Furthermore, the stability of these materials decreases at elevated temperatures. Diamond has the additional problem of being unable to machine ferrous alloys at elevated temperatures due to diffusional wear (Loladze, (1981)). These problems with the current super-hard materials have stimulated research into finding a new super-hard material for industrial applications.

Boron suboxide has been found to possess properties that indicate that it could potentially be used as an industrial super-hard material. Single crystal boron suboxide has a hardness of 45GPa ($Hv_{0.1}$) and a fracture toughness of 4.5MPa.$m^{0.5}$ (He *et al*. (2002)), comparable with the hardness and fracture toughness of cubic boron nitride (60GPa and 2.8MPa.$m^{0.5}$ respectively). However, the polycrystalline materials of pure boron suboxide have been found to fracture in a very brittle fashion. The toughness of polycrystalline boron suboxide has been improved by the work of Shabalala (2008), Andrews (2008), Johnson (2008) and Ogunmuyiwa (2009), which produced various boron suboxide composites. However, the reasons behind the improved toughness of the composites have never been fully explained.

The aim of this project was to explain the reasons behind the increase in fracture toughness of the boron suboxide composites compared to pure boron suboxide. The toughness of various boron suboxide composites, as well as pure boron suboxide were be determined by three methods, including a standard testing method. The reasons for the toughening was examined in terms of the interaction of crack with the microstructure of the boron suboxide material.

A detailed literature review on the previous developments of boron suboxide is presented in Chapter 2.

Chapter 3 describes the techniques and equipment used to accomplish the aim of this project.

Chapter 4 presents the results obtained using the techniques discussed in Chapter 3.

Chapter 5 discusses the results and explains the toughening behind the boron suboxide composites.

The conclusions of this projects and recommendations for further bodies of work are presented in Chapter 6.

2.0 Literature Survey

2.1 Super hard materials

The majority of researchers accept that the minimum criterion for a material to be classified as super-hard is to have a hardness value higher than 40GPa (Sung *et al*. (1995)). Industrially, super-hard materials are used in applications where resistance to abrasive wear is important. These applications include grinding media, cutting tools and wear parts.

Hardness of a material is a measure its ability to resist plastic deformation (Dieter (1976)). Many factors are responsible for a material's hardness. The material's resistance to volume compression, resistance to shearing and the resistance to deformation due to the formation and interactions of dislocations, and in ceramics, microcrack formation all play a role. Hence, a hard material would have a high bulk modulus and a high shear modulus.

Another way of viewing the factors affecting hardness is that a hard material must have a three dimensional dense network of bonds of short length and high strength. Covalent bonds are the strongest bonds in nature; these bonds exist

between Group IV elements (such as C, Si, Ge). Short bond lengths exist between the lighter elements (B, C, N, O). It is for this reason that much research into hard materials has been focused on the lighter elements (Veprek (1999), He et al. (2002)).

The super-hard materials made from these light elements also exhibit the highest strength in compression, thermal conductivities and acoustic wave velocities. They also exhibit high chemical inertness and low thermal expansion and mechanical friction coefficients (Sung *et al*. (1995)).

Examples of super-hard materials made from the lighter elements are diamond and cubic boron nitride (cBN). Diamond is reported to have a hardness value between 70 and 100GPa and a fracture toughness of 5.0MPa.$m^{0.5}$. Cubic boron nitride is reported to have a hardness around 45GPa (Brookes (1986)), and a fracture toughness of 2.8MPa.$m^{0.5}$.

The boron family of compounds (of which cBN is a prominent member) is of particular interest for various reasons. Boron is able to form covalent bonds with many elements, which as discussed above is one of the requirements of producing super-hard materials. Boron is also able to form hard materials with many of the transition elements. Boron has several existing hard phases, such as boron carbide

(B_4C) and boron suboxide (B_6O), as well as several proposed phases, such as B_2O, BCN and BC_2N(Itoh (2004)).

Recently however, single crystalline boron suboxide, with hardness values up to 45GPa and fracture toughness values up to 4.5MPa.$m^{0.5}$, has been found to display properties which may classify the material as superhard. (He *et al*. (2002)) This has led to the belief that boron suboxide composites may be another potential industrial wear resistant material.

2.2. Structure of boron suboxide

The structure of boron compounds B_6O, B_4C and B_6P, as well as elemental boron are based upon the icosahedron unit cell (King (1992)). The icosahedra of both boron suboxide and boron carbide form an α-rhombohedral structure group ($R\bar{3}m$ spacegroup) which comprises twelve boron atoms occupying the vertices of the rhombohedral, this is shown in Figure 2-1. In boron suboxide, two oxygen atoms are accommodated along the main diagonal. Hence, boron suboxide has the structural formula of $B_{12}O_2$ (Kawai *et al*. (1990)).

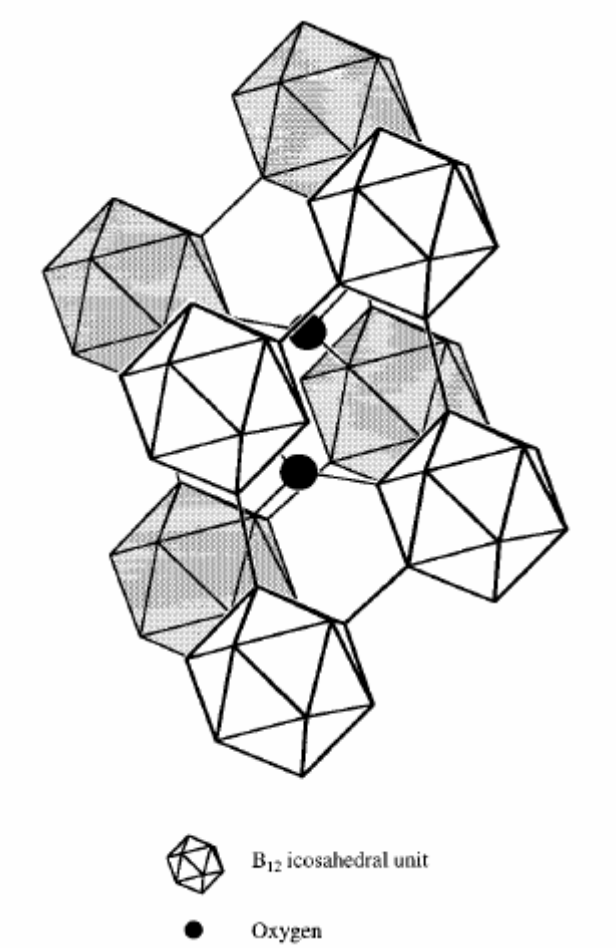


Figure 2-1: Rhombohedral cell of boron suboxide (Hubert (1998))

Performing Rietveld refinement on boron suboxide, Bolgrem (1991) determined the hexagonal cell parameters of boron suboxide to be a = 5.366Å and c = 12.331Å, with the distance between the central oxygen atoms being 3.06Å. The distance between oxygen atoms was confirmed by Kawai *et al*. (1990) using $K\alpha$ x-ray emission spectroscopy.

Theoretical calculations performed by Lee *et al*. (1991) and later Letsoala and Lowther (2008) sought to determine the atomic position of the unit cell by altering cell parameter until a minimum energy was established. In both cases, the oxygen atoms were found to be non-bonding. Figure 2-2 is a calculated electron density map, which shows the lack of interaction between the oxygen atoms. The plane of the density map was chosen such that it would intercept the two oxygen atoms of the same boron suboxide unit cell. Lee *et al*. determined the lattice constant to be 9.709Å. Letsoabe and Lowther determined the a and c dimensions to be 5.392 Å and 12.121Å respectively. The difference between the calculate values and experimental data was due to non-stoichiometry of oxygen in the B_6O unit cell.

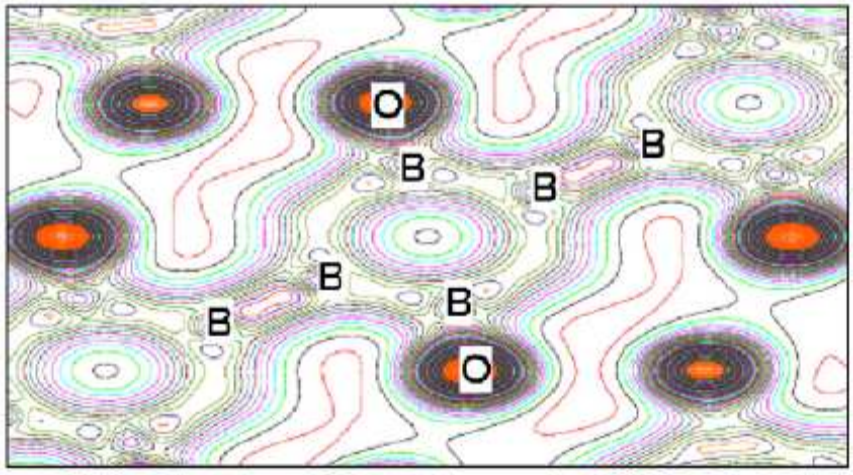


Figure 2-2: Electron density map for boron suboxide (calculated) Letsoala and Lowther (2008)

Work done by Lundström (1997) on the synthesis of boron suboxide with various forms of boron powder (notably, amorphous and α-rhombohedral), showed that

the occupancy of the 6c position by oxygen decreases with increasing temperature. The trend of oxygen stoichiometry with reaction temperature is displayed in Figure 2-3. This shows that there is a solubility range for oxygen occupancy in boron suboxide. The work of Lundström, however was conducted using two phases of boron as starting material: ex-iodide amorphous and α-boron. It is not clear how the change in the starting material could alter the occupancy of the 6c position in boron suboxide.

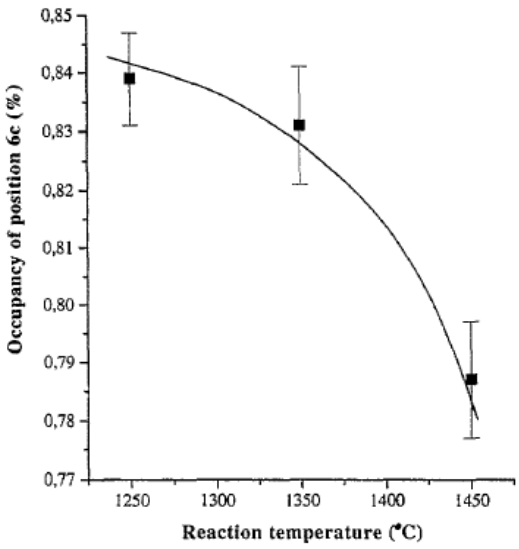


Figure 2-3: Occupancy of the 6c position in B_6O by oxygen. From Lundström (1997)

Earlier work by Lundström and Andreev (1996) showed that there was a high concentration of vacancies at the oxygen position in B_6O_{1-x}, where "x" is in the range of 0.16-0.24. They concluded that stoichiometric B_6O could only be prepared at elevated pressures. Boron suboxide formed at ambient pressures not

only suffered from oxygen deficiency, but also from poor crystallinity and small grain size (less than 4μm).

McMillan *et al*. (1999) reported that synthesising at high pressures results in higher crystallinity. At a pressure of 4-5.5GPa, they reported achieving perfect icosahedral crystals (of about 40μm in size), while maintaining the $R\bar{3}m$ space group. This is almost contradictory, they reported, as the $R\bar{3}m$ space group does not allow for the five fold symmetry that icosahedra have. They attempted to explain this by using Mackay packing. In Mackay packing, successive layers of atoms are assembled around a central icosahedron. This method of packing does not produce a close packed structure, with the atoms on the triangular face separated by 1.05 times their diameter. McMillan *et al*. believed that Mackay packing is possible in B_6O as the oxygen would act as spacers in the boron structure. This is only possible with higher oxygen activities, which occur at higher pressures.

Hubert *et al*. (1997) showed that boron suboxide has the propensity to twin. Twinning occurs along a parallel set of planes or along the {100} plane. However, twinning along non-parallel planes is never observed. Similar twinning is observed in boron carbide.

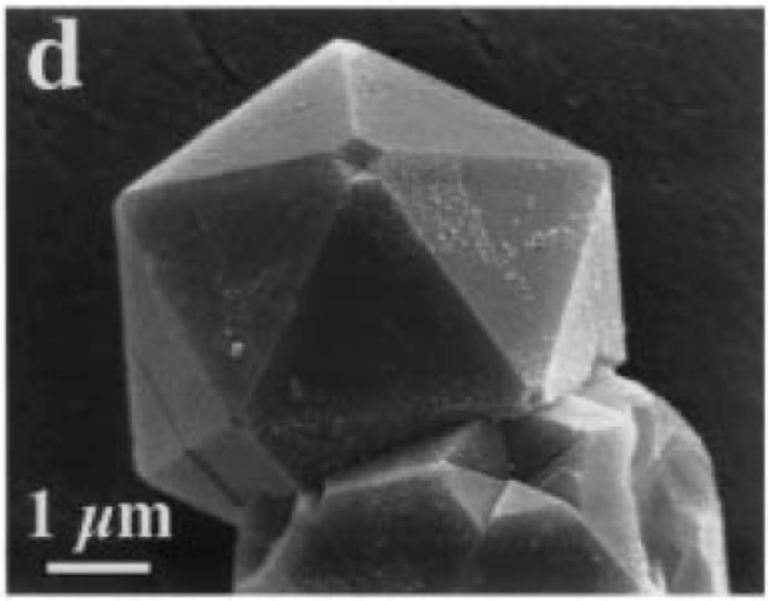


Figure 2-4: Indented apex, indicative of twinning, observed by Hubert *et al.* (1997)

He, Shieh and Duffy (2004) studied the properties of boron suboxide when subjected to nonhydrostatic compression in a diamond cell. By analysing the radial x-ray diffraction, they were able to determine that boron suboxide has a bulk modulus of 270 ± 12GPa, which approaches that of cBN (360GPa) and diamond (440GPa).

2.3. Synthesis

Boron suboxide is produced mainly through two techniques: the reaction of boron with boron oxide (B_2O_3) and the reaction of boron with a metal oxide. These techniques are discussed below.

U.S. patent 3,660,031 (Holcombe, Jr. *et al*. (1972)) discloses a method to prepare boron suboxide (reported as B_7O) by reacting elemental boron with zinc oxide, between the temperatures of 1200° and 1500°C. The material is recorded as having a high refractivity and small grain size (~1μm). Although no fracture toughness value is reported, hardness of 38.20GPa (under a 100g load) and a density of 2.60g/cm^3 is reported. The reaction of boron powder with zinc oxide powder is:

$$ZnO + B \rightarrow B_6O + Zn \qquad \textbf{Equation 2-1}$$

Elemental boron is mixed with the metal oxide powder. The blended powder is then placed in a refractory vessel and heated to 1200°-1500°C under flowing argon, helium or vacuum (Holcombe *et al*. (1972)). This method is claimed to work for powder blended in stoichiometry or with excess boron with only a slight reduction in the properties of the final product (Holcombe *et al*. (1972)). However, it is doubtful that stoichiometry was achieved in the initial reports of boron suboxide synthesis.

Apart from zinc oxide, various metal oxides have been reported to be successful in the synthesis of boron suboxide including; MgO, CdO, SnO, Ga_2O_3 (Brodhag *et al.* (1986)), CrO_3, $KClO_3$ and CuO, Bi_2O_3 and In_2O_3 (Olofsson *et al*. (1997)). Zinc oxide has been proven to offer the best results (Liu *et al*. (1995)). The

temperature of this synthesis ranges from 1200°C to about 2000°C. Olofsson and Lundström (1997) report that attempts at synthesis below about 1250°C are likely to be unsuccessful due to reduced reaction rates.

Oxides such as CrO_3, $KClO_3$ require higher pressures to promote Equation 2-2 (Liu *et al*. (1995)).

$$CrO_3 + B \rightarrow B_6O + Cr_2O_3 + O_2 \qquad \textbf{Equation 2-2}$$

However, there is a problem controlling the pressure when a gaseous phase (O_2) is released. MgO is reported to form magnesium boride, reducing the amount of boron free to form boron suboxide (Liu *et al*. (1995)). There is contention as to whether Ga_2O_3 also forms a boride or not. Liu *et al*. (1995) report that it does not, while Brodhag and Thevenot (1986) reports that it does.

In the production of B_6O through a metal oxide, zinc oxide has gained acceptance as the oxide to use in this route, due to the ease with which the undesired products and reactants can be removed.

The zinc is removed from the crucible in the gaseous form, while the zinc oxide and excess boron powder can be removed by washing in hydrochloric acid. Furthermore, at the temperatures of the reaction, zinc oxide is a liquid phase,

which would increase the rates of reaction via increased mass transport rates (Liu *et al.* (1995)).

The synthesis of boron suboxide by use of zinc oxide can be performed either at low pressure (even ambient) (Holcombe *et al*. (1972) and Liu *et al*. (1995)), or at higher pressures (about 3.5GPa) (Kayhan and Inal (1999)). However, if the synthesis occurs at higher pressures, then the die must be faced with hBN to prevent contamination of the powder.

The second route for production of boron suboxide (reported as B_6O) is disclosed in U.S. patent 5,330,937 (Ellison-Hayashi *et al*. (1994)). This method produces boron suboxide by reacting elemental boron with boron oxide (B_2O_3), between 1900° and 2100°C, under a pressure of between 3000 and 4000 psi. The grain size of the resulting boron suboxide is reported as less than 5μm. Hardness values of at least 38GPa and typically 42.5GPa were recorded. No fracture toughness values were recorded. This method produces a sintered compact which must then be ground to powder.

It is possible to produce powder directly through the reaction of boron with boron oxide (B_2O_3). In this method, the two powders are blended and allowed to react under an inert atmosphere (argon or helium) between 1000-2000°C (Oloffson and Lundstrom (1997)). The following reaction ensues:

$$16B_{(s)} + B_2O_3 \rightarrow 3B_6O$$ **Equation 2-3**

Boric acid has been successfully used in the place of B_2O_3. Typically, excess boric acid is used in the synthesis to correct for losses due to the evaporation of HBO_2. This method has similar advantages as compared to the synthesis with zinc powder. Since boron oxide melts around 450°C, it increases the kinetics of the overall reaction. Further, any residual reactants can be removed by washing in dilute hydrochloric acid or ethanol (Shabalala *et al*. (2008)).

In this method, either amorphous or crystalline boron can be used, with varying effects on the properties of the end powder. Olofsson and Lundström (1997) studied the effect on the choice of boron morphology on the reaction using amorphous boron and α-rhombohedral. It was found that the alpha rhombohedral boron resulted in better crystallinity of the samples (Lundström (1997)). However, due to the lower reactivity of α-boron as compared to amorphous boron, the reaction time increases dramatically. For example, at 1450°C, it was required to sinter for 100 hours before a homogeneous phase was established (Olofsson and Lundström (1997)).

In 2000, Yu *et al*. showed that nanostructured films of boron suboxide could be deposited on various substrates. Prepared boron suboxide sintered compacts were

placed upon Si (100) or graphite surfaces. Pulsed laser deposition at 200MJ under varying pressures was used to deposit the boron suboxide on the substrate. A near homogenous distribution of nano-clusters of boron suboxide resulted. Some of the clusters were as large as 500nm. It was observed that the larger particles tended to form polymorphic regular shapes, for example, decahedra.

If the synthesis of boron suboxide is conducted at high pressures, then the oxygen stoichiometry, grain size and crystallinity of B_6O_{1-x} improves (McMillan *et al*. (1999)). Hubert *et al*. (1998) achieved a maximum grain size of 40μm with an oxygen stoichiometry of "x"=0.04, while He *et al*. (2002) achieved a maximum grain size of 100μm by seeding a B_2O_3 melt with B_6O crystallites.

The achievement of He *et al*. (2002) in producing a grain size of 100μm meant that single crystal properties could be measured. These crystals were synthesised at 2100°C under 5.5GPa for 60 minutes. The stoichiometry of the crystals was determined to be $B_6O_{0.98}$. The fracture toughness of single crystal boron suboxide is reported as 4.5MPa.$m^{0.5}$ and the hardness as 45GPa. This is comparable to diamond's fracture toughness of 5.0MPa.$m^{0.5}$ and cubic boron nitride's hardness of 60GPa The fracture toughness is significantly higher than cBN's fracture toughness of 2.8MPa.$m^{0.5}$ (Sung *et al*. (1996), Brookes (1986)).

Cao *et al*. (2006) synthesized boron suboxide platelets and nanowires by reacting a mixture of $B_{(am)}$, Fe_3O_4 and CaO at 1450°C for four hours. The Fe_3O_4 to CaO ratio determined whether platelets or nanowires were produced. The nanowires diameter ranged between 50 and 300nm and had a reported length of tens of microns. Cao proposed that the growth mechanism was related to the conventional vapour-liquid-solid growth mechanism, where the Ca-B-O system can form vapours which deposit onto the Fe catalyst. This argument was supported by the presence of a line of Fe within the grains.

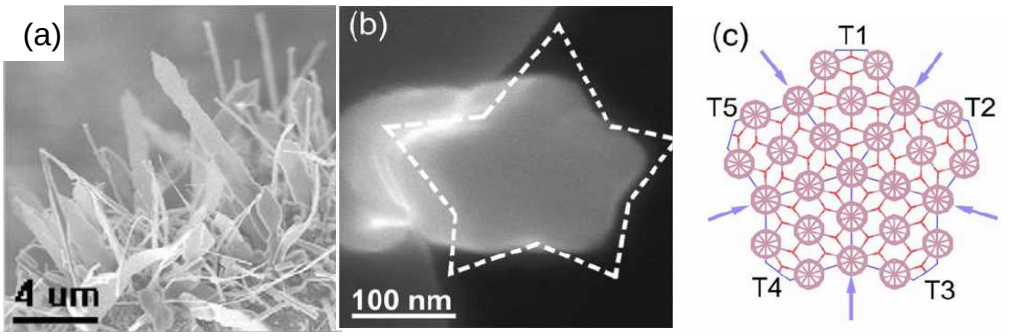


Figure 2-5: (a) SEM of B_6O platelets (Yu (2010))(b) a cross-section of a nanowire with the proposed star geometry (Jiang (2006)); (c) a schematic of the cross-section showing the planes of twinning (Jiang (2006))

Using a high resolution transmission electron microscope (HRTEM), Yu *et al*. (2010) examined the growth mechanism of the platelets reported by Cao *et al*. Normally, in the $R\bar{3}m$ spacegroup which is characteristic of B_6O materials, it would not be possible to form platelets as growth along the [100] planes must be retarded. Yu *et al*. observed that the [100] planes was extensively twinned. These

twins are likely to induce anisotropic growth of the platelets as preferred nucleation and growth occurs along the twin-plane re-entrant grooves (Figure 2-5 (c)).

Continuing the work of Cao *et al*., Jiang *et al*. (2006) examined the structure of the B_6O nanowires. Figure 2-5 (b) shows the head of the nanowire, which has a star shaped morphology. This was attributed to a five-fold cyclic twinning along the {100} planes. The misfit along the twin boundaries could be as low as 1°. Jiang *et al*. believe that the nanowires have potential uses as nanoabrasives or use in nanoelectromechanical systems.

2.4. Sintering

2.4.1 Pure boron suboxide

Brodhag *et al*. (1986) investigated the densification behaviour of boron suboxide. The starting powder for the densification experiment was either a mixture of boron and boron anhydride (for reactive sintering) or pre-produced boron suboxide powder. The pre-produced boron suboxide powder was produced by the borothermic reduction of ZnO. A boron nitride layer was used to limit the carbon diffusion into the powder from the graphite dies. Three major densification peaks were observed during sintering, as shown in Figure 2-6.

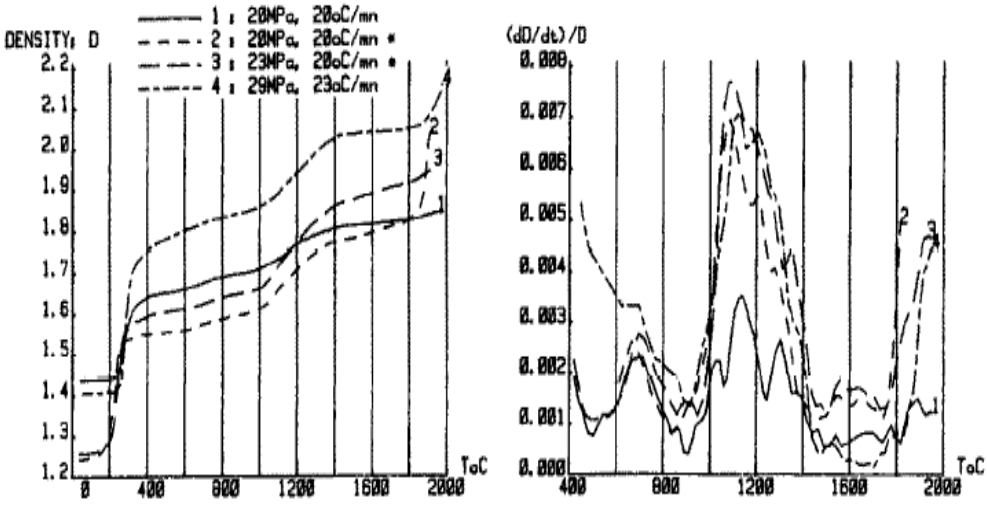


Figure 2-6: Densification of boron suboxide during hot pressing and reactive sintering (indicated by a *). Figure from Brodhag *et al*. (1986)

The first peak is a result of the melting of B_2O_3 and the resulting liquid penetration into the compact. The second peak at about 1200°C is a result from the initiation of the reaction, while proper sintering begins after 1800°C. An important outcome of this experiment is that boron suboxide does not sinter below about 1800°C.

2.4.2. Composites

In 2000, Itoh *et al*. investigated the possibility of a new phase being formed when B_6O-B_4C were sintered compacts at high temperature and pressure. The boron suboxide was prepared by reacting amorphous boron with boron oxide. The boron

carbide was commercially available. The boron suboxide was mixed 0-40vol% boron carbide and then degassed. The mixed powders were sintered at 1500 -1800 °C under a pressure of 4-7GPa. The lattice parameters for B_6O and B_4C were constant throughout the sintering, indicating that no new compounds were formed. The composite B_6O-B_4C was found to have a hardness of 43GPa and a fracture toughness of 1MPa.$m^{0.5}$ when sintered at 1800°C. It was found that the fracture toughness resulted in crack deflection along the B_4C-B_6O interface. This implies that the fracture toughness increases with increasing B_4C content.

In 2001, Sasai *et al*. investigated the properties of diamond-B_6O mixtures. The boron suboxide was prepared by the reaction of amorphous boron with boron oxide. The boron suboxide was then mixed with 0-40vol% diamond powder and the resulting powder was degassed. The mixture was treated under 3-5GPa at 1400-1800°C for 20 minutes. Part of the diamond changes form into diamond-like carbon. Depending on the size and amount of the diamond additions, the resulting compact either had diamond as the matrix and B_6O as the second phase or B_6O as the matrix and diamond as the second phase. The hardness of the compacts increased with increasing pressure and temperature. The hardness depended upon the amount and dispersion of the diamond particles and a maximum hardness of 60GPa was achieved. However, the fracture toughness never exceeded 1MPa.$m^{0.5}$.

Kayhan and Inal (1999) prepared boron suboxide compacts through a variety of techniques. The boron suboxide that they used for their experiment was produced

by reactive sintering of boron and zinc oxide at 1450°C and 90-130MPa. The resulting compact was then ground for consolidation by explosive consolidation and hot pressing. Certain compacts were then selected to be infiltrated by aluminium. The explosive consolidation occurred with a die velocity of 3500m/s, while hot pressing was done under 40MPa and 1400°C for 2 to 4 hours. The resulting compacts had varying properties: hardness varied between 34 and 38GPa, fracture toughness varied between 4.95 and 7.05MPa.$m^{0.5}$ and open porosity of 5 to 15%. After infiltration with aluminium, the porosity varied between 2.30 and 3.85% for explosive consolidation and 3.10 and 4.25% for hot pressing; hardness varied between 28 and 40GPa for explosive consolidation and 25 and 40GPa for hot pressing; while fracture toughness varied between 5.28 and 8.47MPa.$m^{0.5}$ for explosive consolidation and 4.96 and 8.17MPa.$m^{0.5}$ for hot pressing.

However, the composites that Kayhan and Inal produced were of very low density and accompanying high porosity. The density of the produced B_6O material ranged from 2.12g/cm^3 to 2.46g/cm^3 as compared to the density of fully dense B_6O being 2.59g/cm^3. As a consequence of the high porosity, low fracture strength values were recorded. Using a three point bend test method, Kayhan and Inal recorded fracture strength values of up to 75.44MPa. Boron carbide, which is a similar to boron suboxide has a strength of between 310-350MPa (<5% porosity) (Richerson (2006)). Additionally, Kayhan and Inal used the Single Edge Notch Beam (SENB) method, with a notch root of 0.635mm, to determine the

fracture toughness of the materials. This method was found to inevitably yield overestimated fracture toughness values (Quinn (2002)).

Shabalala *et al*. (2007) investigated the properties of boron suboxide powder coated with aluminium. Starting with powder produced from the reaction of boric acid with amorphous boron, the powder was coated with aluminium and then hot pressed between 1700°C and 1900°C under 40MPa of pressure. It is reported that only sintering at 1900°C produced a dense compact (2.51g/cm^3). The hardness of the pure boron suboxide is 30.1GPa and decreases with increasing aluminium additions, to 27.8GPa with 5.6wt% Al. As expected, the fracture toughness of the samples increased with increasing Al additions, to a fracture toughness of 3.37MPa.$m^{0.5}$. Shabalala proposes that the increase in fracture toughness is a result of the aluminium reacting with the B_2O_3 to form $Al_4B_2O_9$.

Shabalala *et al*. (2008) and Kleebe *et al*. (2008) investigated the properties of boron suboxide doped with alumina. The boron suboxide powder was prepared by reacting boric acid with amorphous boron. The boron suboxide powder was mixed with varying (1-7wt%) amounts of alumina powder. The resulting mixture was sintered by hot pressing at 1900°C for 20 minutes under a pressure of 50MPa. Hardness tests were done under 500g and 5kg load. The undoped powder was found to have a hardness of 34.8 ± 1.2GPa. Figure 2-7 shows that increasing alumina addition increases the fracture toughness and decreases hardness of the boron suboxide.

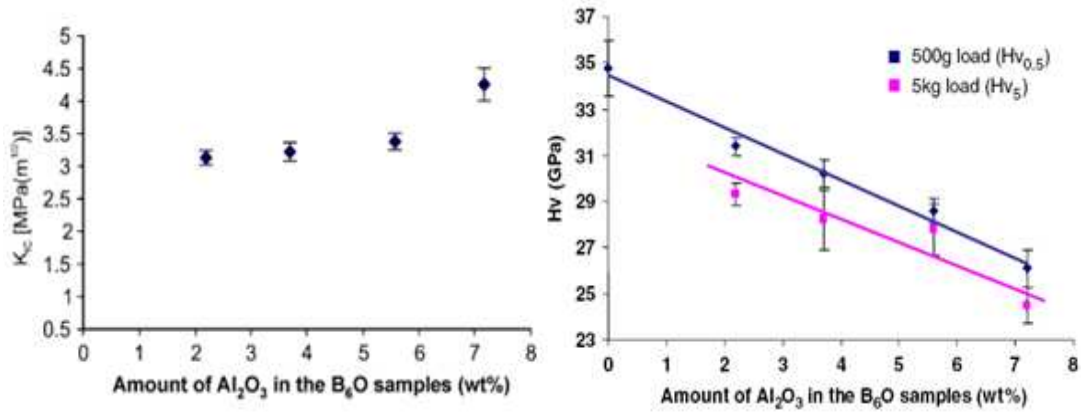


Figure 2-7: The effect of alumina on the fracture toughness and hardness of boron suboxide. Taken from Kleebe *et al*. (2008)

Andrews (2008) produced boron suboxide materials sintered with a range of Y_2O_3-Al_2O_3 additions. The addition of Y_2O_3-Al_2O_3 examined ranged from 1wt% Al_2O_3 and 1.32wt% Y_2O_3 to 4.06wt% Al_2O_3 and 2.24wt% Y_2O_3. It was observed that the densification of boron suboxide materials drastically improved with a small addition of Y_2O_3-Al_2O_3 additive, but larger quantities did not have any significant effect on the density. From TEM images, Andrews concluded that the grain boundaries between the B_6O grains were clean of any secondary phase and that there was extensive twinning within the grains. This was also observed by Shabalala *et al*. (2008) (Figure2-8).

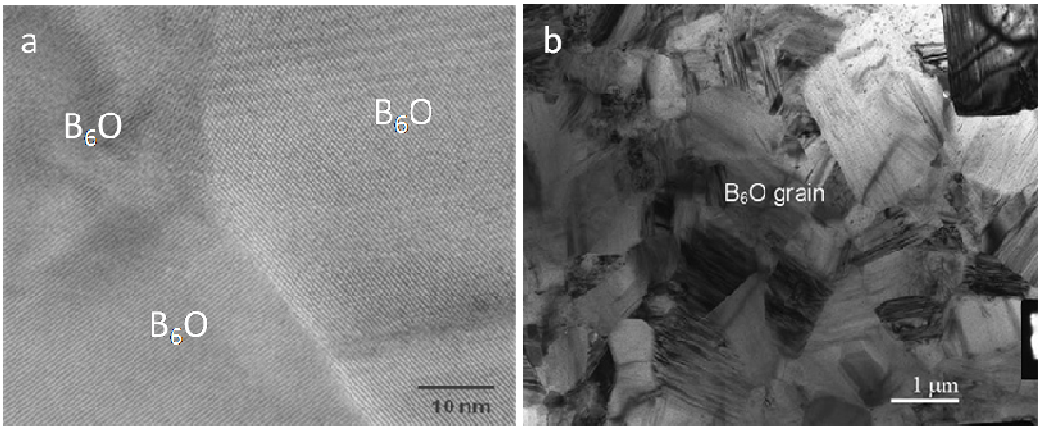


Figure 2-8: Bright field TEM images showing the clean interface between grains (a) (Andrews (2008)) and the multiple twinning within the B_6O grains (b) (Shabalala *et al.* (2008))

Johnson (2008) and subsequently Ogunmuyiwa (2009) sintered boron suboxide materials with a large range of metal, metal oxide and metal boride additives. The composites were hot pressed at 1850°C at 50MPa. The hardness and toughness values for the composites are plotted in Figure 2-9. The elemental composition of the additive phase is indicated on the graph for simplicity. Figure 2-9 shows that there is a wide range of additive materials which can be used to improve the fracture toughness of boron suboxide.

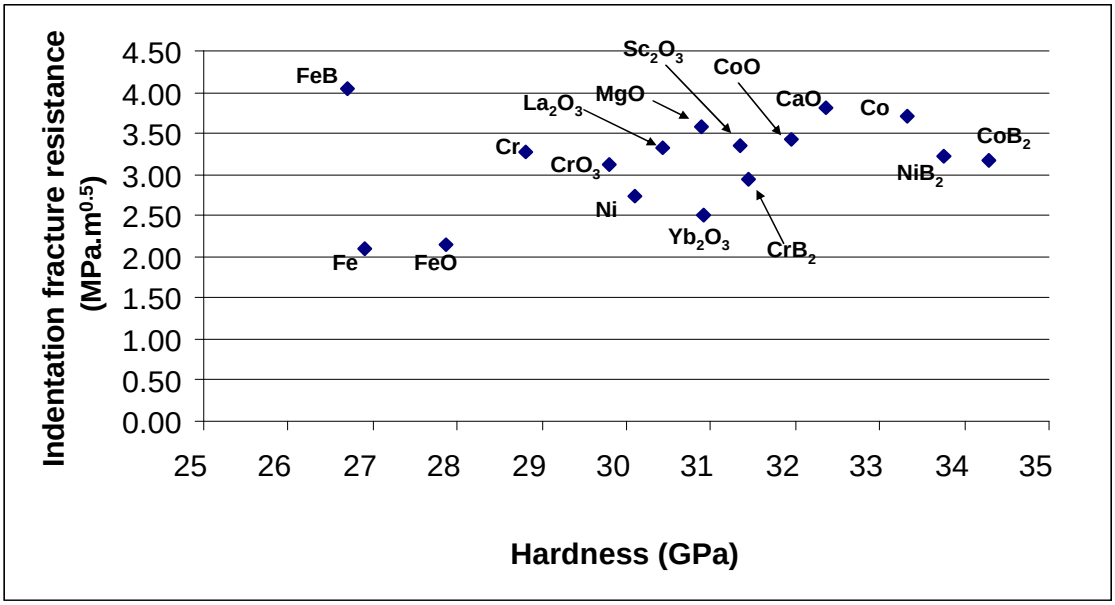


Figure 2-9: Hardness and fracture toughness values for various B_6O composites (Johnson (2008) and Ogunmuyiwa (2009))

Recently, B_6O-TiB_2 composites were produced by the in situ reaction of amorphous boron with titanium dioxide (Equation 2-4) (Herrmann *et al*. (2009)). Compared to previous composites, faster densification was observed for the B + TiO_2 reaction between 1000 and 1600°C, but complete densification required temperatures above 1650°C. It was also noted, that when polishing the composites, the glassy B_2O_3 phase present in final composites was subject to far larger removal rates than the harder matrix (Figure 2-10). This was alleviated to some extent by the addition of Y_2O_3 based additives, which formed a more stable yttria-borate glasses.

$$TiO_2 + 14B \rightarrow 2B_6O + TiB_2$$ **Equation 2-4**

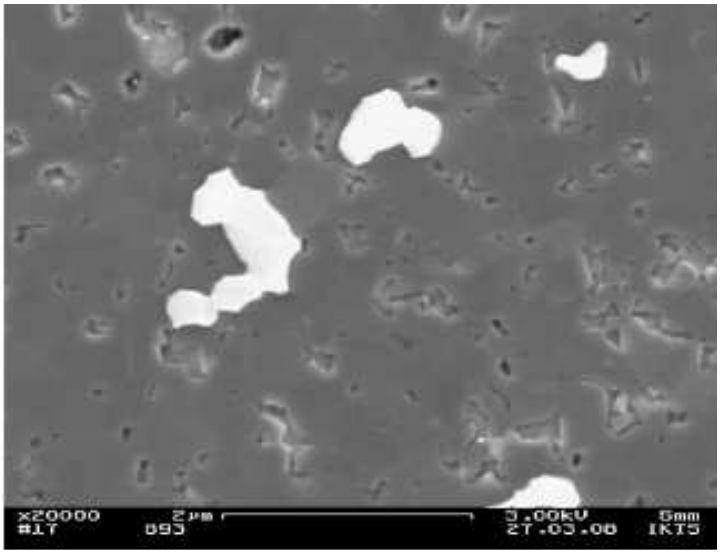


Figure 2-10: A B_6O-TiB_2 (without yttria additions) composite showing the TiB_2 grains (light phase) and partial removal of oxide grain boundary phase (Herrmann *et al*. (2009))

2.5 Thermodynamics of boron suboxide

2.5.1 Enthalpy and heat capacity

In 1986, Makarov and Ugai determined the standard enthaply of formation of boron suboxide. Using dissolution calorimetry of B_6O in nitric acid, the standard enthalpy of formation, at 298K, was determined to be 527±32kJ/mol. Marakov then compared the enthalpy with other boron icosahedral materials of the B_6X form. Figure 2-11 shows that there is a linear dependence of standard enthalpy of formation and the atomic radius (τ) of the inserted atom (i.e. the X species).

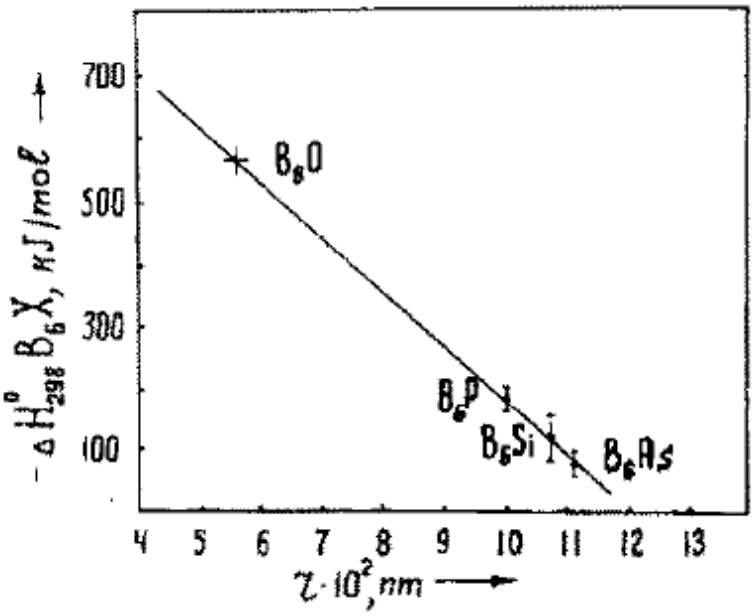


Figure 2-11: Standard enthalpy of formation as a function of atomic radius of X species in B_6X (Makarov and Ugai (1986))

Using the mixing method in a massive calorimeter, Tsagareishvili *et al.* (1990) determined the enthalpy and heat capacity of boron suboxide in the temperature range of 298.15K to 781.5K. Extending the work of Tsagareishvili *et al.* and Makarov and Ugai (1986), Andrews (2008) approximated the thermodynamics of boron suboxide at elevated temperatures (up to 2300K). This is shown in Figure 2-12. This was used to calculate the extent of reaction between B_6O and various compounds in order to assess suitability for use of these compounds as secondary phase reinforcement in boron suboxide composites. It was shown that many oxides and pure metals can be used as a secondary phase within the boron suboxide system. Carbides however, will react with B_6O to form boron carbide.

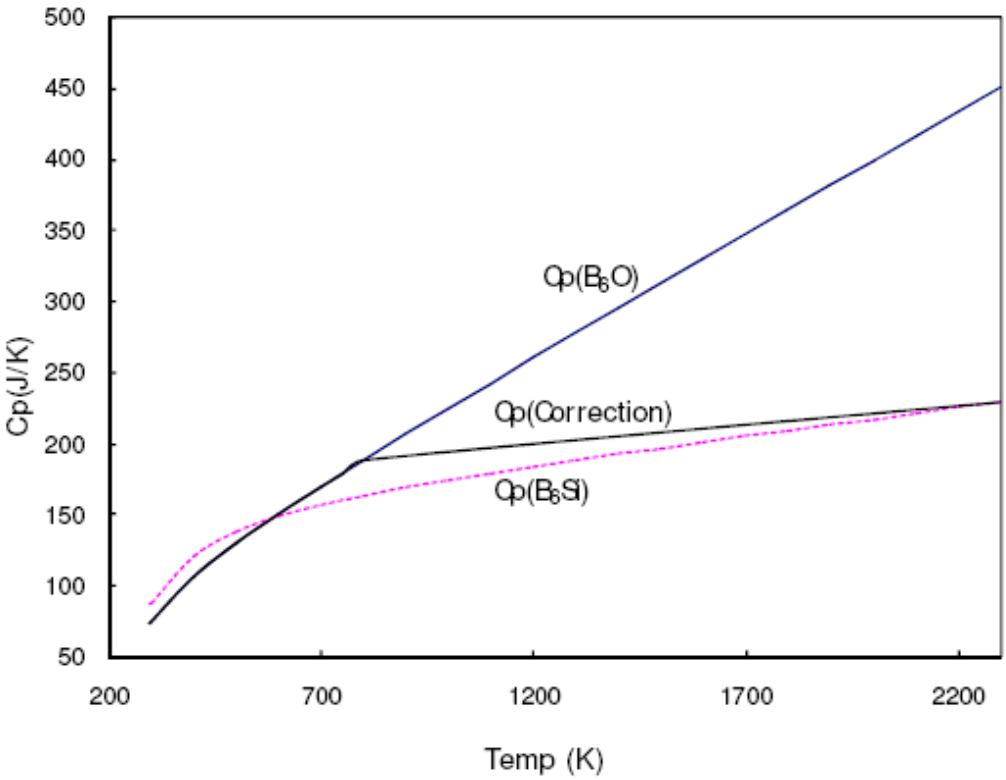


Figure 2-12: The effect of temperature upon heat capacity for B_6Si, B_6O (extrapolated experimental) and for B_6O after correction. (Andrews (2008))

2.5.2 Static interactions with Compacted Graphite Iron

In order for a cutting tool to be successful, it must be able to resist chemical attack by the work piece. Freemantle (2009) undertook an investigation into the reaction between B_6O and Compacted Graphite Iron (CGI) under constant temperature and pressure. The reaction couple consisted of a sintered pure B_6O disc inserted between two CGI discs all held within a hBN pot. At a pressure of 10MPa and a dwell time of one hour, the interaction, under a argon atmosphere, at temperatures of 700, 900, 1100 and 1300°C were investigated.

Freemantle calculated a ternary phase diagram for the Fe-B-O system at 700°C. From the phase diagram (Figure 2-13), the only expected phases are FeB and B_2O_3 from the reaction between Fe and B_6O. However, no boride was detected by XRD analysis after the reaction at this temperature. This could be explained by the phase diagram only accounting for chemical equilibrium and not the kinetics of the reactions.

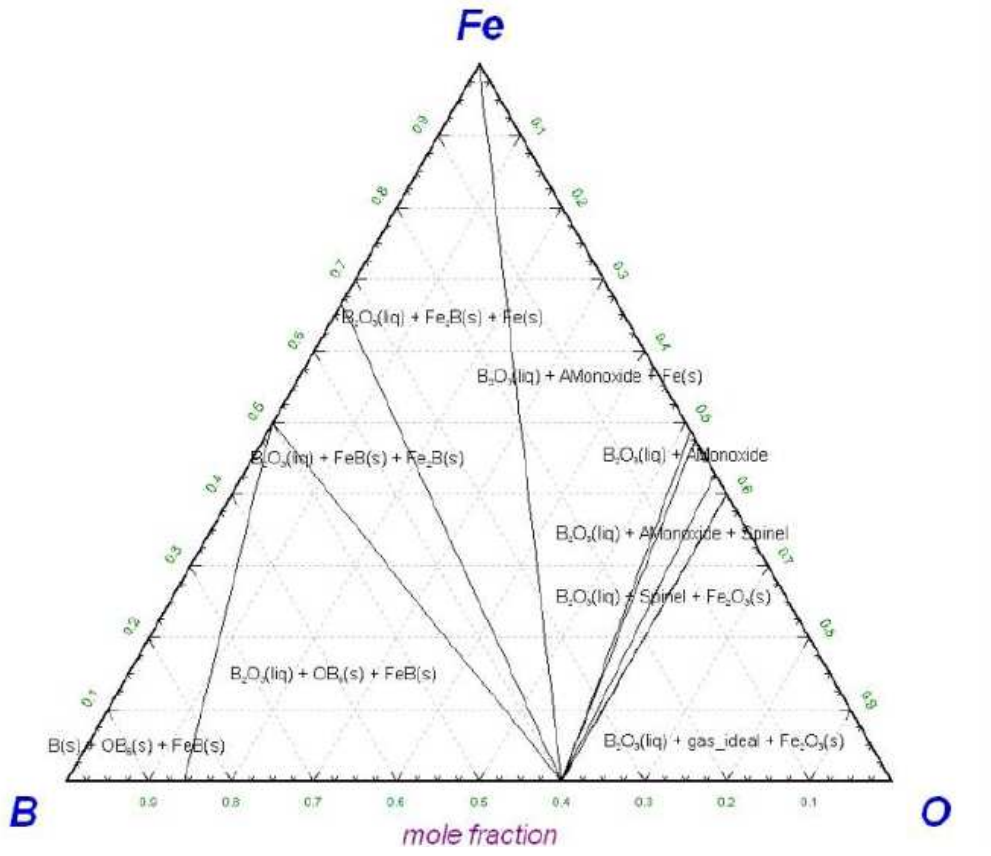


Figure 2-13: The B-O-Fe ternary phase diagram calculated for 700°C (Freemantle (2009))

During the 900, 1100 and 1300°C experiments, reactions between the B_6O and the CGI were observed. Fe_2B formation was observed with increasing temperature. Above 900°C, the Fe_2B formation, together with B_2O_3 formation, raises the possibility of chemical wear of a boron suboxide tool.

2.5.3 Oxidation resistance

Although B_6O is already an oxide, it is possible for it to oxidise further to higher oxides, e.g. B_2O_3. In 2009, Freemantle examined how B_6O was affected when exposed to elevated temperature in moist air. Using a muffle furnace, Freemantle subjected sintered discs of pure B_6O and B_6O-(2wt%Al_2O_3-2.65wt%Y_2O_3) to 1000°C in approximately 14g/m^3 humidity for up to 50 hours. It was observed that a glassy film and small crystals (<50μm), attributed to borohydrates, developed on the surface of the pure B_6O. With the B_6O-Al_2O_3-Y_2O_3 sample, less of a glassy film was observed, however, crystalline rosettes were observed (Figure 2-14). By XRD analysis, the rosettes were determined to be yttria borates. The extent of the glass film and crystal size increased with increasing dwell time.

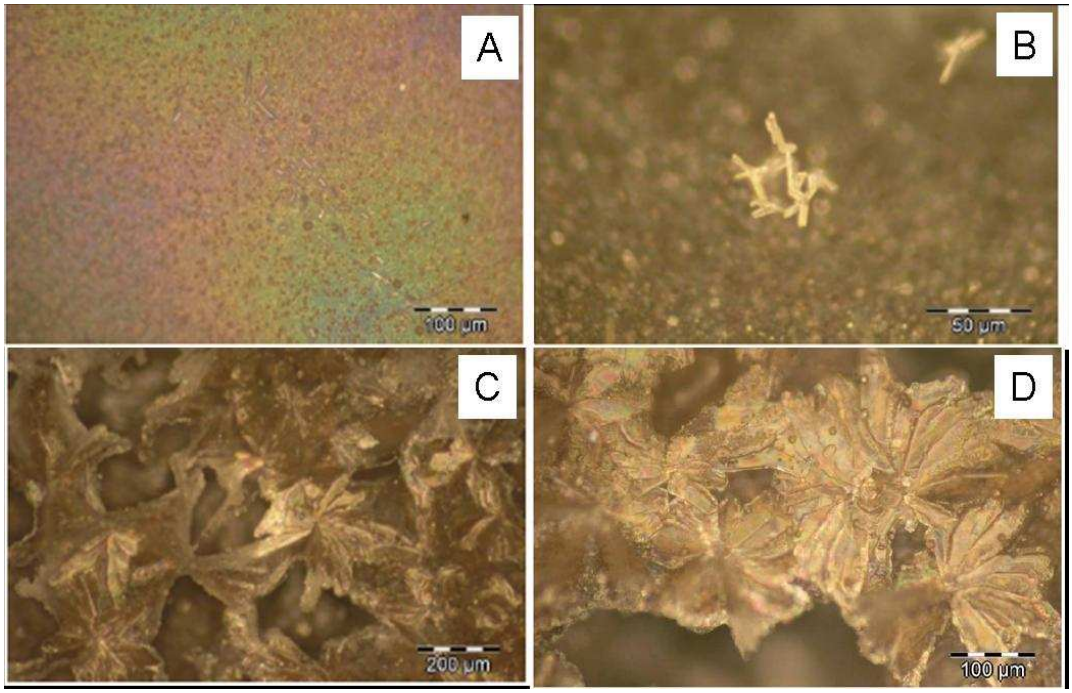


Figure 2-14: Optical micrographs after 10 hours of heat treatment. A and B are from the pure B_6O sample. C and D are from the B_6O-Al_2O_3-Y_2O_3 sample. Freemantle (2009)

Oxidation resistance of $B_{13}O_2$ was examined by Kharlamov *et al*. (2002) in dry air. From Figure 2-15, Kharlamov deduced that the powder of boron suboxide is more stable in air than powdered crystalline boron. At 900°C, the extent of oxidation of $B_{13}O_2$ did not exceed 50%. This was attributed to the formation of a film of molten B_2O_3 on the surface of the boron suboxide. The particle size of the boron suboxide powder was around 2µm, with crystal agglomerates of up to 10µm in size. The size of the boron powder was not specified.

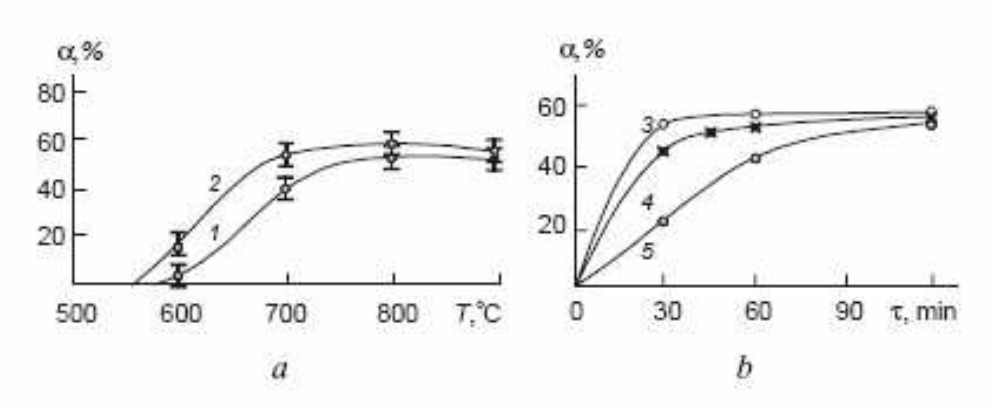


Figure 2-15: Temperature (a) and kinetic (b) curves for the reaction of powdered boron suboxide (1) and boron (2). Kinetic curves for boron suboxide under isothermal conditions at 900 (3), 800 (4) and 700°C (5) (Karlamov (2002))

2.6. Hardness

2.6.1. Hardness testing

Hardness is normally defined as the resistance of a material to plastic deformation (Dieter (1976)). However, for ceramic materials, factors other than plastic deformation affect the hardness of a material. These factors include microcracking and pore compaction (Malzbender (2002)). The experimental method used to determine hardness usually involves using an indenter of known geometry and measuring the depth of penetration of the said indenter.

However, it has been extensively proven that the hardness values determined in an indentation test is dependent upon the applied load. The observed trend is that the

apparent microhardness increases with decreasing load. This phenomenon is called the “indentation size effect” (ISE) (Stevenson *et al*. (2002)).

The effect of load upon hardness typically has two regions. Firstly, at elevated loads, there is a plateau where hardness is either independent or very weakly dependent of the applied load. Secondly, at lower loads, there is a sloped load dependent region. This general trend is illustrated by Figure 2-16. There is no agreement of what load to use during hardness testing, although it would be sensible to use a load which lies in the load independent region. A region which is completely independent of load is not always achieved. At higher loads a region which is weakly load dependent sometimes occurs.

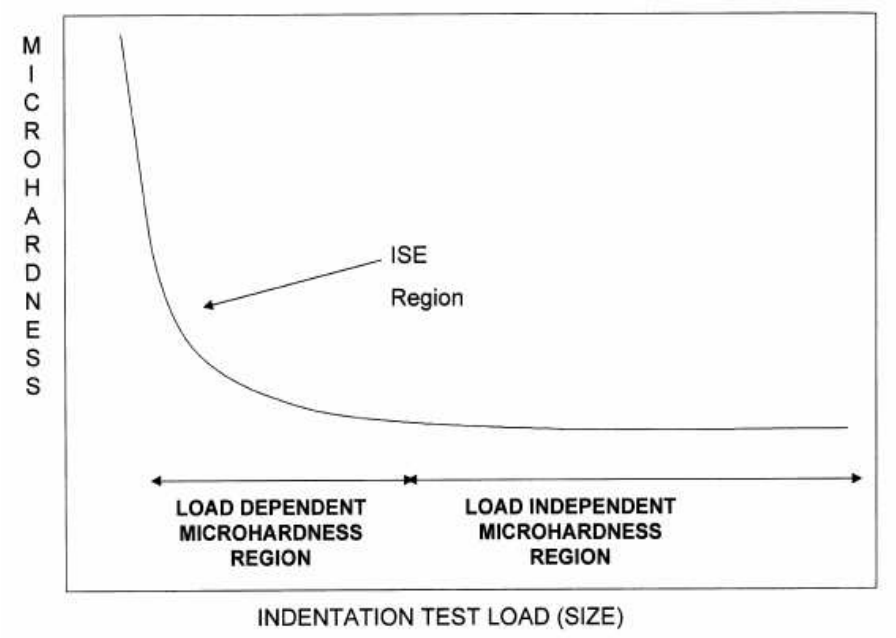


Figure 2-16: Effect of load on microhardness (Stevenson *et al*. (2002))

The ISE can be modelled using Meyer's power law (Equation 2-5)

$$P = KD^n \qquad \textbf{Equation 2-5}$$

Where, P is the load, K is a constant and D is the diameter of the indentation. The Meyer's index, "n", is used as a measure of the ISE. When the hardness is independent of load, "n" equals 2. When hardness increases when load decreases, "n" is less than 2. When hardness decreases when load increases, "n" is greater than 2 (Yurkov *et al*. (1997)).

2.6.2. Hardness of boron suboxide

When testing the hardness of boron suboxide, a range of loads were applied to the indenter. As a result of the indentation size effect, it is not possible to directly compare values reported by different authors. The ISE would also explain the scatter in reported hardness values of pure boron suboxide. Table 2-1 shows the different hardness values reported by the different authors.

Table 2-1: Previously recorded hardness values of boron suboxide

Author	**Sintering pressure** (MPa)	**Sintering temperature** (^{o}C)	**Indention load** (kg)	**Hardness** (GPa)
Ellison-Hayashi *et al*. (1994)	20-28	1900-2100	0.1	38.2*
Kayhan *et al*. (1999)	Explosive		0.1	36.0
	HP		0.1	37.0
Kharlamov *et al*. (2002)	80	1800-2000	0.1	38.0
He *et al*. (2002)	55,000	2100	0.1	45.0$
Shabalala *et al*. (2007)	50	1900	1	30.1±1.2
Kleebe *et al*. (2008)	50	1900	0.5	34.8±1.2
Andrews *et al*. (2008)	50	1900	0.5	35.0±0.8

* Knoop hardness

$ Single crystal

Ellison-Hayashi (US Patent 5330937) plotted Knoop hardness of various hard ceramics against indentation load. As can be seen from Figure 2-17, boron suboxide experiences a sizable ISE. However, insufficient data points were plotted to compare the hardness of the different authors as in Table 2-1.

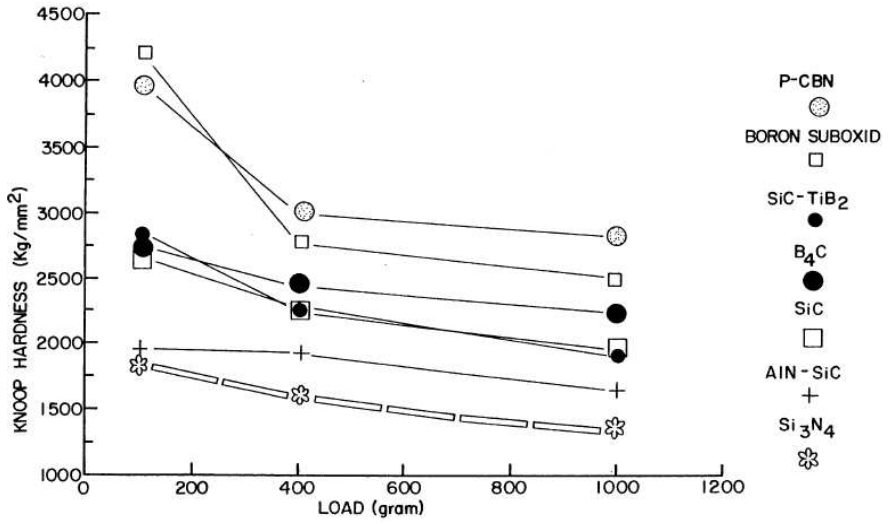


Figure 2-17: Hardness against load for various ceramics (Ellison-Hayashi (US Patent 5330937))

2.7. Fracture Toughness

In industrial applications, the majority of ceramic components fail due to unstable propagation of a pre-existing flaw. Such flaws may be introduced into the component during manufacturing or machining. These flaws may be pores, cracks or inclusions. (Munz (1999)). Due to the presence of these flaws, it is not sufficient to design components against the material's yield strength, as crack propagation can occur at much smaller loads (Roesler (2007)).

Fracture mechanics addresses this problem. Fracture mechanics' main objective is to predict at what load a crack will grow, in order to enable safe design (Roesler (2007)). Fracture mechanics deals with planar cracks with extremely sharp crack tips. However, flaws have a finite volume (Munz (1999)). Despite this, a description of a flaw in terms of a sharp crack is possible using linear-elastic fracture mechanics (LEFM).

There are three different load cases which produce high stress at the crack tip. In mode I (σ_y) (Figure 2-18 I) the largest principle stress is perpendicular to the crack surface. Tensile stresses open the crack, separating the surfaces. Mode II (τ_{xy}) (Figure 2-18 II) is shear loading in the plane of the crack. Mode III (τ_{yz}) (Figure 2-18 III) is shear loading out of the plane of the crack. Mode II and mode III loading does not open the crack, instead the crack surfaces slide against one another, dissipating the applied work. (Roesler (2007)) Mode I failure is the most important (Munz (1999)).

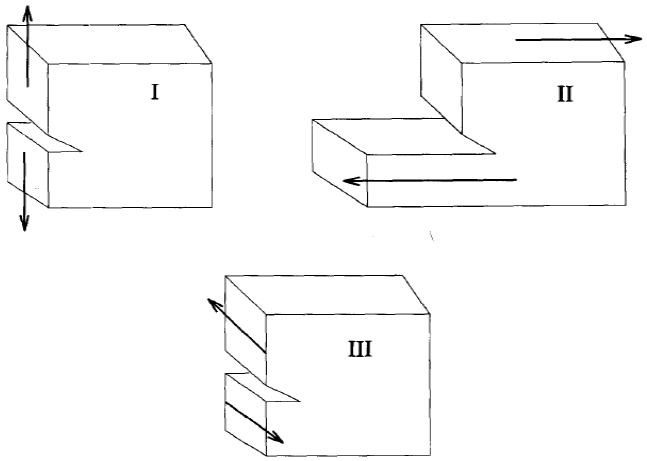


Figure 2-18: Modes of failure: I: Opening, II: Sliding III: Shear (Atkinson (1995))

If a crack is present in a linear elastic, homogeneous and isotropic material, then the stress distribution near a crack tip can be characterised by the polar coordinates r and φ. In the case of mode I cracking, the stress distribution is given as (Munz (1999), Roesler (2007)):

$$\sigma_{11}(r,\varphi) = \frac{K_I}{\sqrt{2\pi r}}\cos\frac{\varphi}{2}\left[1-\sin\frac{\varphi}{2}\sin\frac{3\varphi}{2}\right] \qquad \textbf{Equation 2-6}$$

$$\sigma_{22}(r,\varphi) = \frac{K_I}{\sqrt{2\pi r}}\cos\frac{\varphi}{2}\left[1+\sin\frac{\varphi}{2}\sin\frac{3\varphi}{2}\right] \qquad \textbf{Equation 2-7}$$

$$\tau_{12}(r,\varphi) = \frac{K_I}{\sqrt{2\pi\pi}}\cos\frac{\varphi}{2}\sin\frac{\varphi}{2}\cos\frac{3\varphi}{2} \qquad \textbf{Equation 2-8}$$

where: K_I (units of $MPa.m^{0.5}$) is a stress intensity factor which is dependent upon the applied load, the size of the crack and the geometry of the component. For mode I:

$$K_I = \sigma \sqrt{\pi a}\, Y$$ **Equation 2-9**

In this case, σ is the stress observed by an uncracked component of the same geometry. Y is a geometric factor, normalised to a characteristic dimension of the component. In the case of a semi-elliptical surface crack, the stress intensity factor will vary along the crack front. The $\sqrt{\pi}$ in Equation 2-9 is the geometric factor for a sharp, elliptical crack. Different crack geometries would result in different factors.

As the stress distribution at the crack tip is a function of K_I, the crack propagation behaviour is also dependent upon the stress intensity factor. When a component with a pre-existing flaw is loaded, the stress intensity factor increases as load increases (from Equation 2-9) until the crack propagates. At this point, K_I is termed the critical stress intensity (K_{Ic}).

2.8. Toughening of ceramics

As a whole, advanced ceramics have a large range of desirable properties. Although there are exceptions, in general ceramics possess low thermal conductivity, low electrical conductivity, favourable optical, electrical or magnetic

properties, low density, corrosion resistance, high elastic modulus, high hardness, wear resistance and high strength at elevated temperatures (Munz (1999)).

However, the applications of ceramics selected for their mechanical properties are often limited by the ceramics' brittleness. In metallic systems, the fracture toughness often lies between 15 and 150MPa.$m^{0.5}$, while in pure ceramic systems, the toughness is often less than 5MPa.$m^{0.5}$ (Evans (1988)). The brittleness of ceramics arises from the strong atomic bonds of ceramics. The large bond strength requires large stresses before dislocations can move. Since dislocation movement is responsible for plastic deformation, the lack of, or extremely limited, dislocation movement in ceramics leads to near atomically sharp cracks and extremely large stresses near the crack tip. Ceramics can be toughened, then, by lowering the stress around the crack tip. (Weiderhorn (1984)) The stress at the crack tip can be partially alleviated through a variety of techniques.

Ceramics can be toughened by controlling the toughening mechanisms present in the material. Attempts to control the flaw size distribution involve reducing the number and size of processing flaws, in line with the Griffiths Equation. Controlling the toughening mechanism present in the material involves altering the microstructure to one which would reduce the stress at the crack tip and thus increasing the fracture resistance of the material.

There are three generic types of toughening mechanism, as described in Figure 2-19. These mechanisms are discussed further below.

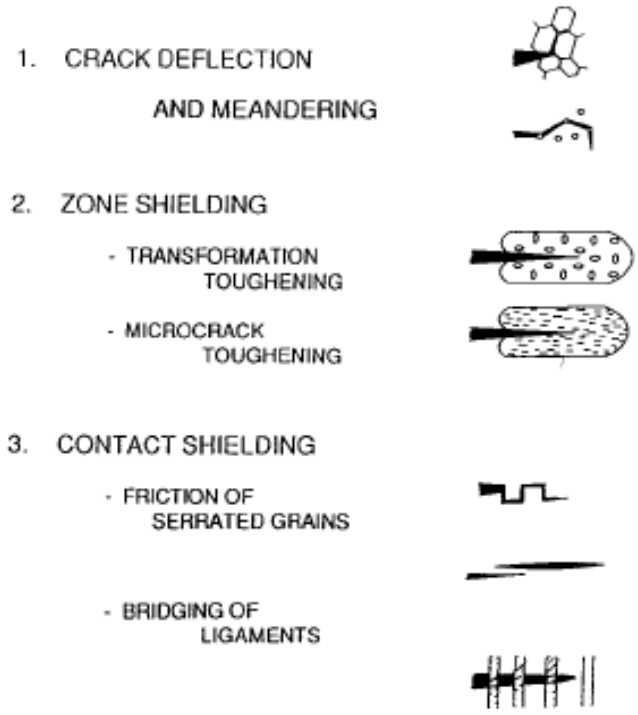


Figure 2-19: The three types of toughening mechanisms (Steinbrech (1992))

2.8.1 Crack deflection

Crack deflection occurs when there are local areas in a ceramic material which have a lower fracture resistance than an average plane perpendicular to the tensile stress (Wiederhorn (1984)). When a crack is deflected from a straight path, the surface area of the crack, per unit of advanced distance increases. This requires additional energy for crack propagation, thus increasing the fracture toughness

(Roesler (2007)). Crack deflection is also a precondition for other toughening mechanisms, such as crack branching and friction of segregated grains.

As grain boundaries typically require only about half the fracture surface energy of a single crystal, it would be expected that a crack advancing through a polycrystalline ceramic would traverse along the grain boundaries (Wachtmann (2009)). The stresses acting in inclined planes near a crack tip depend upon the angle of the incline plane relative to the crack tip. For the same angle, a crack which twists about the direction of crack advance is more effective at increasing the stress intensity factor than a tilt about a direction perpendicular to the crack advance. A crack advancing through a polycrystalline ceramic will encounter grain boundaries at various angles. Based upon deflection of the crack along the grain boundaries, the fracture toughness of polycrystalline ceramics, which experience intergranular fracture, should be approximately twice that of monocrystalline ceramics (Weiderhorn (1984)).

Faber and Evans (1983) examined the effects that particle shape (spheres, rods and discs) has upon crack deflection. The geometry that produced the greatest increase in crack deflection was the rod shape, followed by the disc shape; spherical geometries were the least effective. It was found that an increase in fracture toughness due to crack deflection is dependent upon volume fraction and geometry of the particles, but is independent of the particle size. Although fracture toughness was found to increase with increasing volume fraction of the secondary

phase, a maximum was observed around 20% (by volume), after which, fracture toughness decreased.

In the presence of a secondary phase, cracks also experience modulus interaction. If the secondary phase has a larger Young's Modulus than the matrix, the matrix is partially unloaded in the vicinity around the secondary phases and the stress to propagate the crack is reduced. Hence, the crack will be deflected away from the second phase. Conversely, if the secondary phase has a lower Young's modulus, the local stress is increased, attracting the crack to the particle. If the crack is not able to propagate through the secondary phase, then it must proceed along the interface, further increasing the crack path (Roesler (2007)).

2.8.3 Zone shielding

Zone shielding occurs when there is increased screening of the crack tip from the applied stress as the crack grows. There are two types of zone shielding, transformation toughening and microcracking (Weiderhorn (1984)).

2.8.3.1 Transformation toughening

The most common example of transformation toughening is found in stabilised zirconia composites. As the crack tip advances through the material, it induces a phase transformation of the stabilised tetragonal zirconia into its monoclinic form. This produces an increase in the volume of the zirconia, which produces a compressive stresses around the crack tip. These stresses serve to limit the extent of crack propagation. Since boron suboxide and its additives do not undergo phase transformation, transformation toughening is not possible in boron suboxide ceramics (Evans (1990)).

2.8.3.2 Microcracking

Toughening through microcracking can occur in composites when there are residual stresses resulting from large thermal expansion mismatch between the different phases. Microcracks occur along paths of minimum fracture energy and relieve the local residual stresses. Microcracks also reduce the elastic modulus within the microcrack process zone. Although many ceramics have shown trends consistent with the presence of microcracking, there are relatively few systems which the presence of microcracking has been validated (Evans (1990)). These systems include the SiC – TiB_2 system with expansion coefficients of 5.6 x 10^{-6}/K and 8.5 x 10^{-6}/K respectively (Steinbrech (1992)).

2.8.4 Contact shielding

Segments of a microstructure, located behind a crack front, can impede the opening of a crack by either frictional means, or by the formation of ligaments.

Increase in fracture toughness due to crack bridging occurs in two forms: ductile and brittle. Ductile bridging refers to bridging in metal reinforced ceramics (cermets) and relies upon the ductility and high toughness of the metal reinforcement to produce ligaments in wake of a crack. Upon failure, these ligaments produce acoustic waves, further toughening the material (Evans 1990).

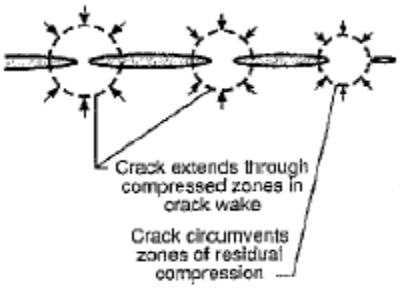


Figure 2-20: Ductile bridging in the wake of a crack (Evans (1990))

In brittle bridging, the bridging material is similar to the matrix material. To produce ligaments, then, the material must possess either weak interfaces or residual stresses or both. If the material possesses weak interfaces, an advancing crack may deflect along the interface, forming intact ligaments in the crack wake.

When these ligaments fail through further debonding or fracture, the fragments will frictionally slide along the debonded surface. As with ductile bridges, brittle bridges also dissipate energy through acoustic wave formation upon failure (Evans, (1990)).

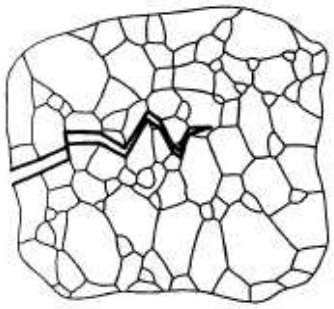


Figure 2-21: Ligaments toughening a brittle ceramic by frictional action (Roesler (2007))

3.0 Experimental Procedure

3.1 Introduction

This section discusses the experimental procedure used for the preparation, characterisation and mechanical testing of boron suboxide materials. Also included in this section is a description of the equipment used for the purposes of this study.

3.2 Hot press runs

For the indentation size effect experiments, hot-pressed discs of pure boron suboxide were required. Boron suboxide, supplied by the Fraunhofer IKTS (Institute of Ceramic Technologies and Systems, Dresden), of d_{50} particle size of 0.11µm was sintered using a uniaxial hot-press (HP20 Thermal Technology). The hot press consists of a central punch and die arrangement, surrounded by a hollow, cylindrical graphite element. The uniaxial hot press is rated for a temperature up to 2200°C with a maximum applied load of 100KN. A rotary vacuum pump, capable of reducing the pressure to 10 millitorre, is attached to evacuate the furnace chamber of air and a gas line supplies an inert atmosphere

(typically argon). The load is applied uniaxially through the lower graphite punch. In order to reduce friction between the moving graphite parts, hexagonal boron nitride was scratched onto the surfaces of the upper and lower graphite punches.

3.2.1 Capsule assembly

A partially bored out cylindrical hexagonal boron nitride capsule of outer diameter 21.4mm and inner diameter of 17.3mm was used to contain the boron suboxide powder for densification. A graphite piston was used to transmit the applied force from the punch directly onto the powder. An hBN disc was placed on top of the boron suboxide powder to prevent contamination of the sample from the graphite piston. hBN was used for the capsule due to its high chemical inertness and thermal stability. This assembly is shown in Figure 3-1.

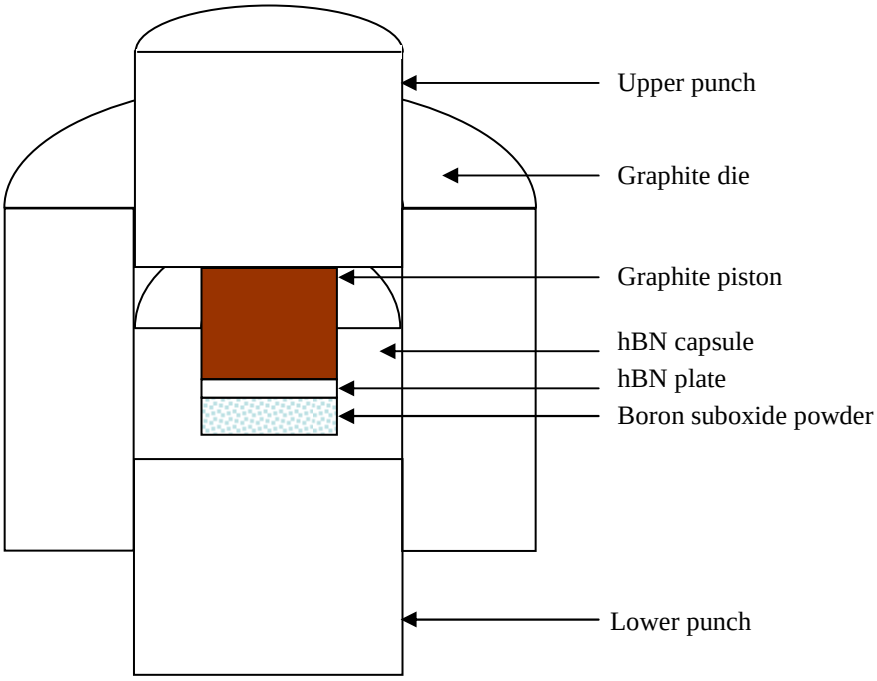


Figure 3-1: Capsule assembly and punch and die configuration

3.2.2 Densifying boron suboxide powder

In order to densify the boron suboxide powder, the uniaxial hot press was heated up at 15°C/min to 1700°C, where 50MPa of pressure was applied to the capsule assembly. The furnace was then further heated to 1900°C at a rate of 10°C/min and left to dwell for 20 minutes. Throughout the second heating step and the dwell period, the pressure was kept constant at 50MPa. The furnace is then allowed to cool at 20°C/min to the ambient temperature.

3.3 Materials to be tested

The boron suboxide based materials which were used for fracture toughness measurements and fractography were supplied as 6mm thick discs and are described in Table 3-1. The composition of the additives stated in Table 3-1 is that of the starting materials..

Table 3-2: Samples, supplied by the IKTS, Dresden, examined for fracture toughness experiments

Composition (vol%)	Disc diameter
B_6O	40mm
B_6O + 1.16% NiO	60mm
B_6O + 1.13% CaO	60mm
B_6O + 1.54% Y_2O_3 + 1.45% Al_2O_3	60mm
B_6O + 1.57% Y_2O_3 + 1.49% Al_2O_3 + 18.69%TiB_2	60mm

3.4 Production of boron suboxide discs by SPS/FAST technology

The Fraunhofer IKTS, Dresden produced the boron suboxide discs which were cut into bend bars for fracture toughness testing. To produce the discs, the IKTS used SPS/FAST technology (Spark Plasma Sintering/ Field Assisted Sintering Technology).

In SPS/FAST technology, a large, alternating DC current is passed through the most conducting route through the graphite punches, the capsule and the ceramic powder. This causes the heat to be generated within the punch and die assembly, rather than in a separate element, as occurs in conventional hot pressing. This means that SPS/FAST is capable of very high heating rates (greater than 300°C/min). The high heating and subsequent cooling rates, in turn, can be utilised to limit grain growth in the ceramic powder. The general configuration of a SPS/FAST system is shown in Figure 3-2.

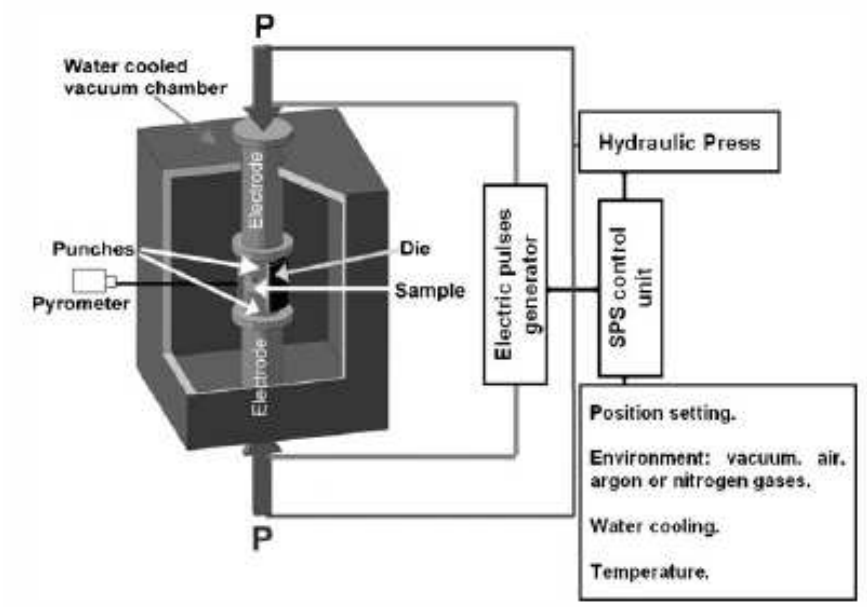


Figure 3-2: Schematic drawing of an SPS configuration (Hungria *et al*. (2009))

Using SPS/FAST technology, the IKTS group produced the ceramic plates which were used in this project for determination of fracture toughness by SEVNB testing. The materials to be examined were pure boron suboxide (as a baseline) and four boron suboxide materials with additives. In terms of the additive phase, the materials were: Y_2O_3-Al_2O_3, CaO, NiO and TiB_2 (with yttria – alumina binder). The exact composition of these materials was described earlier in Table 3-1. The boron suboxide powder for all of the discs (barring the TiB_2 composite) was produced by the borothermic reduction of boron oxide (B_2O_3). The TiB_2 composite disc was produced by the in situ borothermic reduction of TiO_2.

Two pure boron suboxide discs, with a diameter of 38mm and thickness 6mm, were sintered for 5 minutes at 1900°C using a heating rate of 50°C/min. One of

the pure boron suboxide discs was sintered using 50MPa of pressure, the other using 70MPa of pressure. These samples are denoted as B_6OP5 and B_6OP7 respectively. The discs of boron suboxide with additive phases, of a diameter of 60mm and a thickness of 6mm, were produced by sintering for 5 minutes at 1850°C with a heating rate of 50°C/min and 50MPa of pressure applied.

3.5 LASER cutting

For fracture toughness testing, rectangular bars of 40 x 4 x 3mm were required. Due to the extreme hardness of boron suboxide, the discs were cut with a LASER, rather than mechanically with a diamond cut-off blade.

The LASER used for cutting was a LASAG 100W YAG pulse LASER, with a beam width of 0.3mm. The pulse length was set to 0.25ms and a frequency of 20Hz. The LASER advance rate was set to 20mm/min.

The width and length of the bars to be cut out of the sintered discs was increased by 350µm, on each side, to accommodate any heat affected zone effects. Thus, the dimensions of the rectangular cuts of the LASER were 40.7 x 3.7mm for the composite discs and 25.7 x 3.7mm for the pure B_6O discs.

For each of the discs of boron suboxide with additives, ten bend bars were LASER cut. For the pure boron suboxide discs, five bars were cut out each disc. Figure 3-3 shows the layout of the bend bars of the material as they were cut out of the discs. Figure 3-4 shows that of the pure boron suboxide. After LASER cutting, the rectangular bars were then lapped to the required dimensions.

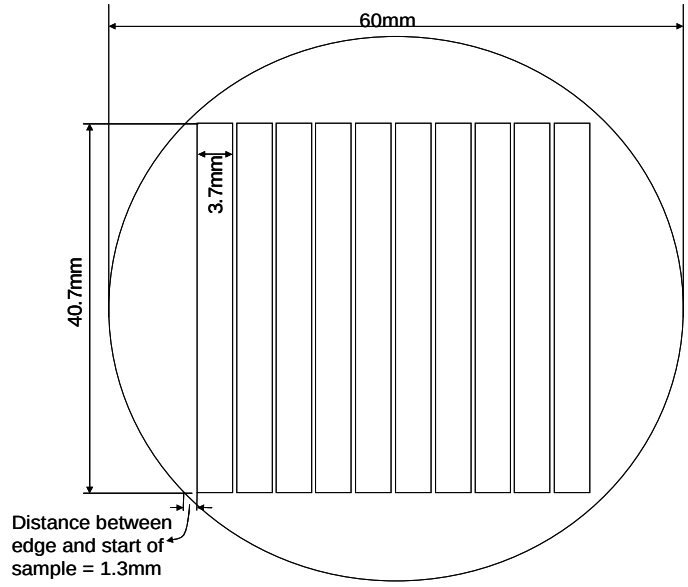


Figure 3-3: Schematic diagram of the layout of the rectangular bars as cut out of the composite discs

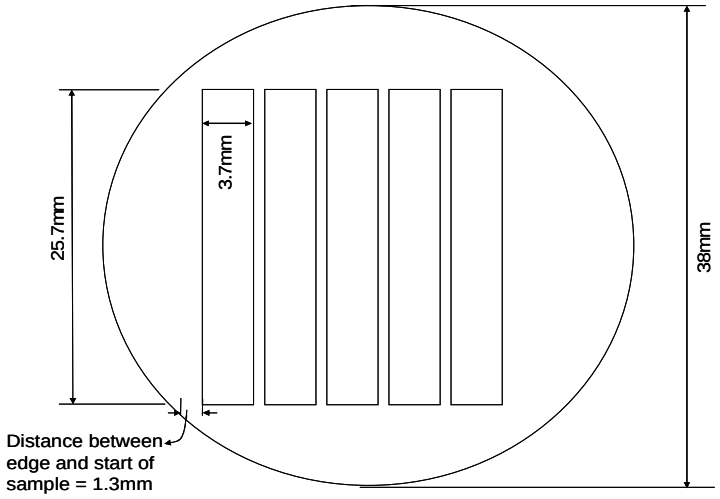


Figure 3-4: Schematic diagram of the layout of the rectangular bars as cut out of the pure B_6O discs

3.6 Lapping and grinding

The as-cut bars had the approximate width and height of 4.7 x 6mm. For the single edge V-notch beam tests, the sample geometry required was 3 x 4mm. To this end, the bars were lapped down to the required size.

The bars were lapped using a Struers DP-U4 polishing machine and a cast iron lapping disc. Since the sample holder on the DP-U4 only accommodates round sample geometry, an attachment was produced to facilitate the rectangular shape of the bend bars.

The attachment consisted of a round, varnished plywood base plate onto which two cylindrical cores of pine were secured. The cylindrical pieces were used to secure the plywood plate to the existing sample holder. A set of ten samples were glued (Contact Adhesive, Pratley) onto two masonite blocks (five samples on each). The blocks were then attached to the base plate using two bolts for each block. Figure 3-5 shows the arrangement of the lapping attachment.



Figure 3-5: Schematic diagram of arrangement used for lapping

The bend bars were lapped using 20µm diamond grit until within 0.5mm of the desired dimensions. The bend bars were then further lapped using 10µm diamond grit to eliminate the any major scratches on the surfaces. The final polishing step was to use a 3µm diamond slurry on a polishing cloth to polish the surface of the bend bars.

3.7 Grinding and polishing

Certain procedures, notably those based upon the Vickers indentation, require a flat, regular surface. To this end, a sequence of steps was taken to ensure a satisfactory surface finish.

A segment of a sample was hot mounted into a Bakelite resin using a 30mm diameter hot mounting press (CitoPress-10, Struers). The mounted sample was then polished on a Leco Spectrum System 2000 automatic polisher. Table 3-2 lists the conditions subsequently used to ensure the mounted sample was polished to a 1µm finish.

Table 3-3: Grinding and polishing conditions

Step	Description	Grit	Speed (rpm)	Load (N)	Time (minutes)
1	Coarse grinding	220	300	35	Until plane
2	Fine grinding	9µm	150	25	5
3	Fine grinding	6µm	150	20	10
4	Polishing	3µm	150	20	8
5	Fine polishing	1µm	150	10	1

Between each of the steps, the mounted samples were cleaned in an ultrasonic bath. If a sample needed to have its surface reconditioned, then the procedure was started from step 3, fine grinding using 6µm diamond grit.

3.8 Density and Porosity

The density (ρ) and open porosity (P_o) of the samples were determined by the Archimedes' principle. For each of the compositions, one of the polished, yet un-notched bend bars were boiled in distilled water for three hours to displace the air from the porosity which was open to the surface. After boiling, the sample was cooled down to room temperature.

The sample was then suspended in water to determine the apparent mass (m_a). The sample was removed from the water and lightly dabbed with tissue paper until all the excess surface water was removed, the wet mass (m_w) was then weighed. The sample was then dried in an oven for 20 minutes and allowed to cool to room temperature, the dry mass (m_d) was then weighed. To increase the accuracy of the density measurements, each of the three weights were determined five times and an average was taken. The density of the sample was determined by Equation 3-1 and the open porosity by Equation 3-2.

$$\rho = \frac{m_d}{m_d - m_a}\rho_{water}$$ **Equation 3-1**

$$P_o = 100\%\left[1 - \left(\frac{m_s - m_d}{m_a - m_w}\right)\right]$$ **Equation 3-2**

The density of the sample was compared to the theoretical density of the samples. The theoretical density was calculated using Equation 3-3, which is based upon the rule of mixtures, ignoring the contribution of porosity.

$$\rho_{Theorectical} = \frac{1}{\sum_{i}^{j}\frac{x_i}{\rho_i}}$$ **Equation 3-3**

where: ρ_i and x_i are the density and mass fraction of component "i" in the composite.

Where possible, the density of the phases present after sintering was used to calculate the theoretical densities. However, in the case of yttria-alumina, it was not certain what the exact composition of the glass was. In this case, the densities of pure yttria and pure alumina were used. The justification for this approximation is presented in Appendix A. The theoretical densities of the components and

composites are presented in Tables 3-3 and 3-4 respectively. For all of the boron suboxide materials, it was assumed that there was 1.5wt% B_2O_3 present in the sintered material. The exact quantity of B_2O_3 present in the samples after sintering is not known. Additionally, the density of boron suboxide is also unknown. Boron suboxide is substoichiometric. The extent of substoichiometry, depends upon the method used to produce the material. As it was not possible to determine the oxygen content within the boron suboxide with a high degree of accuracy, an oxygen content greater than expected was chosen, as to not overestimate the density. The stoichiometry chosen, $B_6O_{0.90}$, has a density of 2.55g/cm^3.

Table 3-3: Density of individual phases present in sintered discs

Material	Density (g/cm^3)
B_6O	2.55
TiB_2	4.50
Y_2O_3	5.03
Al_2O_3	3.99
NiB	7.17
CaO	3.35

Table 3-4: Theoretical densities of each of the samples. Includes 1.5wt% B_2O_3

Composition	Theoretical density (g/cm^3)
B_6O	2.53
B_6O + 1.16% NiO	2.53
B_6O + 1.13% CaO	2.54
B_6O + 1.54% Y_2O_3 + 1.45% Al_2O_3	2.59
B_6O + 1.57% Y_2O_3 + 1.49% Al_2O_3 + 18.69%TiB_2	2.91

3.9 Microscopy

Large portions of this study required microscopy either to generate results, or to lay the foundation for the analysis of the results. The size of the feature being examined determined which microscope was used.

A reflected light optical microscope, a Carl Zeiss AxioCam MRc AV31-KS microscope was used for any body of work requiring magnification up to 1000x. The images from the camera were captured onto the image processing software

Axiovision v3.1. The light microscope was extensively used for determining notch depth and root radius.

For magnifications higher than 1000x, a Philips XL 30 ESEM-FEG series scanning electron microscope, equipped with energy dispersive x-ray spectroscopy (EDS) was used. The ESEM was equipped with a field emission gun capable of operating in the range of 5 to 30kV.

3.10 XRD analysis

For phase analysis, a Bruker AXS D2 phaser X-ray diffractometer equipped with a Cu Kα radiation source was used. During the scan, the voltage was set at 30kV and 10mA. Phase identification was performed using the program Philips Analytical X'Pert HighScore® using the International Centre for Diffraction Data (ICSD) database.

3.11 Hardness Testing

Hardness is defined as a materials resistance to indentation. (Roesler *et al*. (2007)) For hardness testing in metallic systems, a wide range of indenters can be used. These indenters come in two general types, blunt indenters such as the Brinell

indenter and sharp indenters, such as the Vickers indenter For ceramic materials, it is important that a sharp indenter is used to prevent uncontrolled cracking around the indentation. For this reason, a Vickers indenter was used to determine the hardness of the boron suboxide based materials.

Two Vickers hardness testers were used for the purposes of this project. A Leco V-100-A2 capable of loads greater than 1kg and a Leco M-400A capable of between 10g and 2kg were used. The diagonals of the indentation were usually measured under 200x magnification on a Carl Zeiss Axiotech microscope. Total contact area was used to calculate the hardness of the samples. Equation 3-4 used to calculate the hardness of the samples.

$$H_v = \frac{2\sin\left(\frac{\theta}{2}\right)}{d^2} P \qquad \textbf{Equation 3-4}$$

Where, “P” is the force applied to the indenter, “d” is the average diagonal length and “θ” is the angle between the faces of the indenter. For a standard Vickers indenter, θ is 136°. This simplifies Equation 3-4 to Equation 3-5.

$$H_v = \frac{1.8544}{d^2} P \qquad \textbf{Equation 3-5}$$

A flat and polished surface was necessary to perform hardness tests on a sample. Since the indented samples would often be sent for SEM for further analysis, the polished samples were thoroughly cleaned before indentation. The polished samples were cleaned in an ultra-sonic bath in soapy water for five minutes, then ultra-sound for five minutes in fresh water. Following which, the samples were cleaned in ethanol and dried.

For reported hardness values, all of the boron suboxide composites were tested under a 5kg load. Pure boron suboxide was tested under a 1kg load due to boron suboxide's tendency to crack excessively under higher loads. The indenter dwell time was set to 10 seconds, all hardness tests were repeated a minimum of five times, depending upon the quality of the indentation. An average of these readings was taken.

3.12 Indentation size effect

As described in Section 2.6, the hardness determined by the indentation technique is dependent upon the applied load. In order to determine the effect of load upon the recorded hardness of boron suboxide, a sequence of Vickers indentations were made on the pure hot-pressed boron suboxide samples by changing the applied load. The loads used for the ISE experiments were 0.1, 0.2, 0.3, 0.5, 1 and 2kg.

For all of the tests, a dwell time of 10 seconds was used. In order to ensure reproducibility across samples, three different hot pressed samples were tested. A minimum of five indentations were made for each load for each sample.

3.13 Indentation fracture toughness

As discussed earlier, blunt indenters are seldom used for ceramic testing as there is an increased likelihood of catastrophic cracking around the indenter. Although with sufficiently high loads, cracking also occurs with sharp indenters (such as the Vickers indenter), the cracking is far more directional. With Vickers indenters, the cracking visible after indentation grows radially outwards from the indentation's corners.

Working on WC-Co cermets, Palmqvist (1962) was the first to propose using these radial cracks as a measure of fracture toughness of the material. Although his approach was entirely empirical, it formed the basis of later, more fundamental work. Notably, the work by Anstis *et al*. (1981), Niihara *et al*. (1982) and later Shetty *et al*. (1985) allowed for the calculation of the fracture toughness of glasses and ceramics.

The measurement of K_{Ic} from an indentation by the indentation fracture toughness (IFT) method depends upon the load applied and two measured quantities, the

length of diagonals of the indentation and the length of the cracks. Figure 3-6 shows an indentation with diagonals of “d”, crack length from the indenter of “c” and crack length spanning from crack tip to crack tip of “2a”.

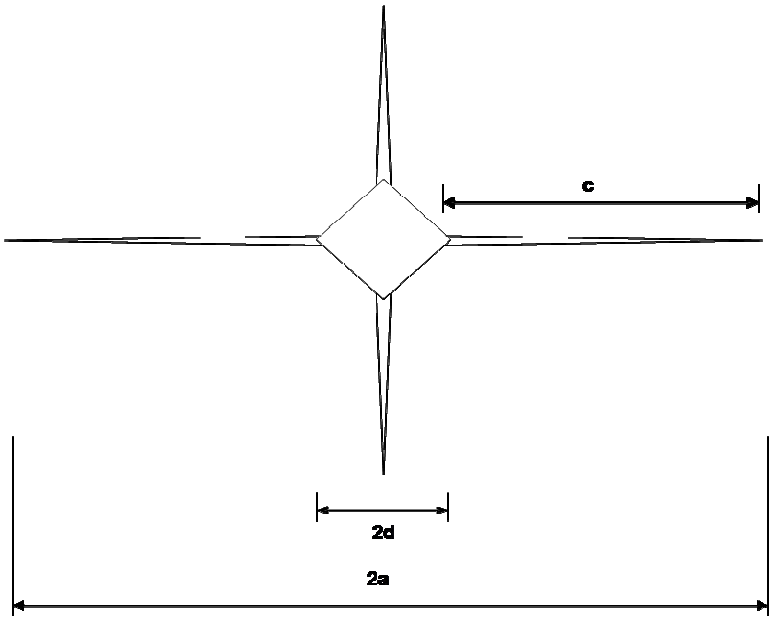


Figure 3-6: An indentation, showing measured dimensions for IFT

Although a large number of Equations have been proposed to determine the fracture toughness from an indentation, generally the Shetty and Anstis Equations are used. Which Equation is used depends upon whether the cracks are fully developed half-penny type cracks or Palmqvist type cracks. The extent of crack development is related to the load applied and the toughness of the material. It is necessary to experimentally determine which cracking regime is present in the material, as to be described in Section 3.13. The Anstis Equation (Anstis *et al.* (1981)) is exclusively applicable to half-penny cracks and is given by Equation 3-

6. The Shetty Equation (Shetty *et al*. (1985)) is only applicable to Palmqvist cracks given by Equation 3-7.

$$K_{ic} = \S\left(\frac{P}{a^{1.5}}\right)\left(\frac{E}{H_v}\right)^{0.5} \qquad \textbf{Equation 3-6}$$

$$K_{Ic} = \frac{1}{3\sqrt{\pi}(1-\upsilon^2)(\sqrt{2}\pi\tan\theta)^{1/3}}\frac{(H_v P)^{0.5}}{(4c)^{0.5}} \qquad \textbf{Equation 3-7}$$

For the Anstis Equation (Equation 3-6), "§" is an experimentally determined constant, usually assumed to be 0.016. For the Shetty Equation (Equation 3-7), θ is the angle between the faces of the indenter (136° for a Vickers indenter) and υ is the Poisson's ratio. The crack lengths, "a" and "c" are as shown in Figure 3-6.

For the Anstis Equation, the elastic moduli of the composites were required. The elastic moduli of the composites were calculated (through Equation 3-8) using the relative volume fractions present in the composite. In Equation 3-8, E_c and E_i are the elastic moduli of the composite and phase "i" respectively and V_i is the volume fraction of phase "i".

$$E_c = \sum V_i E_i \qquad \textbf{Equation 3-8}$$

Due to a lack of available data, the elastic modulus of the yttria-alumina-borate glass was assumed to be approximately 75GPa. Since many glasses have a range of elastic moduli spanning 50-100GPa, 75GPa can be viewed as a reasonable assumption for the elastic modulus for a glass of unknown composition (Shelby (2009)). As mentioned previously, it has been assumed that the final sintered boron suboxide materials have 1.5wt% B_2O_3 within them. The elastic moduli of the boron suboxide based material is presented in Table 3-5.

Table 3-5: Elastic moduli of boron suboxide materials

Material	Phases present	% Phase (vol)	Phase elastic modulus (GPa)	Composite elastic modulus (GPa)
B_6O pure	B_6O	97.9	540[1]	529
	B_2O_3	2.1	17.1[2]	
B_6O - NiO	B_6O	95.2	540	517
	B_2O_3	3.8	17.1	
	NiB	1.0	254[3]	
B_6O - CaO	B_6O	96.8	540	526
	CaB_2O_4 (glass)	3.2	102[4]	
B_6O-Y_2O_3-Al_2O_3	B_6O	96.3	540	523
	Y_2O_3-Al_2O_3-B_2O_3	3.7	75	
B_6O-Y_2O_3-Al_2O_3-TiB_2	B_6O	76.5	540	522
	Y_2O_3-Al_2O_3-B_2O_3	4.8	75	
	TiB_2	18.7	565[5]	

[1] Shabalala (2007)
[2] Inaba, S. et al. (1999)
[3] Smolin, M.D. et al. (1984)
[4] Manupriya et al. (2006)

[5] Munro, G. (2000)

3.14 Distinguishing the crack regime

There are two major cracking regimes in response to a Vickers indentation in brittle materials. They are radial (or Palmqvist) cracks and the radial/median (or half-penny) cracks. The origin of cracks, as a result of the Vickers indentation, is a material response to the indenter loading cycle. The two crack regimes are illustrated in Figure 3-7.

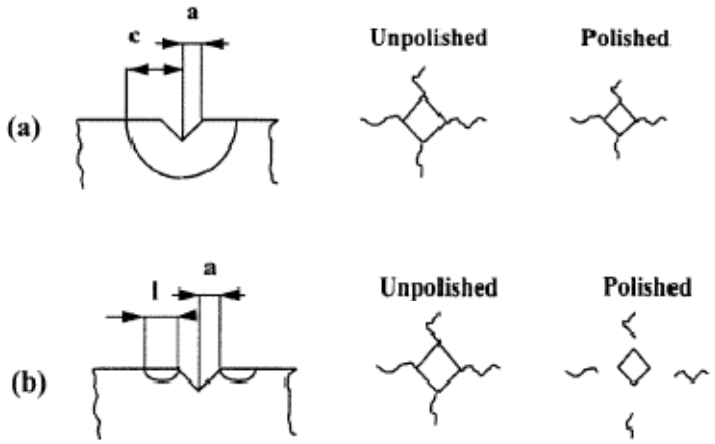


Figure 3-7: (a) Half-penny and (b) Palmqvist cracks as introduced by a Vickers indenter

Below a certain indentation size, the deformation of the material in question is still elastic. For brittle materials, this size is typically very small and is material dependent (Marshall *et al*. (1986)). As a higher load is applied to the indenter, the

local stress around the tip of the indenter becomes higher than the yield point of the material and plastic deformation results. Once the stress reaches a critical level, the main median crack located at the tip of the indentation, opens. At this point, radial cracking also occurs (Oglivy *et al*. (1977) and Lawn *et al*. (1976)). The four radial cracks begin at the edge of the indenter and extend outwards. The radial cracking begins slightly below the surface and extends upwards towards to the surface.

The growth of these cracks is stable as increasing load occurs (Zlatkin *et al*. (1992)). If the applied load is high enough and the material sufficiently brittle, then the two separate radial cracks will extend downwards towards the tip of the indenter, forming one complete hemispherical crack. The growth of the radial cracks into half-penny cracks is both material and load dependent.

For the purposes of calculating fracture toughness from the crack length it is necessary to know which type of crack appears at the edge of the indentation. Unfortunately, there is no way to distinguish between radial and radial/median cracking by examining the as-indented surface (Meacham *et al*. (2006)).

There are, however, a couple of methods which require destructive treatment of the indentation. One, proposed by Jones *et al*. (1987), is to place a drop of lead acetate onto the indenter tip prior to indentation. The lead acetate will infiltrate

into the cracks which form. Upon drying, the sample can be sectioned perpendicular to the indented surface.

The other method relies on radial cracks being shallow. By polishing the indented surface, the radial cracks will become separated from the actual indentation. As hemispherical cracks extend deeper into the surface than the indentation and curve towards the centre of the indent, the polished cracks will not separate from the indent. This is illustrated in Figure 3-7 (Halitim *et al*. (1997), Choudhury *et al* (2006), Meacham *et al* (2006)).

To establish which of the two cracking regimes were active in boron suboxide composites, a section of each of the composites were mounted and polished, as described in Section 3.6. The samples were then indented using a Vickers indenter under a load of 5kg with a dwell time of 10 seconds. Initial micrographs of the indentation were taken at this point. The composites were then coarse polished using 6µm diamond grit for 30 second periods. The pressure and disc speed were the same as discussed in Section 3.6. Micrographs of the indentation were taken at the end of each of the 30 second polishing periods. The final micrograph was taken when the indentation had been completely polished out. The cracking regime was then established by the criteria illustrated in Figure 3-7.

3.15 Crack opening displacement analysis

When examining a Vicker's indentation, it is possible to use, not only the crack length, but also the crack width measurements, to determine the critical stress intensity of a material. Considering the stresses active around an indentation, Fett *et al*. (2005) proposed a method to calculate the critical stress intensity based upon the crack opening displacement (COD).

The method entails measuring the COD as a function of distance within a few microns (~<30µm) of the crack tip. Using measurements of the indentation diameter (d) and the crack length (a), together with the measured distance (x) and an assumed stress intensity factor of one, a calculated value for COD can be found using Equations 3-9 to 3-12.

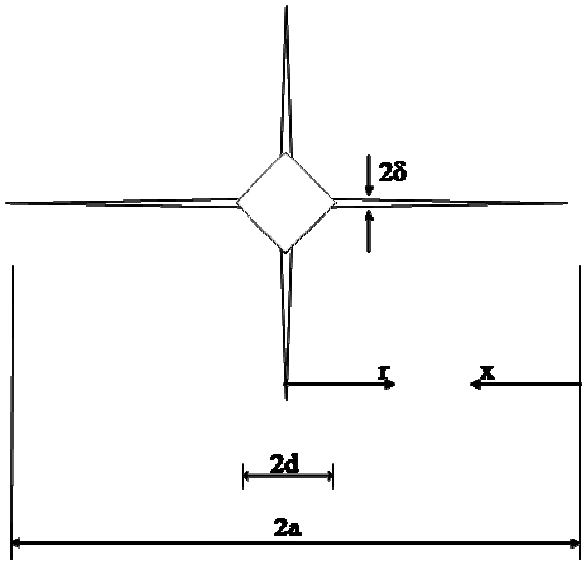


Figure 3-8: Schematic of an indentation showing measured dimensions for COD analysis

$$\frac{\delta}{K}=\frac{\sqrt{b}}{E'}\left(\sqrt{\frac{8}{\pi}\frac{x}{d}}+A_1\left(\frac{x}{d}\right)^{3/2}+A_2\left(\frac{x}{d}\right)^{5/2}\right) \qquad \textbf{Equation 3-9}$$

$$A_1 \cong 11.7\exp[-2.063(a/d-1)^{0.28}]-\frac{0.898}{a/d-1} \qquad \textbf{Equation 3-10}$$

$$A_2 \cong 44.5\exp[-3.712(a/d-1)^{0.28}]-\frac{1}{(a/d-1)^{3/2}} \qquad \textbf{Equation 3-11}$$

$$E'=\begin{cases} E & \text{for plane stress} \\ E/(1-\nu^2) & \text{for plane strain} \end{cases} \qquad \textbf{Equation 3-12}$$

The measured crack opening displacement ($2\delta_{meas}$) is then plotted against the calculated crack opening displacement ($2\delta_{calc,\ K=1}$). The slope of the linear portion

of the graph is the critical stress intensity factor of the material being investigated. The linear portion of the graph is usually found near the crack tip, with deviation from linearity occurring further towards the indentation.

For the purposes of this work, the indentation cracks used to measure K_{ic} by crack length analysis were also used for COD analysis. For the pure boron suboxide samples, where IFT was not possible due to large scale cracking and an improperly formed indentation, a 5kg load was applied to the samples regardless. Although the area around the indentation was badly damaged, the size of the indentation was approximated by an SEM image. This can be observed in Figure 3-9. The average diagonal length was taken as the arithmetic mean of d_1 and d_2.

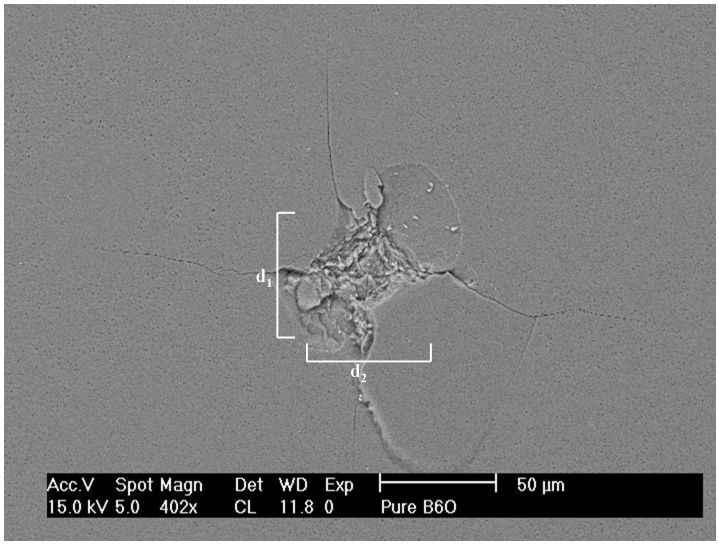


Figure 3-9: An approximation of the diagonal lengths for an indentation in pure boron suboxide

A sequence of SEM images was taken of the indentation cracks. Images of the entire length of the crack were taken at a magnification of 5000x. Images of the region near the crack tip were then retaken at a magnification of 10000x. It was these images which were used for COD analysis of the pure B_6O samples and its composites.

The elastic moduli of the composites were required in order to determine the fracture toughness of the composites by the COD technique. The elastic moduli were approximated using the rule of mixtures of the elastic moduli of the final phases in the composites. The list of elastic moduli approximations is given in Table 3-5 in Section 3.12.

3.16 Single-edge-V-notch beam test

The single-edge-V-notched beam test (SEVNB) is a fracture toughness test based upon the single-edge-notched beam (SENB) test (Kübler (2002)). The SENB test, however, has been found to be heavily influenced by the width of the notch root. During a sequence of Round-Robins, the SEVNB test was found to be user-friendly, reliable, reproducible and comparable with other standard methods for testing fracture toughness, such as the chevron notch and the single-edge-pre-cracked beam tests (Kübler (2002)). For these reasons, the SEVNB test was

chosen as the standard method for determining the mode I fracture toughness (K_{Ic}) of the boron suboxide composites.

Determining the fracture toughness of boron suboxide based materials by SEVNB test involved loading rectangular samples in three point flexure until failure. Testing was performed on a Tinius Olsen H50K-TUTM equipped with a 50kN load cell. The test was controlled and recorded by the program QMAT (v5.43).

The boron suboxide composite test beams had the dimensions of 40 x 4 x 3mm^3. The composite samples were loaded into the mechanical test jig with a span between the outer and inner rollers of 15mm. The pure boron suboxide test beams had the dimensions of 25 x 4 x 3 mm^3, in this case, the distance between the outer and inner rollers was set to 10mm. The diameter of the cylindrical rollers was 5mm. The beam was aligned such that the central roller was directly in line with the notch, but in contact with the un-notched surface. This ensured that the notch experienced maximum loading and that the notch was in opening mode upon loading. The test speed was set to 100µm/s. The layout of the SEVNB test is shown in Figure 3-10. The failure load was recorded and subsequently used in Equations 3-13 to 3-15 to determine the fracture toughness of the material.

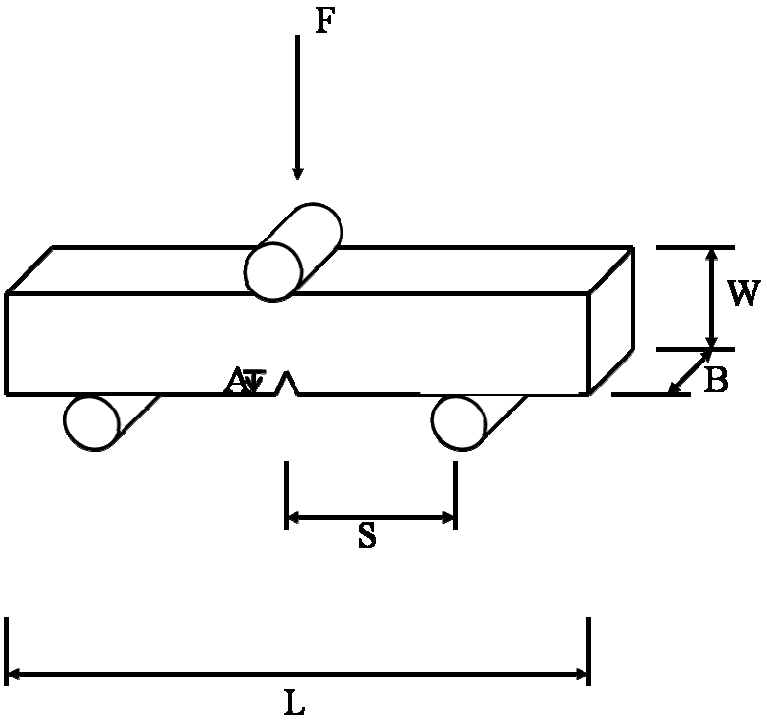


Figure 3-10: Schematic of SEVNB testing layout (Kübler (2002)).

$$K_{Ic} = \frac{F \cdot S}{B \cdot W^{1.5}} \cdot \frac{3\sqrt{\alpha}}{2} Y^{*} \qquad \textbf{Equation 3-13}$$

$$Y^{*} = 1.964 - 2.837\alpha + 13.71\alpha^{2} - 23.25\alpha^{3} + 24.13\alpha^{4} \qquad \textbf{Equation 3-14}$$

$$\alpha = \frac{A}{W} \qquad \textbf{Equation 3-15}$$

As described in Figure 3-10, F is the force applied and S is the span between the middle and outer rollers. The geometric factors a, B and W are the notch depth, breadth and width of the sample respectively.

3.17 Introducing the V-notch

In order to determine the fracture toughness, the SEVNB samples required a notch of a depth between 0.8 and 1.2mm. This notch was introduced in two sequences of steps. Firstly, the beams from each sample were glued onto a 7mm wide steel bar in pairs. When gluing, the 4mm sides of the sample were placed perpendicular to the steel bar, such that the intended tensile surface of the beam was exposed. The samples were then placed in a Secotom-10 Precision Cutting Machine (Struers) and a pre-notch was cut with a 0.8mm diamond cut-off blade. The depth of the pre-notch ranged between 0.2-0.3mm.

After applying the pre-notch, the samples were mounted in V-notcher (Exakt). The V-notcher consisted of a stage which oscillated along a linear path and a head, where a razor blade could be fastened and load could be applied. The samples were mounted in such a fashion that the razor blade rested in the pre-notch. The stage was set to oscillate at 25 cycles per minute, with the distance per cycle being 33mm. The load applied to the razor blade was set at 200g. Concentrated slurries of progressively finer diamond powder were applied

between the notch and the razor blade. The diamond powder used for notching was 9, 3 and 1µm in size. The razor blades were replaced every half hour when the samples were removed from the V-notcher to examine the depth of the notch. After the required depth was reached, the notch was cleaned of diamond powder by ultrasounding the sample in a water bath.

Prior to testing, radii of the notches were examined under a microscope. After testing, the depth of the notch was measured at three places along its length; the average of these measurements was taken to be the depth of the notch. Simultaneously, the notch was evaluated for straightness. If the normalised difference between the maximum and minimum notch depth was greater than 0.1 (Equation 3-17), then the test specimen was rejected.

$$\frac{(A_{max} - A_{min})}{A} \leq 0.1 \qquad \textbf{Equation 3-17}$$

4.0 Results

4.1 Introduction

In this section, the results for the procedures followed in the Chapter 3 are presented.

4.2 Analysis of hot pressed boron suboxide materials

As mentioned in Section 3.8, the density and porosity measurements of the samples were determined by the Archimedes' principle. In the case of the hot pressed boron suboxide pieces, density and porosity both aided in understanding of mechanical properties of the hot pressed material, but also served as a quality control step. The measured densities and open porosities of the hot pressed boron suboxide materials (produced through the method described in Section 3.2) examined in this study are recorded in Table 4-1. As there were multiple hot pressed samples produced, they are labelled HP1 through HP3. The density was then compared to the theoretical density of boron suboxide presented in Section 3.7 (2.53g/cm^3).

Table 4-1: Density and porosity of hot pressed boron suboxide materials

Materials	Density (g/cm^3)	Density relative to theoretical density (%)	Open porosity (%)
B_6O (HP1)	2.44	96.4	1.2
B_6O (HP2)	2.45	96.8	0.9
B_6O (HP3)	2.44	96.4	1.3

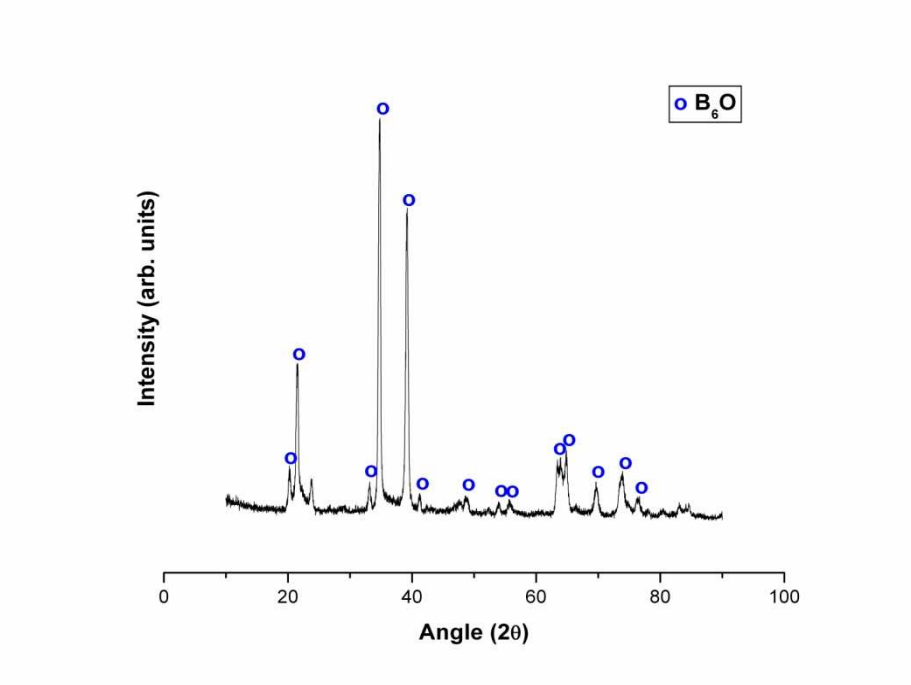


Figure 4-1: XRD trace of B_6O (HP1)

From Figure 4-1, the only crystalline phase that hot-pressed boron suboxide materials contain is boron suboxide. However, there will be trace amounts of MgO as a result of contamination of the starting boron powder. Additionally, there will be some B_2O_3 as a result of partial oxidation of the powder. The exact amount of B_2O_3 remaining in the samples is unknown.

4.2 Analysis of Spark Plasma Sintered samples

4.2.1 Density

The densities of the samples received from the IKTS are recorded in Table 4-2. For the boron suboxide based discs received from the IKTS, density and porosity was established in order to aid understanding of the mechanical properties of the materials. In Table 4-2, the samples B_6OP5 and B_6OP7 refer to pure boron suboxide discs sintered under 50 and 70MPa of pressure respectively. The samples B_6O-NiO (1) and B_6O-NiO (2) refer to two B_6O-NiO samples, both sintered under the same conditions.

Table 4-2: Density and porosity of the samples received from the IKTS

Sample	Density (g/cm^3)	Density as % of theoretical	Open porosity (%)
B_6OP5	2.43	95.6	1.43
B_6OP7	2.42	95.7	1.56
B_6O-CaO	2.48	97.4	0.91
B_6O-NiO (1)	2.47	95.2	0.81
B_6O-NiO (2)	2.49	96.0	0.86
B_6O-Y_2O_3-Al_2O_3 - TiB_2	2.88	98.9	0.22
B_6O-Y_2O_3-Al_2O_3	2.48	95.6	0.50

All of the samples are near fully dense (>95%) and of fairly low open porosity. The addition of secondary phases into the boron suboxide served to lower the open porosity and increases the densification of the materials.

4.2.2 Phase analysis of samples

In order to determine the phases present in the samples densified by SPS, EDS-SEM and XRD analysis were used.

Pure boron suboxide:

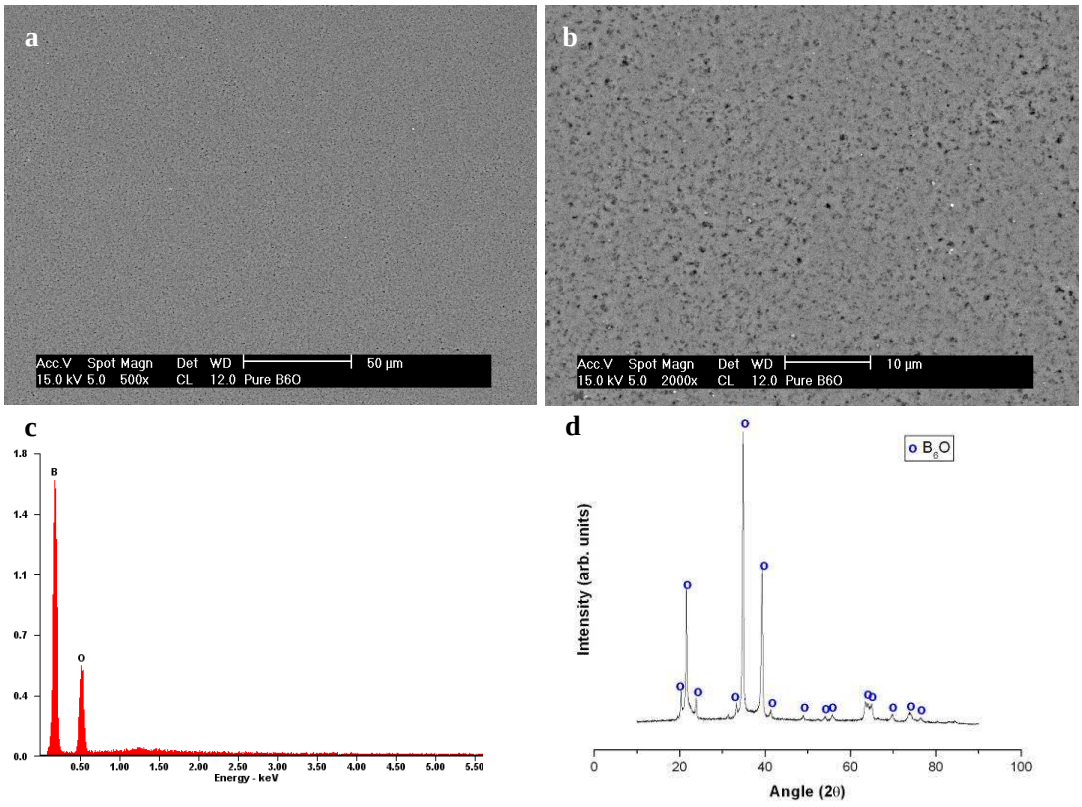


Figure 4-2: Structure (a,b), accompanying EDS spectrum (c) and XRD trace of pure B_6O. EDS spectrum mapped area of image b.

The pure boron suboxide samples registered as pure boron suboxide on the XRD trace. Any B_2O_3 present in the sample would not register on the XRD trace as B_2O_3 seldom ever occurs in a crystalline form. While some of the porosity on the sample seen in Figure 4-2 (b) can be explained by the removal of remnant B_2O_3 during polishing, the majority of the observed porosity would result from removal of material during polishing. This is an effect of the difficulty in polishing boron suboxide materials using the polishing method presented in Section 3.7.

B_6O-Y_2O_3-Al_2O_3-TiB_2:

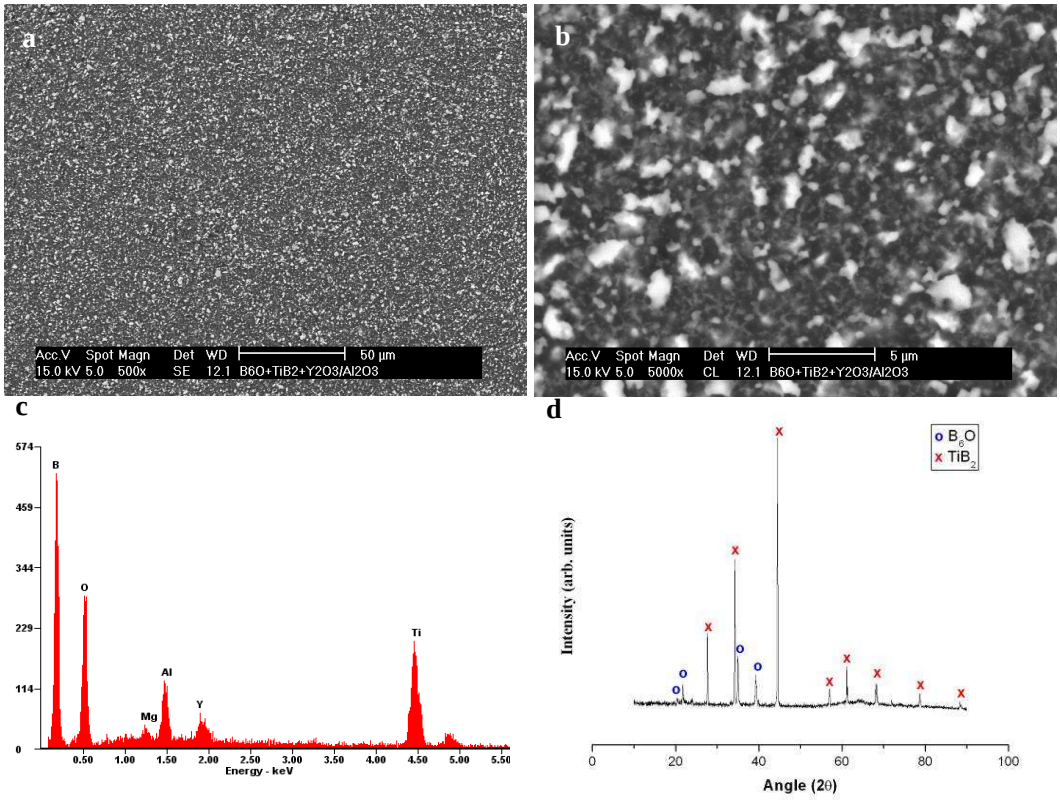


Figure 4-3: Structure (a,b), accompanying EDS spectrum (c) and XRD trace of B_6O-Y_2O_3-Al_2O_3-TiB_2. EDS spectrum mapped area of image b.

For the XRD trace of the B_6O-Y_2O_3-Al_2O_3-TiB_2 sample, it can be seen that the only crystalline phases within the sample are B_6O and TiB_2. However, Y_2O_3 and Al_2O_3 additions were present, as validated by the EDS spectrum (Figure 4-3c). It can thus be reasoned that the Y_2O_3 and Al_2O_3 additions have formed a glassy phase within the composite. However, it must be noted that the XRD trace is only certain for materials are present in quantities greater than 4 volume percent. The yttria and alumina additions will form a glassy phase with any free B_2O_3 present. The exact stoichiometry of the glass is not known. The magnesium detected by the EDS trace is a remnant from the boron powder used at the IKTS for the formation of the B_6O phase.

<u>B_6O-CaO:</u>

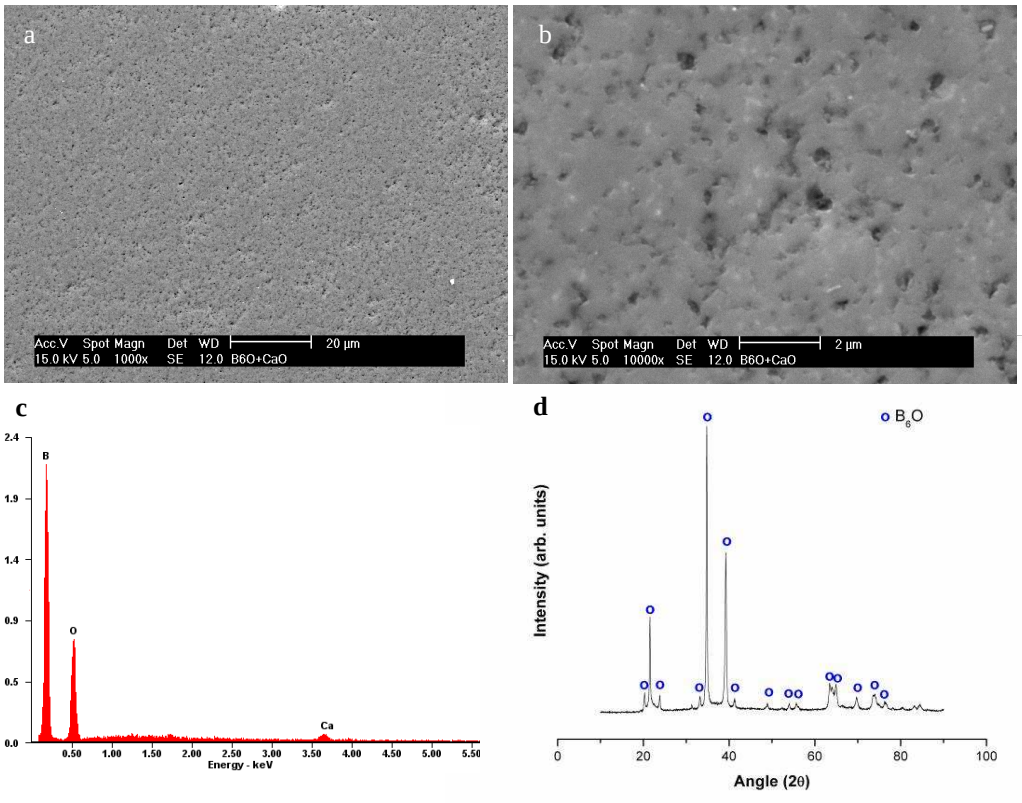


Figure 4-4: Structure (a,b), accompanying EDS spectrum (c) and XRD trace of B_6O-CaO. EDS spectrum area of mapped image b.

For the B_6O-CaO sample, the only phase determined by the XRD trace (Figure 4-4d) was boron suboxide. However, from the EDS spectrum, the sample has some species of Ca remaining within it. As there are no Ca species detected on the XRD trace, the Ca present in the B_6O-CaO sample are present in an amorphous form. The CaO additions most likely formed a $CaO\text{-}B_2O_3$ glass of some, unknown, stoichiometry.

<u>B_6O-NiO:</u>

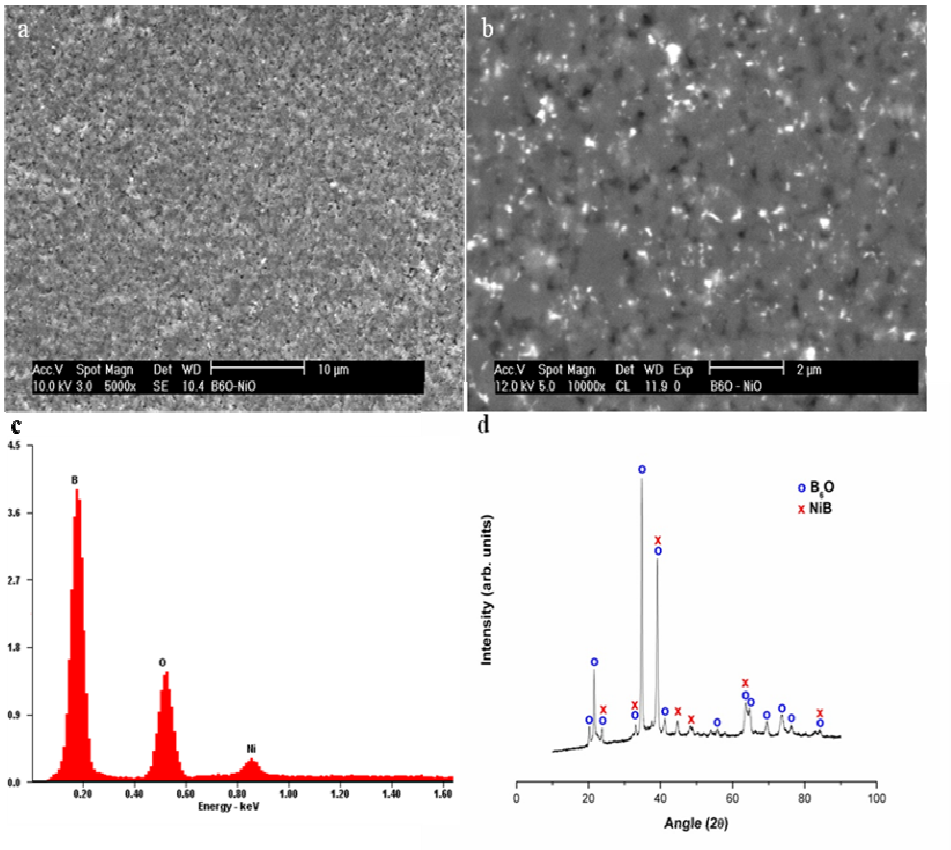


Figure 4-5: Structure (a,b), accompanying EDS spectrum (c) and XRD trace of B_6O-NiO. EDS spectrum area of mapped image b

In the B_6O-NiO sample, the entire starting NiO additive was converted to NiB during sintering. The NiO additive would react with the B_6O matrix through Equation 4-1.

$$\mathbf{5B_6O + 16NiO \rightarrow 16NiB + 7B_2O_3} \qquad \textbf{Equation 4-1}$$

The porosity observable in Figure 4-5b can be attributed to the difficulty in obtaining a well-polished surface for the material.

<u>B_6O-Y_2O_3-Al_2O_3:</u>

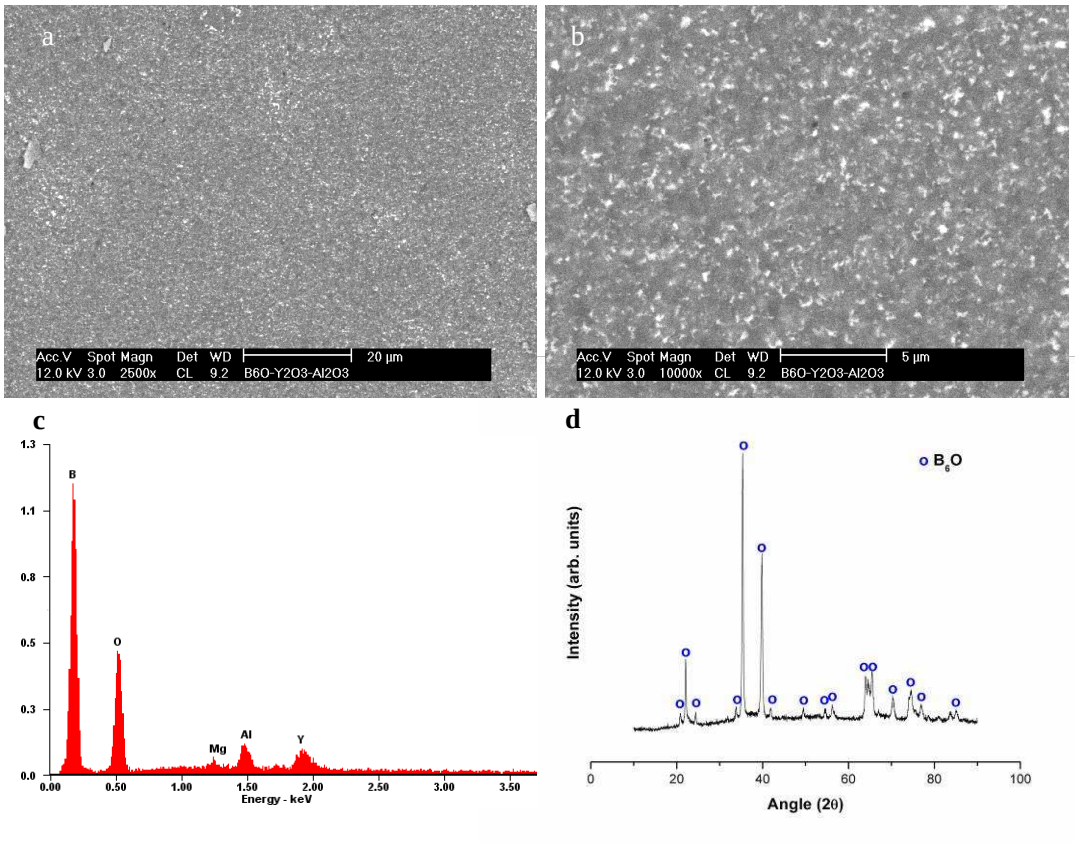


Figure 4-5: Structure (a,b), accompanying EDS spectrum (c) and XRD trace of B_6O-Y_2O_3-Al_2O_3. EDS spectrum area of mapped image b.

In the B_6O-Y_2O_3-Al_2O_3 sample, the only crystalline phase present is boron suboxide. Similar to the B_6O-Y_2O_3-Al_2O_3-TiB_2 sample, Y and Al species are detected on the EDS spectrum, but not on the XRD trace. The Y_2O_3 and Al_2O_3 have formed a glass phase with the B_2O_3 inherently present in the system. The exact composition of the glass is not known. However, the yttria-alumina additive also has a molar ratio of 0.6 for Y_2O_3:Al_2O_3, hence, like the B_6O-Y_2O_3-Al_2O_3-TiB_2 sample, the B_2O_3 content within the glass needs to be between 49 and 65mol% to form a stable glass (based on the work of Chakraborty *et al*. (1986), see Appendix A). The stability of the glass phase may be affected by species like Mg remaining within the system.

4.3 Indentation Size Effect

4.3.1 Hardness Measurements

As outlined in Section 3.12, a series of indentations were made into the hot pressed boron suboxide samples to determine the extent of the indentation size effect. The measured hardness values and their standard deviations are displayed in Table 4-3.

Table 4-3: Hardness measurements for hot-pressed pure boron suboxide

Applied load (kg_f)	Dwell time (s)	Average diagonal (μm)	Hardness (GPa)	Standard deviation (GPa)
0.1	10	6.74	40.4	4.2
0.2	10	10.07	36.1	3.2
0.3	10	12.40	35.5	1.5
0.5	10	16.34	34.0	1.2
1	10	24.26	31.0	3.2
2	10	36.15	27.9	2.5

4.3.2 Meyer's law.

Meyer's law can be used to describe the extent of the indentation size effect in boron suboxide. Meyer's law is given by Equation 4-2; where, "P" is the applied load, "d" is the average indentation diagonal. "A" and "n" are constants which can be established through curve fitting a plot of load against indentation diagonal length (Figure 4-7).

$$P = Ad^n \qquad \textbf{Equation 4-2}$$

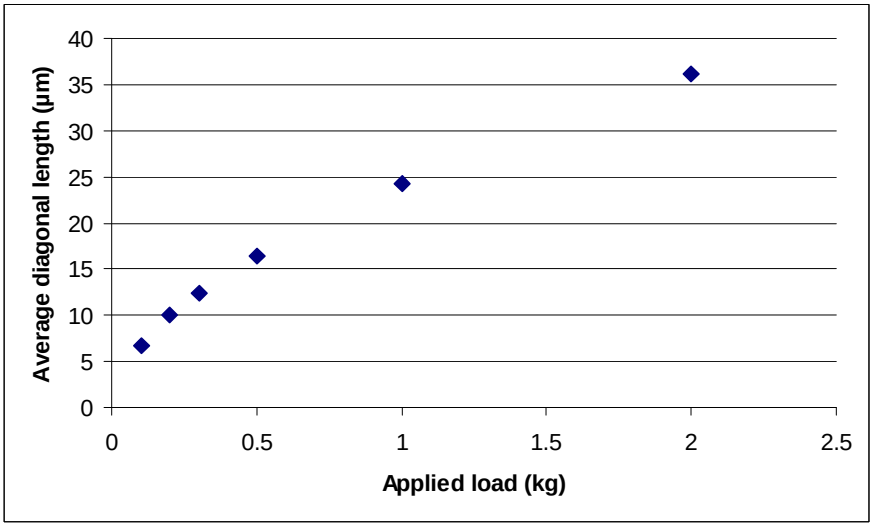


Figure 4-7: Effect of load on the measured diagonal length during hardness testing

By solving for the least sum of squares, the best fit is when "A" has the value of 692 (kg/mm^n) and "n" has the value of 1.76 (with an R^2 value of 0.979). Meyer's law describes the extent to which a material is subject to the indentation size effect by the deviation of the value "n" from the value of 2. An "n" value of 2 means that the material is not subject to any indentation size effect. A deviation of 0.24 implies that boron suboxide has a significant indentation size effect. In turn, this means that it is not possible to directly compare the hardness measurements for boron suboxide when different loads were used in determining hardness measurements.

The Meyer's Law (Yurkov *et al.* (1997)) predicts a region of loading where the measured hardness is nearly independent of the applied load. In order to establish

if there is such a region for boron suboxide, a plot of hardness against applied load was drawn (Figure 4-8).

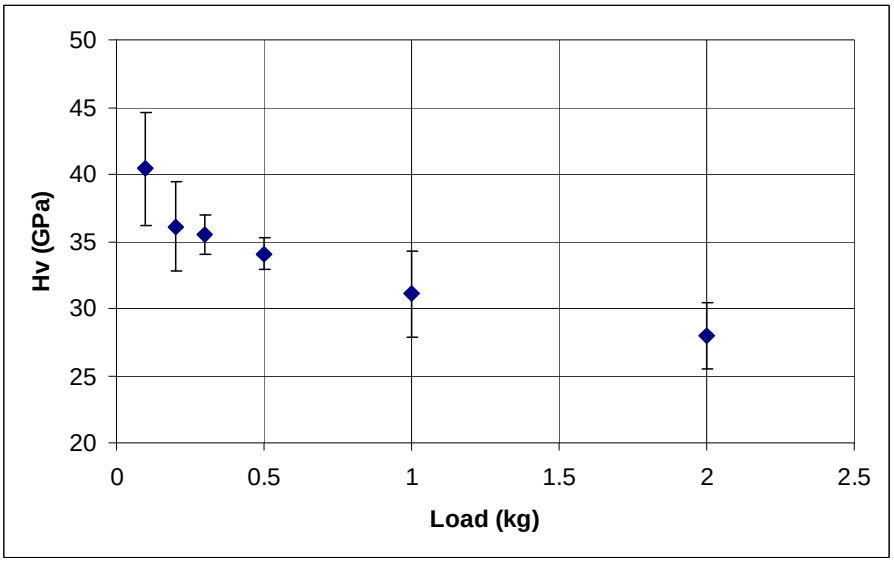


Figure 4-8: Effect of load on the measured Vickers hardness of hot-press, pure B_6O

As can be observed from Figure 4-8 boron suboxide does not have a portion of the graph where hardness becomes near independent of the applied load. While a trend towards linearity may be extrapolated from the graph, thus giving the impression that linearity may be achieved at higher loads, this is not the case. At loads greater than 1kg, cracking around the indentation was observed. At loads greater than 2kg, for instance 5kg, the indentation is damaged to such an extent that no accurate hardness measurements are possible. Since the hardness of boron suboxide is not independent of load at any stage, no standard load for testing the hardness of pure boron suboxide could be recommended.

4.4 Hardness of SPS densified materials

Unlike the pure boron suboxide materials, the boron suboxide composites could be indented with a 5kg load and retain a well defined indentation. This load was used for determining the hardness of the composites as it would produce results directly comparable with previous studies involving composites of boron suboxide (for example, Johnson (2008) and Ogunmuyiwa (2009). Additionally, the 5kg load induced cracks required for indentation fracture toughness measurements. Hardness of the spark plasma sintered pure boron suboxide sample was performed using a load of 1kg. As discussed above, any load higher than this resulted in an extremely deformed indentation. The hardness measurements for the materials densified by SPS are recorded in Table 4-4.

Table 4-4: Vickers hardness (H_{V5kg}) for the spark plasma sintered boron suboxide materials

Material	Hv_5 (GPa)	Standard deviation (GPa)
Pure B_6O	29.2*	2.0
$B_6O – Y_2O_3$-Al_2O_3	20.3	1.2
$B_6O – CaO$	23.2	2.2
$B_6O – NiO$	21.8	2.3
$B_6O – Y_2O_3$ - $Al_2O_3 – TiB_2$	25.7	3.3

*Determined under a 1kg load

4.5 Crack regime

To establish whether indenting boron suboxide composites with a 5kg load would produce Palmqvist cracks, or fully developed half-penny cracks, the method described in Section 3.14 was followed.

Figure 4-9 shows the indentation before and after material is removed by polishing. As can be observed, the cracks are visible even after the indentation is almost entirely removed (Figure 4-9b). This gives evidence that the crack regime that boron suboxide composites experience at a 5kg load are of the half-penny type. This result was used when calculating the indentation fracture toughness of the boron suboxide based materials. A half-penny crack regime means that the Anstis Equation is applicable when calculating the indentation fracture toughness. Hence, when calculating the indentation fracture toughness of the boron suboxide based materials, the Anstis Equation was used instead of, for example, the Shetty Equation.

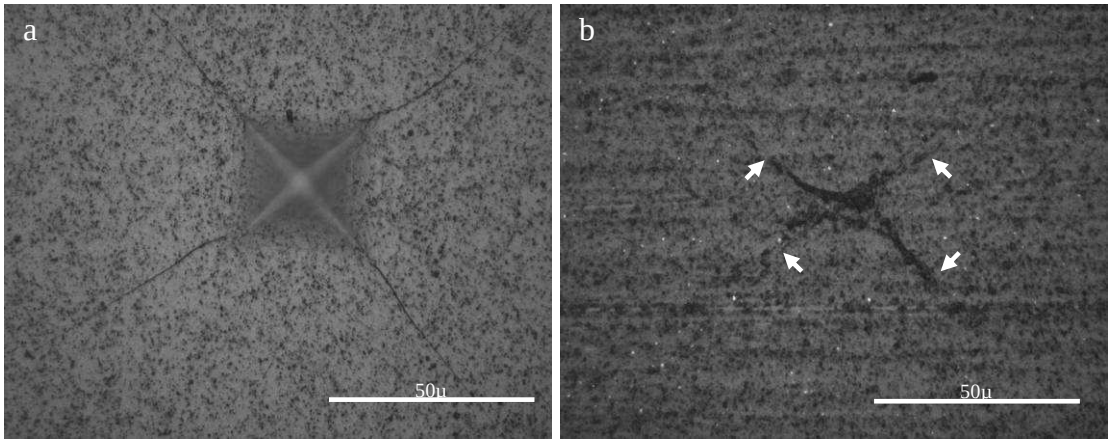


Figure 4-9: An indentation in Y_2O_3-Al_2O_3-B_6O before (a) and after (b) polishing. The white arrows indicate where the cracks are still attached indentation.

4.6 Indentation fracture toughness

While simultaneously determining the hardness of the boron suboxide composites, the indentation fracture toughness (IFT) of the Spark Plasma Sintered boron suboxide composites were measured. As discussed in Section 4.4, the load applied to the indenter for these experiments was a 5kg load, as this was the lowest load where it was possible to resolve the cracks using an optical microscope.

As described in Section 4.3, when using a 5kg load, the indentations in pure boron suboxide samples fail to maintain their shape, and often crack catastrophically (the lateral cracks extend to the surface of the crack, destroying the indent entirely). Although fine cracks emanating from the corner of the indentation are

observed under a load of 1kg, these cracks are too fine to track with an optical microscope. It would be possible to track these cracks using a microscopy technique with higher resolution (for example, an SEM). However, from the work of Shrivastava (2007), it is not possible to accurately compare the measurements obtained from an optical microscope and that which was obtained from an SEM due to differences in the resolution. In the case of an indentation, an SEM image would appear to measure a longer crack length than an image taken using an optical microscope. As this would introduce another variable into the results, IFT was not measured for the pure boron suboxide materials.

The recorded hardness and indentation fracture toughness values, as calculated by the Anstis Equation, are shown in Table 4-5.

Table 4-5: Fracture toughness of boron suboxide materials, determined by the IFT method

Material	$K_{Ic,\ IFT}$ ($MPa.m^{0.5}$)	Standard deviation ($MPa.m^{0.5}$)
$B_6O – Y_2O_3$-Al_2O_3	4.1	0.4
$B_6O – CaO$	4.2	0.4
$B_6O – NiO$	3.9	0.5
$B_6O – Y_2O_3$ - $Al_2O_3 – TiB_2$	3.4	0.2

4.7 Single edge V-notch bend tests

Single edge V-notch beam tests were conducted in accordance to the method described in Section 3.16. The determined values are recorded in Table 4-6. As stated in Section 3.16, the span used for determining the fracture toughness of pure boron suboxide was less than the span used to determine the fracture toughness of the composite materials. This may lead to the pure boron suboxide having a recorded fracture toughness which is slightly higher than expected.

Table 4-6: Fracture toughness of boron suboxide materials, as determined by the SEVNB method

Material	Span (mm)	$K_{Ic,\ SEVNB}$ ($MPa.m^{0.5}$)	Standard deviation ($MPa.m^{0.5}$)
B_6O	16	1.3	0.2
$B_6O – Y_2O_3$-Al_2O_3	30	3.6	0.3
$B_6O – CaO$	30	2.6	0.3
$B_6O – NiO$	30	2.6	0.3
$B_6O – Y_2O_3$ - Al_2O_3 – TiB_2	30	2.9	0.3

4.8 Mode of failure

After testing the samples for toughness by the SEVNB method, the fracture surface was examined under a SEM. Figure 4-10 shows a B_6O-NiO sample after testing. The fracture surface examined is indicated on the Figure. Also evident in the Figure is the cantilever curl, which all bend samples experience. The change in contrast is due to the Figure being assembled from multiple images.

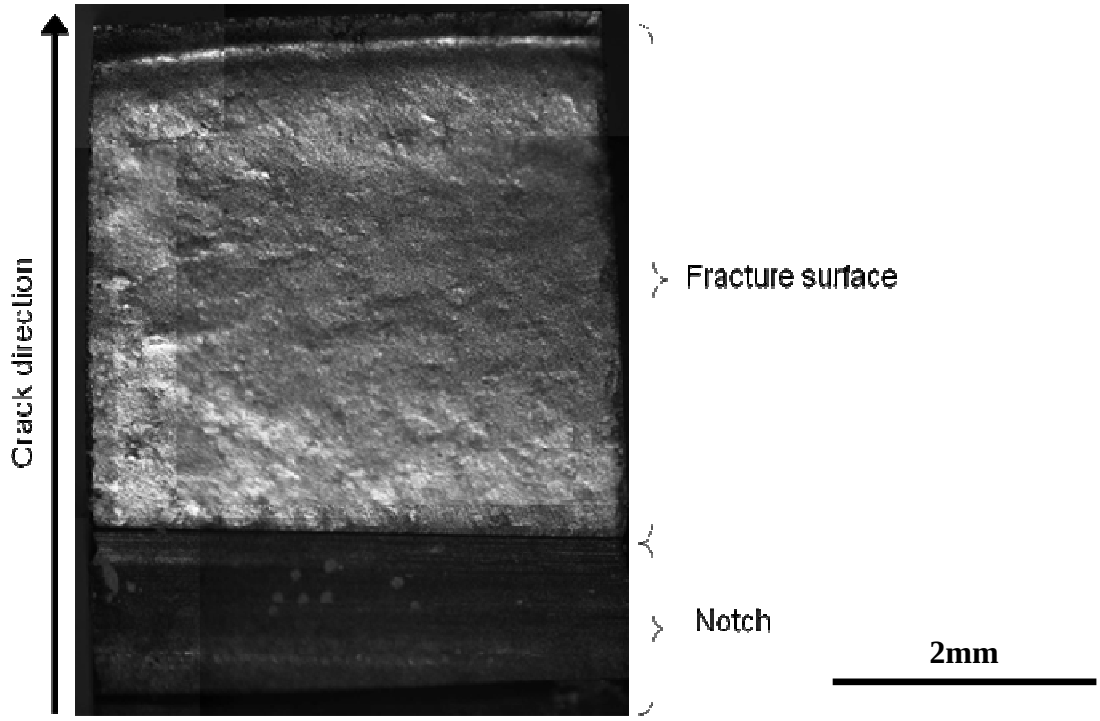


Figure 4-10: Optical image of a B_6O-NiO sample after SEVNB testing. The height of the sample is 4mm.

Although the grain size of sintered boron suboxide based materials is not accurately known, it can be estimated to be around 1µm in size. The starting

powder used when producing the boron suboxide materials was submicron prior to sintering. TEM work recorded by A. Andrews (2008) shows that there is very limited grain growth of the boron suboxide during sintering. Hence, the grain size of the sintered boron suboxide will be around one micron.

Pure boron suboxide was observed to have minimal changes in fracture planes along the surface (Figure 4-11). This is consistent with a material which exhibits transgranular fracture. For the composites examined in this study, minimal facets were observed in the boron suboxide matrix of the fracture surface. This implies that the use of additives do not change the mode of failure of the boron suboxide matrix from transgranular to intergranular. However, with the B_6O-Y_2O_3-Al_2O_3-TiB_2 sample, some intergranular fracture was observed between the additive TiB_2 phase and the matrix B_6O phase.

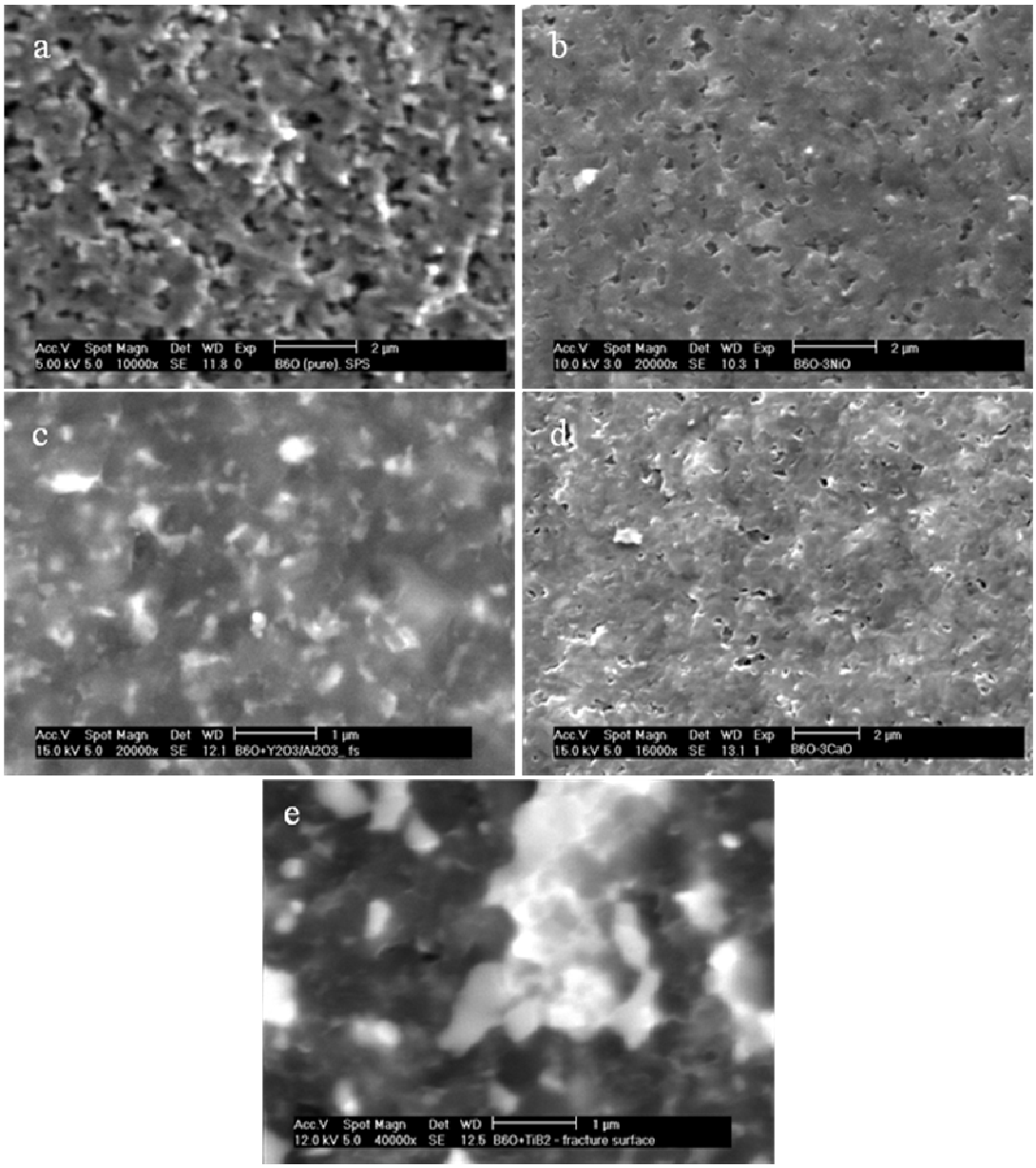
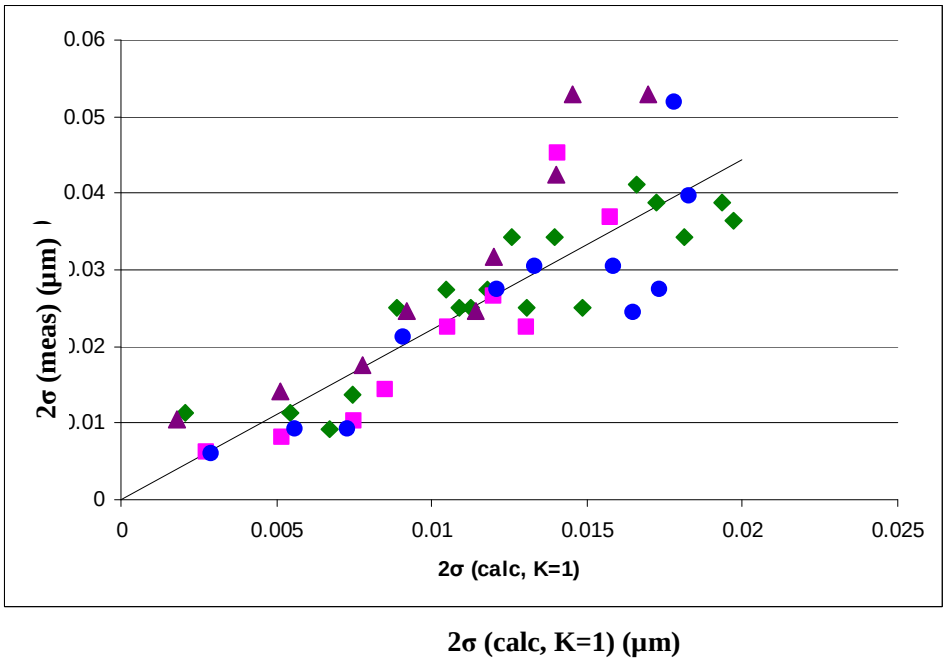


Figure 4-11: SEM images of the fracture surfaces of (a) pure B_6O; (b) B_6O – NiO; (c) B_6O-Y_2O_3-Al_2O_3; (d) B_6O-CaO and (e) B_6O – Y_2O_3 - Al_2O_3 – TiB_2

4.9 Crack opening displacement analysis

In accordance to the method laid out in Section 3.15, analysis of the crack opening displacement was performed on all of the boron suboxide composites, as well as pure boron suboxide. For each of the composites and pure boron suboxide the plots of the measured crack displacement against the calculated crack opening displacement were produced. The gradient of the linear portion of the plot gives the fracture toughness for each of the materials. An example is given for pure boron suboxide in Figure 4-12, each of the four colours represents a different crack which was analysed. The remainder of the plots are available in Appendix B.



2σ (calc, K=1) (µm)

Figure 4-12: COD analysis for pure boron suboxide

The fitted fracture toughness values are summarised in Table 4-7. Due to the fracture toughness being a result of curve fitting, rather than a result of direct measurements, R^2 is quoted, rather than a standard deviation.

Table 4-7: Fracture toughness of boron suboxide materials, determined by the COD method

Material	$K_{Ic,\ COD}$ (MPa.m$^{0.5}$)	R^2 (%)
B_6O	2.2	66.8
$B_6O – Y_2O_3$-Al_2O_3	4.3	76.5
B_6O – CaO	4.1	89.5
B_6O – NiO	3.6	88.5
$B_6O – Y_2O_3$ - $Al_2O_3 – TiB_2$	2.9	69.8

4.10 Toughening mechanisms

Using the images obtained for COD analysis, the cracks radiating from the indentation corners were examined for evidence of toughening mechanisms. Although the cracks were examined for evidence of other toughening mechanisms, the mechanisms of crack deflection, crack branching and contact bridging were examined in the most detail.

4.10.1 Angles of crack deflection

Similar to the work of Faber and Evans (1983), the angle through which the crack deflects was measured. To ensure reproducibility, a minimum of 500 deflections per sample were measured. To remove the effects of the region around the indentation, the deflections were only measured along the last two-thirds of the crack length.

Crack deflection was observed in all of the samples. The distribution of crack deflection angles are plotted in Figure 4-13. This is part of the method described in Section 3.18.

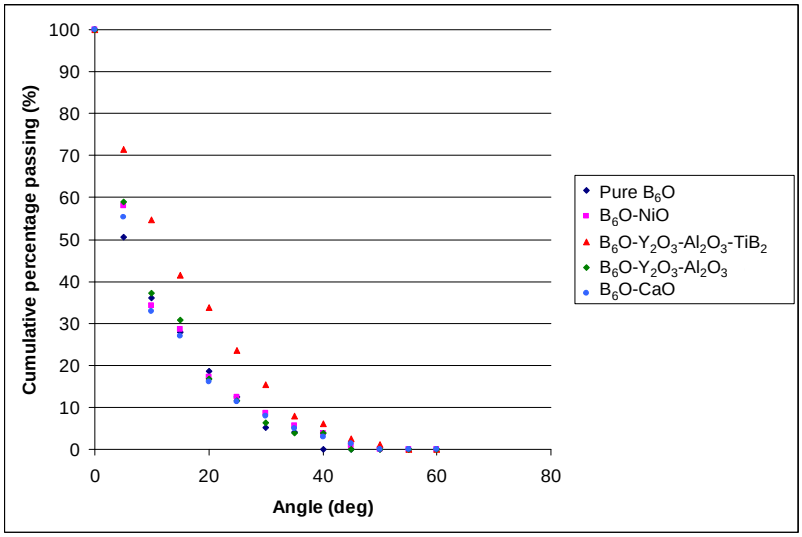


Figure 4-13: Crack deflection angles for the various boron suboxide based materials

For clarity, the region between 15 and 45° is redrawn in Figure 4-14.

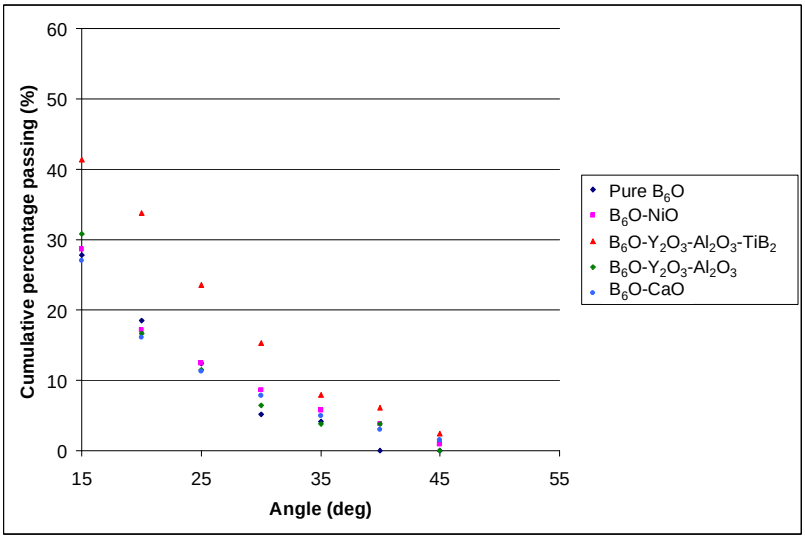


Figure 4-14: Crack deflection angles from Figure 12, redrawn between 15 and 45°

From Figure 4-13 and Figure 4-14, it can be seen that, in terms of deflection angles, it is only the B_6O-Al_2O_3-Y_2O_3-TiB_2 sample which experiences a large improvement over pure boron suboxide. Although the other composites (B_6O-NiO, B_6O-CaO and B_6O-Al_2O_3-Y_2O_3) show a general increase in the deflection angles, the improvement is slight.

4.10.2 Distance between toughening events

In order to compare the toughening mechanisms present in the various boron suboxide based materials, it is advantageous to establish the frequency with which these toughening mechanisms occur. The linear density of these toughening events along a crack was measured using SEM micrographs. Since not every crack would experience a certain type of toughening mechanism, it was not possible to quantify this length with a standard deviation. Rather, it was calculated through Equation 4-13.

$$\text{Event density} = \frac{\text{Number of events}}{\text{Total crack length}} \qquad \textbf{Equation 4-13}$$

Table 4-8 gives an indication of the average distance between two toughening mechanisms of the same type. As certain materials, especially the pure boron suboxide samples, tended to shatter near the corner of the indentation, only the last two thirds of the crack were used when determining the data in Table 4-8.

Table 4-8: Distance between toughening events in boron suboxide based materials

Sample	Crack deflection (events/μm)	Crack branching (events/μm)	Surviving ligaments (events/μm)	Frictional debris (events/μm)
Pure B_6O	1.12	Not observed[6]	Not observed	Not observed
$B_6O – Y_2O_3$-Al_2O_3	1.75	0.012	0.008	0.030
$B_6O – CaO$	1.41	0.010	0.006	0.018
$B_6O – NiO$	1.33	0.009	0.006	0.016
$B_6O – Y_2O_3$ - $Al_2O_3 – TiB_2$	2.56	0.023	0.010	0.085

As can be observed from Table 4-8, apart from crack deflection, the other toughening mechanisms occur very infrequently. Indeed, many of the toughening mechanisms were not observed in every crack. For this reason the distance between the various mechanisms often exceeds the average length of the cracks themselves (70-85μm).

[6] Frequently observed along the first third of the crack length. Never observed beyond that.

5.0 Discussion

5.1 Introduction

In this section the results presented in Section 4 are discussed.

5.2 Densification

The sintering of boron suboxide without the use of sintering aids is extremely difficult. Even at high temperatures, it is not possible to achieve a fully dense sample without applying a rather high load (Brodhag and Thevenot (1986)). It is for this reason that sintering techniques such as hot-pressing or, more recently, SPS/FAST have been used to sinter pure boron suboxide. Even using techniques such as hot-pressing or SPS/FAST, it is still not possible to fully densify boron suboxide. This is due to the presence of B_2O_3 during sintering and the substoichiometry typical of boron suboxide material.

B_2O_3 arises in a boron suboxide system due to the ease with which boron suboxide oxidises (Sasai *et al*. (2001)). B_2O_3 is present in the boron suboxide even before sintering. Andrews (2008) reports that, although washing in water or alcohol reduces the amount of B_2O_3 present, it does not remove it completely.

Complicating the analysis of B_2O_3 present in the B_6O system is that B_2O_3 reacts with moisture at room temperature to form boric acids. This boric acid will evaporate during sintering. Additionally, B_2O_3 reacts with B_6O during sintering to form $(BO)_2$ gas and amorphous boron. Even after sintering, the exact amount of B_2O_3 present in a boron suboxide ceramic is difficult to quantify, given the sub-stoichiometric nature of boron suboxide. It is for this reason that the B_2O_3 content of the sintered B_6O material was assumed to be 1.5wt%.

Although boron suboxide is often quoted as "B_6O", it would be more accurate to refer to it as "B_6O_{1-x}". Boron suboxide is often substoichiometric with respect to oxygen. Conventional methods of producing boron suboxide result in stoichiometry ranging from $B_6O_{0.72}$ to $B_6O_{0.86}$. (Hubert *et al*. (1998)) High pressure sintering can produce a higher stoichiometry of up to $B_6O_{0.98}$ (He *et al*. (2002)). The theoretical density of B_6O increases with increasing oxygen stoichiometry. $B_6O_{0.76}$ has a theoretical density of 2.49g/cm^3 and $B_6O_{1.00}$ has a calculated density of 2.59g/cm^3 (ICSD cards 81-2192 and 50-1505). For the purposes of this study, it was assumed that the B_6O based materials have a stoichiometry less than $B_6O_{0.90}$. This upper limit has a density of 2.55g/cm^3. Since the stoichiometry which was assumed is higher than typical hot-pressed methods achieve, the degree of sintering in the boron suboxide based samples is probably higher than suggested by comparing the measured and theoretical densities.

Previous work in the sintering of boron suboxide materials has shown that adding a secondary phase, which is liquid at B_6O's sintering temperature, improves the density and lowers the porosity of the resulting composite. Successful liquid phase sintering aids include Al_2O_3, Y_2O_3-Al_2O_3, Co and Ni (Shabalala (2008), Andrews (2008), Johnson (2008), Ogunmuyiwa (2008) and Herrmann (2009)). The liquid phase sintering aids used in B_6O ceramics can be divided into two categories, based upon whether the sintering aid is crystalline or glass at room temperature.

The sintering aids which are crystalline after sintering generally consist of the group 4-8 transition group metals. After sintering these sintering aids are generally borides, regardless of whether their starting composition is free metal, oxide or boride. For the transition metal sintering aid examined in this study (B_6O-NiO), the final form of the additive is the simple boride, NiB, which agrees with the work of Ogunmuyiwa (2009) and is predicted thermodynamically by Herrmann (2009).

The sintering aids which form glasses after sintering are generally the oxides of alkali earth metals and the oxides of aluminium, silicon, yttrium and other rare earth elements. These glass formers react with the B_2O_3 present in the B_6O to form a complex borate glass. (Ogunmuyiwa (2009), Johnson (2008) and Andrews (2008)). For higher percentages of additive (greater than about 3wt%), crystallisation of the secondary phase can occur (Herrmann, unpublished (2010)). The borate glass contained some MgO contaminant which was present in the

amorphous boron used by the IKTS to produce the boron suboxide powder. In this study, the composites B_6O-Y_2O_3-Al_2O_3, B_6O-Y_2O_3-Al_2O_3-TiB_2 were expected to form a Y_2O_3-Al_2O_3-B_2O_3-(MgO) glass. The B_6O-CaO composite formed a CaO-B_2O_3-(MgO) glass. As mentioned previously, the exact B_2O_3 and MgO content of the glass is unknown. From the XRD traces, no crystallisation was detected. Hence, the B_2O_3 content must be sufficient in order to form a stable glass. For both the B_6O-Y_2O_3-Al_2O_3 and the B_6O-Y_2O_3-Al_2O_3-TiB_2 composites, the B_2O_3 content of the glass can range between 49-65mol% (based on the work of Chakraborty *et al.* (1986)). For the B_6O-Y_2O_3-Al_2O_3 composite, this is equivalent to between 2.3 and 4.5wt% B_2O_3 in the composite. This is a very large amount of B_2O_3 present in the B_6O system. The discrepancy can be explained however. Firstly, the MgO contaminant is a glass stabiliser, so it will reduce the amount of B_2O_3 required to produce a stable Y_2O_3-Al_2O_3 glass. Secondly, in small triple junctions and thin films along the grain boundaries, crystallisation is retarded. This will stabilise the glass phase, even for a much lower content of glass formers (such as B_2O_3) (Clarke (1987)).

Although liquid phase sintering does serve to improve the density and reduce the porosity of the sintered product, it is not without drawbacks. At room temperature, the sintering additives, whether crystalline or amorphous, generally have inferior properties compared to the B_6O matrix. For example, in terms of elastic modulus, the crystalline phase NiB has an elastic modulus of 254GPa (Smolin *et al*. (1984)), while the glassy CaO-B_2O_3 phase has an elastic modulus of up to 102GPa (Manupriya *et al*. (2006)). These values are low compared to the elastic modulus

of the B_6O matrix of 540GPa (Shabalala (2008)). However, the secondary phases can also improve the mechanical properties of the sintered composite by wetting the grain boundaries or introducing residual stresses into the ceramic. These changes made by the secondary phase can prove beneficial to the fracture toughness of the material.

Liquid phase sintering aids are not the only additives that can be used to alter a ceramic system. Additives which are still solid at the matrix's sintering temperature can also be used. However, solid state sintering does not affect the density and porosity to the same extent as liquid phase sintering (German (1996)). Generally, solid phase additives are chosen to either introduce a new material property, or to enhance an existing one. For example, Sasai *et al*. (2001) introduced diamond into a B_6O matrix in order to increase the composite's hardness. The introduced diamond, however, did not increase the fracture toughness of the composite to any great extent (maximum fracture toughness recorded was less than $1MPa.m^{0.5}$). Similarly, the addition of B_4C into a B_6O matrix by Itoh *et al*. (2000) did not increase the fracture toughness of the composite above $1MPa.m^{0.5}$. Herrmann *et al*. (2009) added TiB_2 to a B_6O matrix in order to increase the electrical conductivity of the composite. However, rather than rely solely on solid state sintering, Herrmann *et al*. included a Y_2O_3-Al_2O_3 phase in order to assist with densification. Additionally, based upon the work of Shabalala (2008) and Andrews (2008), the Y_2O_3-Al_2O_3 phase was expected to increase the fracture toughness of the resulting composite. It was this work upon which the B_6O-Y_2O_3-Al_2O_3-TiB_2 sample was produced.

The presence of porosity plays an important role in determining the material properties of the sintered product. Porosity can result from incomplete sintering. Post-sintering machining operations can introduce surface porosity to the ceramic. If the ceramic is subjected to aggressive grinding, or if the grains in the ceramic are weakly bonded, it is possible to introduce porosity on the surface of the ceramic. Introducing porosity in this manner will increase the amount of open porosity measured. Additionally, the introduced porosity can affect property measurements if the technique uses the surface for its measurement (for e.g., hardness and IFT). In solid state sintering, porosity can be stable if the pores are large compared to the grain size, or if there is high gas pressure within the pores. For the pure B_6O material produced by SPS under vacuum, the porosity can generally be attributed to incomplete densification due to the difficulty in sintering boron suboxide without a sintering aid.

The final density of the material can be improved by the presence of a liquid phase sintering aid. Liquid phase sintering can be divided into three sections. Rearrangement of the grains into a better packing arrangement happens when the liquid phase melts. Solution-precipitation of the matrix material improves densification and increases overall grain size. In the final stages of sintering, the liquid sintering aid fills the stable pores by capillary action. This can be observed in the composites by a 36% reduction in the porosity between pure B_6O and B_6O-CaO, the composite with the highest porosity.

5.3. Hardness

5.3.1 Hardness of boron suboxide materials with additives

The hardness of the boron suboxide materials is lower than expected from previous work on boron suboxide materials. For example, for boron suboxide sintered with 1.1vol% of NiO, (Ogunmuyiwa, (2008)) reported a hardness of 27.1±2.1GPa. Comparatively, the B_6O-NiO sample examined in this study has a hardness of 21.8±2.3GPa. A portion of this discrepancy can be attributed to the improved distribution of the secondary phases of the newer boron suboxide materials (Johnson, private communication (2010)). Due to the segregation of the secondary phase, in the samples of Ogunmuyiwa, the indentation left behind by a Vickers indenter had a much higher probability of being on an area of harder boron suboxide, rather than a softer secondary phase region. Other contributing factors may include the difficulty in polishing certain samples (the B_6O-NiO sample in particular).

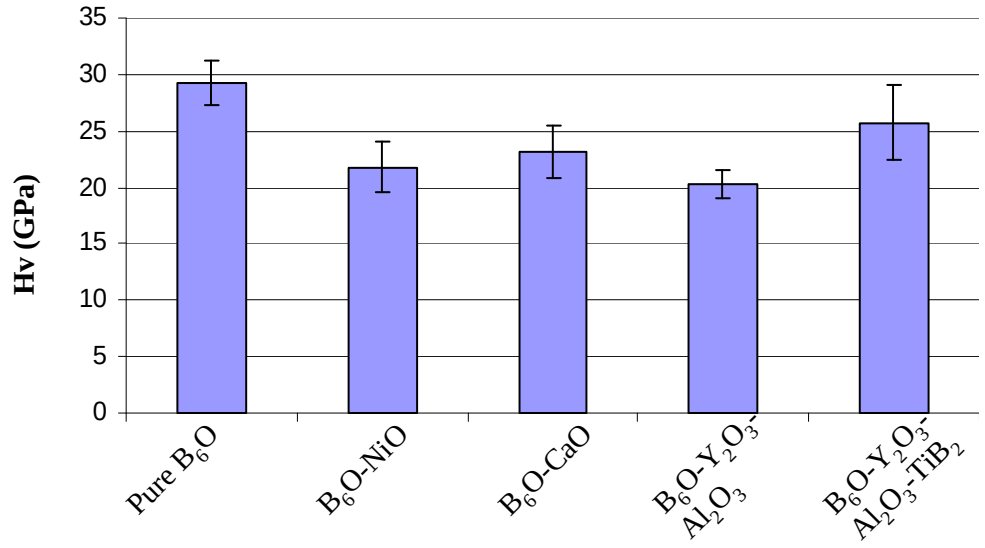


Figure 5-23: Comparison of the hardness of the SPS sintered boron suboxide materials

In terms of hardness trends, the B_6O-NiO and B_6O-CaO composites have a lower amount of secondary phase (1.0 and 3.2vol% respectively) and so have a higher hardness than the B_6O-Y_2O_3-Al_2O_3 composite. It was not expected that B_6O-NiO would be softer than the B_6O-CaO material. The crystalline NiB phase in B_6O-NiO is harder than the glassy CaO-B_2O_3 phase in B_6O-CaO. Additionally, B_6O-CaO has a larger content of the secondary phase, so it is expected that B_6O-NiO will be closer to the hardness of pure B_6O than B_6O-CaO. This discrepancy arises due to the difficulty in polishing the B_6O-NiO, which leads to an increased surface porosity of the sample (Section 4.2.2). Since porosity offers no resistance to an indenter, the measured hardness is lower than if there was no porosity. Additionally, the deviation between the B_6O-Y_2O_3-Al_2O_3 and the B_6O-Y_2O_3-Al_2O_3-TiB_2 materials was unexpected. As the B_6O-Y_2O_3-Al_2O_3 material has a

lower proportion of B_6O than the B_6O-Y_2O_3-Al_2O_3-TiB_2 material, it was expected that the B_6O-Y_2O_3-Al_2O_3 possess a higher hardness value. This was not observed.

5.3.2 Indentation size effect

There is no one standard method to measure the hardness of any material, for example the standard for testing ceramics using a Vickers indenter is ASTM C1327-03, while using a Knoop indenter follows ASTM C1326-03. A wide range of hardness testing systems (for example the Knoop and Rockwell systems) exist and the hardness values obtained by these measurements are not directly comparable. The issue is further compounded by the fact that within each measurement system, there are parameters which change the measured hardness. Notably, the change in load for a Vickers indentation test will change the measured hardness. While there is a range of data available on the hardness of boron suboxide, this data was determined under a range of loads, making it difficult to compare different hardness values reported.

The indentation size effect is usually quantified by the Meyer's law (Equation 5-1) (Stevenson *et al*. (2002)). Where, "P" is the load, "K" is a material constant, "D" is the diameter of the indentation. The Meyer's index, "n", is used as a measure of the ISE.

$$P = KD^n \qquad \textbf{Equation 5-1}$$

The power in Meyer's law describes the extent to which a material experiences the ISE, the greater the deviation of the power from the value of 2, the greater the ISE. It was shown in Section 4.3.2 that the hot-pressed B_6O material has a power of 1.76. This means that B_6O experiences a large ISE. In turn, this means that great care must be taken in comparing hardness values determined at different loads.

To illustrate size of boron suboxide's indentation size effect, a comparison to the ISE of other materials is made. The work of Gong *et al*. (1999) examined a range of materials for indentation size effect. In their work, it was found that soda lime glass had a "n" value of 1.860; sintered TZP of 1.970; sintered Al_2O_3 of 1.892; sintered SiC of 1.790 and hot-pressed SiC whisker reinforced Si_3N_4 a "n" value of 1.826. TZP and Al_2O_3 have a very limited ISE, but SiC is cited as having a substantial ISE. B_6O has a larger ISE than even SiC.

It is possible to fit a curve to the ISE graph in Figure 4-15 (Section 4.3.2). Using this curve, the hardness data obtained in literature can be altered to a single load, making the data more comparable. However, this should be done only with caution. The ISE that a material experiences can change if there are changes to the system. The ISE depends upon the grain size of the material, the level and type of

impurities present and, of special importance for boron suboxide materials, the stoichiometry of the material.

Table 5-1: Comparison of hardness values of literature and this study for pure B_6O

Author	Original load (kg)	Original hardness (GPa)	Hardness with load altered to 0.5kg
Andrews (2008)	0.5	35	35.0
Shabalala (2008)	1.0	30.1	32.6
Elison-Hayashi (1994)	0.1	38	31.5
Kayhan and Inal (1999)	0.1	36	29.9
He *et al*. (2002)	0.1	45*	37.3
This study (hot-pressed)			34.1

*Single crystal

As can be seen from Table 5-1, if the ISE was not taken into account, the values obtained by Kayhan and Inal (1999) would seem to be higher than those of the

samples produced by Shabalala (2008). However, when changing the base load, Kayhan and Inal's material is softer. This is likely as the work of Kayhan and Inal contained significant porosity.

Care should be taken with the interpretation of the hardness values of He *et al.*'s (2002) single crystal. As the stoichiometry is different to hot-pressed boron suboxide, it may experience a different ISE. Additionally, the hardness of single crystal materials is affected by the crystallographic plane and the crystallographic direction the testing was done in. Since He *et al*. reported neither the plane, nor the direction the testing was performed in, it is not known how this will affect the ISE of the material. For these reasons, the ISE which single crystals of boron suboxide experiences would need be determined by indentation experiments on single crystals themselves. However, as an illustratory example, if the ISE for polycrystalline boron suboxide was applied to monocrystalline boron suboxide, then it can be observed (from Table 5-1) that there would be a significant decrease in the measured hardness when using a higher load.

5.4 Comparison of fracture toughness data

The fracture toughness of the boron suboxide materials were examined through three different techniques; the indentation fracture toughness (IFT), the single edge V-notch beam test (SEVNB) and the crack opening displacement analysis

(COD). These techniques were examined, not only to develop a comparison between the three different techniques, but also to compare the results with work previously performed.

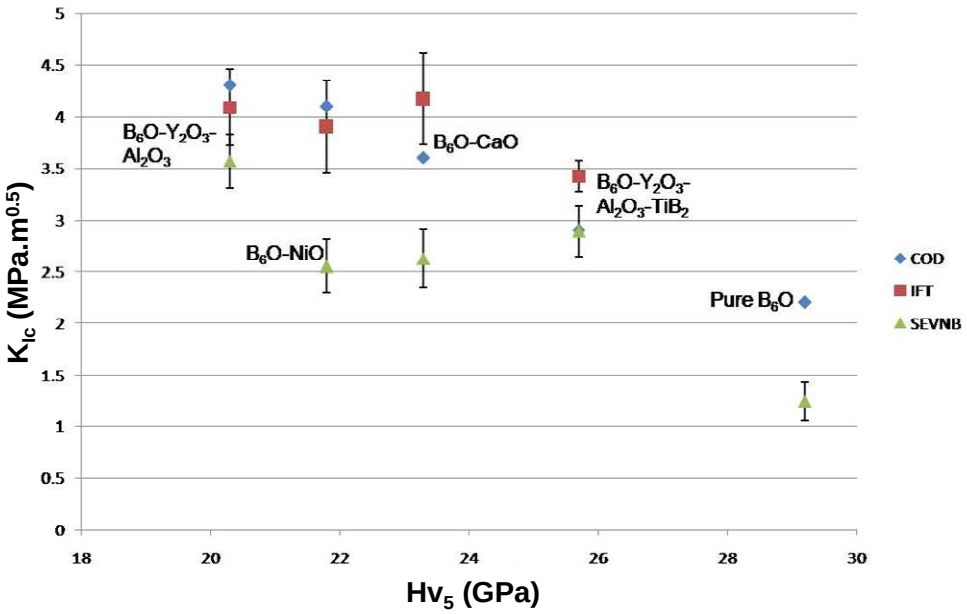


Figure 5-2: Fracture toughness data for pure boron suboxide with and without different sintering additives. Note that pure B_6O was tested under a 1kg load

Figure 5-2 shows the fracture toughness values of the boron suboxide materials with and without sintering aids plotted against their relative hardness values. There are no error bars for the COD analysis as the deviation of the COD was calculated as a R^2 value rather than a standard deviation. Pure boron suboxide was too brittle to maintain an indentation for IFT purposes.

Immediately evident from examining the SEVNB data in Figure 5-2 is that all of the four composites examined have a far higher fracture toughness than pure boron suboxide. Although this is in agreement with the work of Shabalala (2008), Andrews (2008), Johnson (2008) and Ogunmuyiwa (2009), it is remarkable that such a large increase in fracture toughness can occur with such small amounts of secondary phase. For a 1% addition of CaO to boron suboxide, an increase in fracture toughness of 177% occurs. Also evident is that the B_6O-Y_2O_3-Al_2O_3 composite is tougher than the B_6O-Y_2O_3-Al_2O_3-TiB_2 sample. This is unexpected as the B_6O-Y_2O_3-Al_2O_3 sample contains 3.7 vol% of Y_2O_3-Al_2O_3-B_2O_3, while the B_6O-Y_2O_3-Al_2O_3-TiB_2 contains 4.8 vol% of Y_2O_3-Al_2O_3-B_2O_3 and 19.8vol% TiB_2, a far tougher phase than B_6O. The reasons for the increase in fracture toughness values are explained in Section 5.5.

The effect of the additives on the fracture toughness of boron suboxide materials is not only dependent on the amount of additive present. As can be seen from Figure 5-3, there is no evident relationship between the measured fracture toughness and the additive content. This means that the properties of the final phases of the additives have some effect on the fracture toughness of the materials.

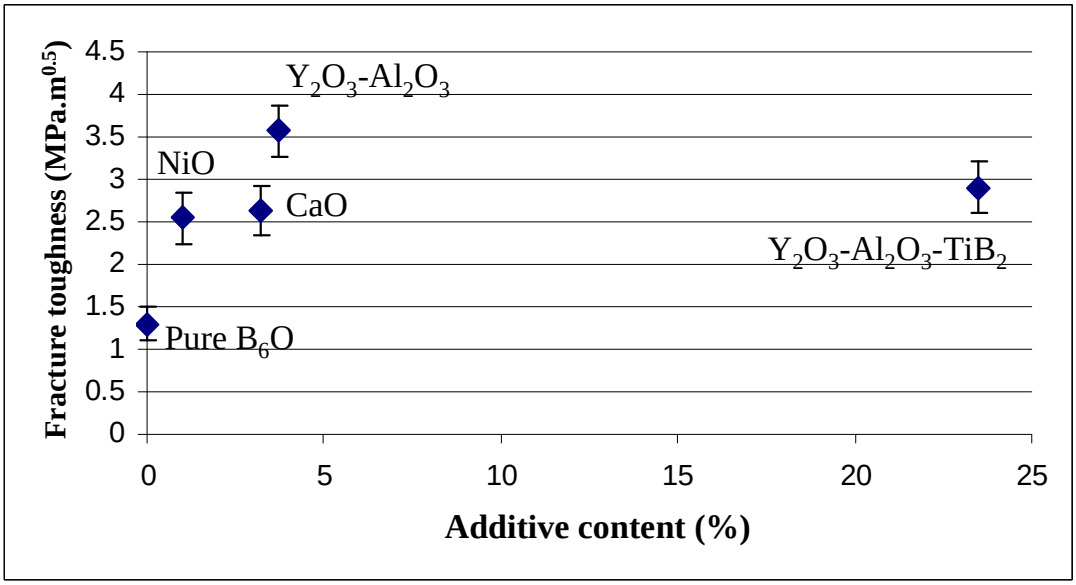


Figure 5-3: SEVNB fracture toughness of boron suboxide materials as a function of additive content

Of the three methods used to obtain fracture toughness measurements, the SEVNB is most likely to be closest to the true fracture toughness of the boron suboxide materials. SEVNB testing has been proven to be a reliable, reproducible test method with high accuracy. The crack opening displacement test is a new testing method and has yet to undergo extensive trials. As of yet, the only published data on the COD method is Fett *et al.*'s (2005) work on Si_3N_4. Additionally, this method is more likely to yield the toughness at the crack tip. Determining the fracture toughness by the IFT method is always more of an approximation than a measurement. The oft cited failures of the IFT method are its large inaccuracy and imprecision (Evans, 1976). For these reasons, the SEVNB test will be used as the reference when comparing the other testing methods.

The deviation between the COD analysis and the SEVNB data is inconsistent. The deviation ranges between very large values for pure B_6O (64.2%) and B_6O-NiO (60.8%) to a negligible deviation of 0.3% for B_6O-Y_2O_3-Al_2O_3-TiB_2. This deviation is related to the microstructure of the samples.

The COD method was intended for use in the region directly behind the crack tip (Fett *et al*. (2005)). As the distance from the crack tip increases, the relationship between the crack opening and the distance from the crack tip can no longer be related to the fracture toughness through Fett's Equation. Although Fett *et al*. used the COD method to determine the fracture toughness of individual silicon nitride grains, for boron suboxide, this was not possible. As boron suboxide is exceedingly difficult to etch (Kharlamov (2002)), it was not possible to establish where one grain ended and another began. Additionally, due to the brittleness of the matrix a crack would not arrest within a B_6O grain. Rather, a crack would arrest within a pore, or for B_6O-Y_2O_3-Al_2O_3-TiB_2, within a TiB_2 grain.

It is this location of crack arrest which causes the deviation between the SEVNB data and the COD analysis. As predicted by Fett's Equation, a tougher material will have a wider crack opening near the crack tip than a brittle material would. Since most of the cracks arrested in pores, it was not possible to establish exactly where the crack should have ended if not for the porosity. Thus, the last known location of the crack, where the crack entered the pore, was taken as the crack tip. However, this position would have a larger crack opening than the real crack tip

would. This would bias the calculated fracture toughness to larger values. For the B_6O-Y_2O_3-Al_2O_3-TiB_2 sample, the crack would arrest within a TiB_2 grain. This allowed for more accurate determination of the position of the crack tip. In turn, this produced far more accurate COD measurements. These are the reasons behind the trend of Figure 5-4 where the deviation between the COD data and the SEVNB data increases with increasing sample porosity.

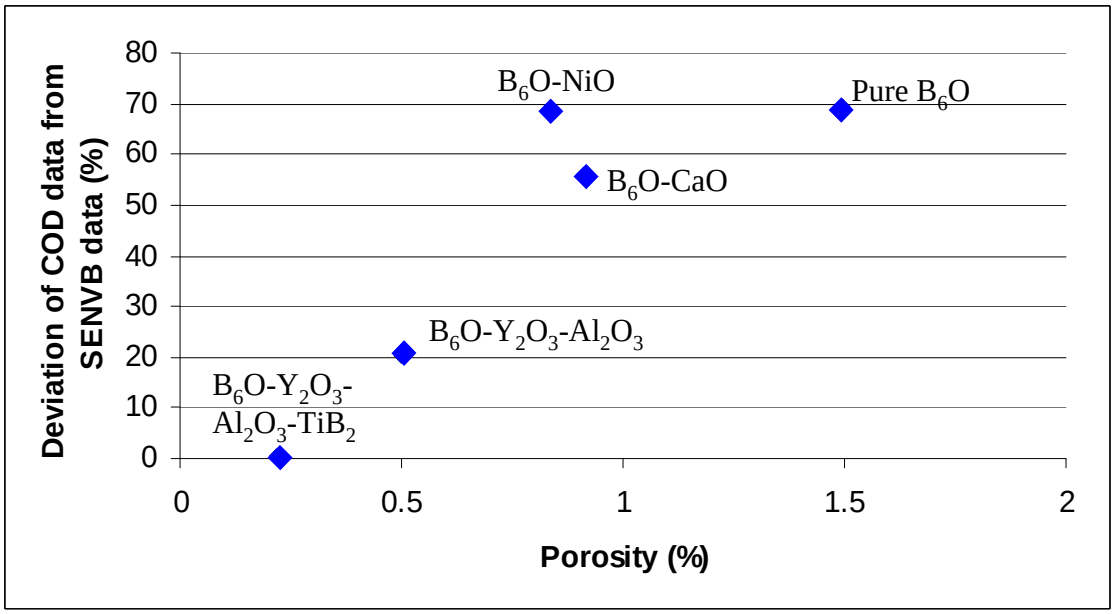


Figure 5-4: Effect of open porosity upon the COD measurements deviation from SEVNB measurements

From Figure 5-2, it is evident that the IFT method overestimates the fracture toughness of all the boron suboxide materials. The over-estimate ranges from 58.5% for B_6O-CaO to 14.6% for the B_6O-Y_2O_3-Al_2O_3 composite. This deviation is consistent with the reported inaccuracy of the IFT method. As the deviation

between SEVNB data and IFT data is not constant, it is not possible to say by what margin other samples, outside of the samples tested, will be over-estimated. The deviation of the IFT data will not be affected by the crack tip being arrested in the porosity in the sample to the same degree as for the COD analysis. The length of a crack which was not arrested in a pore would not exceed the length of a crack which was by a large margin. This is due to the reduced stress applied to the crack tip due to the distance between the crack tip and the indentation. As the IFT method uses the entire crack length for its measurements, this dampens the effect of crack tip arrest in porosity.

However, as the IFT is a near surface technique for measuring fracture toughness, it can be affected by the sample preparation during polishing. With samples which are difficult to polish, the polishing procedure can, partially or fully, break grains out of the surface of the material. This break-out will cause an increase in the measured fracture toughness by the IFT method.

Although others (Shabalala (2008), Andrews (2008), Johnson (2008) and Ogunmuyiwa (2009)) have studied similar composites and have also used the IFT method to report fracture toughness, it is not possible to revise their efforts to give a more accurate indication of fracture toughness. This is not only due to the inconsistency of the IFT testing method between samples, but also due to the variability of the testing method between operators. However, in all likelihood,

the above authors' fracture toughness data for the various composites are over-estimated, despite the margin of the over-estimation being unknown.

The work on B_6O-Y_2O_3-Al_2O_3 fits in with the work at the IKTS on the effect that the volume content of secondary phase has on the fracture toughness of the boron suboxide materials (Herrmann (2010)). B_6O materials with varying Y_2O_3-Al_2O_3 additions were produced and tested for fracture toughness at the IKTS. The general trend is observed in Figure 5-5. Initially, for a very small addition of yttria-alumina, there is a large increase in the fracture toughness of the material (part I in Figure 5-5). Then increasing the volume content has minimal effect upon fracture toughness. After a certain point (approximately 3 vol%), the fracture toughness appears to increase again (part III in Figure 5-5).

The second region in the Figure can be explained by examining the likelihood of a crack encountering the secondary phase. The glassy yttria-alumina-borates which will form will occupy the triple points within a B_6O ceramic. The likelihood of a crack intercepting a portion of the yttria-alumina addition is proportional to the number and volume of triple points. Increasing the volume content of yttria-alumina will not increase the number of triple points. Assuming a spherical triple point, the size of the triple point will only increase by the cubed root of the volume content. This means that increasing the volume content of the secondary phase will only slightly increase the likelihood of a crack interacting with the

secondary phase. This explains the slight increase observed between 1 and 3 vol% in Figure 5-5.

Beyond a certain amount of yttria-alumina, the glass is no longer stable. This will cause some of the yttria-alumina borates to crystallise. The transformation of the additive into a stiffer phase will increase its effect on the fracture toughness of the material. This is what occurs in the third region of Figure 5-5. The explanation behind the first region in Figure 5-5 will be explained in Section 5.5.

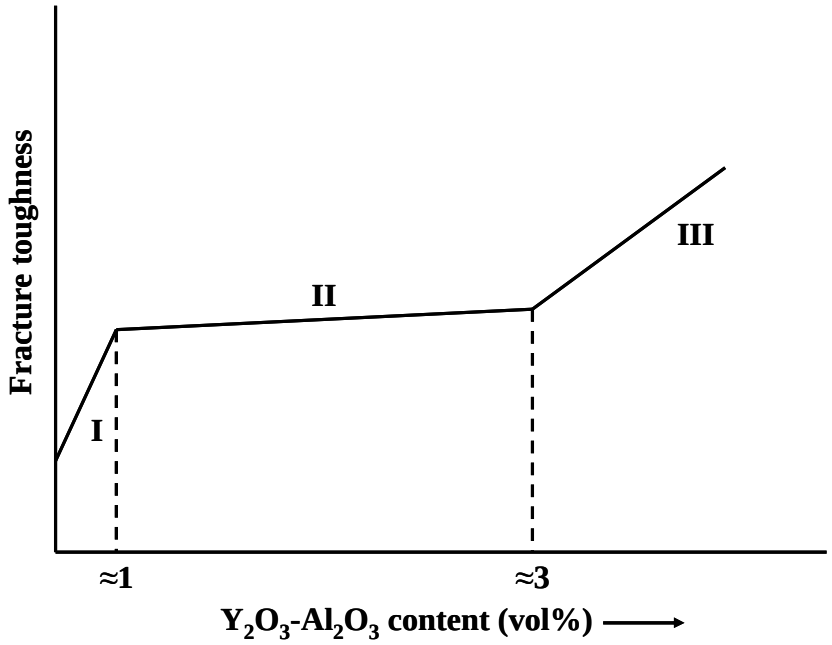


Figure 5-5: Schematic plot of trend of the effect of Y_2O_3-Al_2O_3 content upon the fracture toughness of boron suboxide materials. (Herrmann (2010))

5.5 Toughening mechanisms

Ceramic materials possess the highest elastic moduli and hardness values of all of the material classes. However, the applications of ceramic materials are often limited by their low fracture toughness (Roesler *et al*. (2007)). Often, secondary phases will be added to a ceramic in order to produce a composite which has lower hardness and elastic modulus, but a higher fracture toughness than the pure ceramic would. In order to be able to design materials for specific applications, it is important to understand how the increase in fracture toughness arises in the ceramic.

The critical stress required in order for an existing crack to grow can be given by Equation 5-2. Where: “E” is the elastic modulus of the material, “c” is the length of the existing flaw and “γ” is the surface energy of the ceramic.

$$\sigma_f = \sqrt{\frac{2E\gamma}{\pi c}} \qquad \textbf{Equation 5-2}$$

Direct application of Equation 5-1 would show that in order to increase the critical stress required for fracture an increase in the surface energy or the elastic modulus of the ceramic is needed. However, as mentioned previously, the secondary phases present in boron suboxide composites usually have a lower elastic modulus

compared to B_6O. Hence, these secondary phases must contribute to the fracture toughness of a material through a different mechanism.

It is sometimes useful to use an energy release rate Equation (Equations 5-3 and 5-4). “G” is the crack energy release rate (with respect to distance) and “R” is the crack growth resistance. The “R” values changes if the material experiences R-curve behaviour.

$$G = \frac{\pi\sigma^2 c}{E} \qquad \textbf{Equation 5-3}$$

$$R = 4\gamma \qquad \textbf{Equation 5-4}$$

The minimum crack energy release rate (“G”) required for crack growth is the energy required by the crack growth resistance (“R”). Based upon Equations 5-2, 5-3 and 5-4, the reasons behind the increase in the fracture toughness of boron suboxide materials will be explained.

5.5.1 Crack branching

One method to increase the fracture toughness of a material is to increase the length of the crack, while keeping the penetration of the crack into the sample constant. This would increase the energy required for crack growth as the crack

would require additional energy to form the additional surfaces. There are two methods to accomplish this. The first is crack branching.

In materials without a grain structure, crack branching is energetically possible if the energy release rate (G) ever exceeds twice the crack growth resistance, R. Since the energy release rate often increases with increasing crack length, glasses often experience crack branching at a certain distance from the crack origin. For materials with a microstructure, the microstructure can interact with the applied stress field to produce two planes which lie across local maxima in the tensile stress. This allows for a single crack to branch into two separate cracks. (Wachtman, 2009)

The energy dissipated by a branched crack is associated with the formation of the surface of the two cracks. Logically, if the material is homogeneous and a crack branches into two cracks, the energy expended to grow both cracks the same distance is twice that of one crack.

In the boron suboxide materials, crack branching is not a very common event. Branching usually occurred in or nearby the secondary phases. Figure 5-6 gives an indication of the length of a secondary crack resulting from crack branching. In the B_6O-Y_2O_3-Al_2O_3-TiB_2, where branching is the most common, branching only happens, on average, every 42µm. The observed crack branches were also not

long in length, much less than 1µm in length. If the length of the secondary crack was taken to be 1µm (an exaggeration), then the increase in crack length would only be 2.3%.

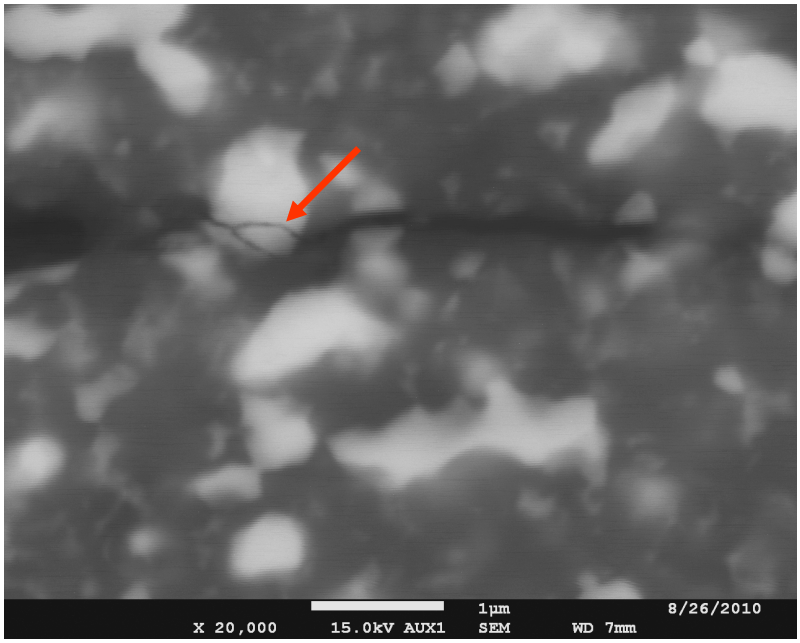


Figure 5-6: Crack branching in the B_6O-Al_2O_3-Y_2O_3-TiB_2 sample.

Since crack branching occurs so infrequently in boron suboxide materials and, when it does occur, the length of the secondary crack is small, the total increase in crack length due to crack branching will be small. This means the increase in energy associated with the creation of new surfaces will also be small. Hence, the large increase in fracture toughness between the boron suboxide composites and pure boron suboxide cannot be explained in terms of crack branching alone.

5.5.2 Crack deflection

The second method of increasing the fracture toughness by increasing the length of the crack, but retaining the depth of penetration, is by crack deflection. Crack deflection can occur when the crack tip encounters an inhomogeneity in either the ceramic's microstructure or the local stress field.

An inhomogeneity in a ceramic's microstructure can include grain boundaries. If the intergranular interface is weak enough, a crack will deflect along the grain boundary, rather than shear the grain. It is for this reason, together with the disruption of the slip planes that polycrystalline materials have a fracture toughness of up to twice that of the single crystal (Wachtman (2006)).

However, this does not apply to boron suboxide. Pure boron suboxide experiences transgranular fracture. A crack approaching a grain in a boron suboxide ceramic would shear the grain, rather than deflect around it. This can be interpreted as boron suboxide having good intergranular bonding. This is validated by the work of Kleebe (2008) whose TEM images show clean, well bonded grain boundaries between adjacent grains of B_6O.

The crack deflection which is observed in pure boron suboxide is uncommon (Section 4.10). This defection is generally associated with impurities and porosity,

rather than any grain boundaries. This is illustrated in Figure 5-7. In this respect, pure boron suboxide fractures in a similar fashion to most glasses.

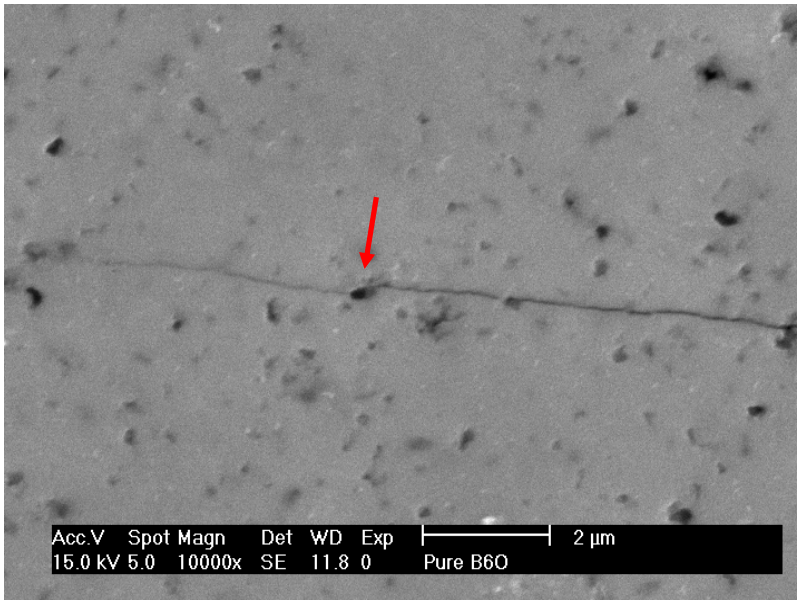


Figure 5-7: Crack deflection around a pore in pure boron suboxide

Compared to pure boron suboxide, the boron suboxide materials with additives exhibit a great deal more crack deflection, not only in terms of quantity, but also in terms of the steepness of the deflection angles. While pure boron suboxide has a crack deflection density of 1.12 deflections per micrometre, the composites have a crack deflection density of between 1.33 (for B_6O-NiO) and 2.56 (for B_6O-TiB_2). This is shown in Figure 5-8. Thus, crack deflection process may play a larger role in toughening of the composites compared to pure boron suboxide.

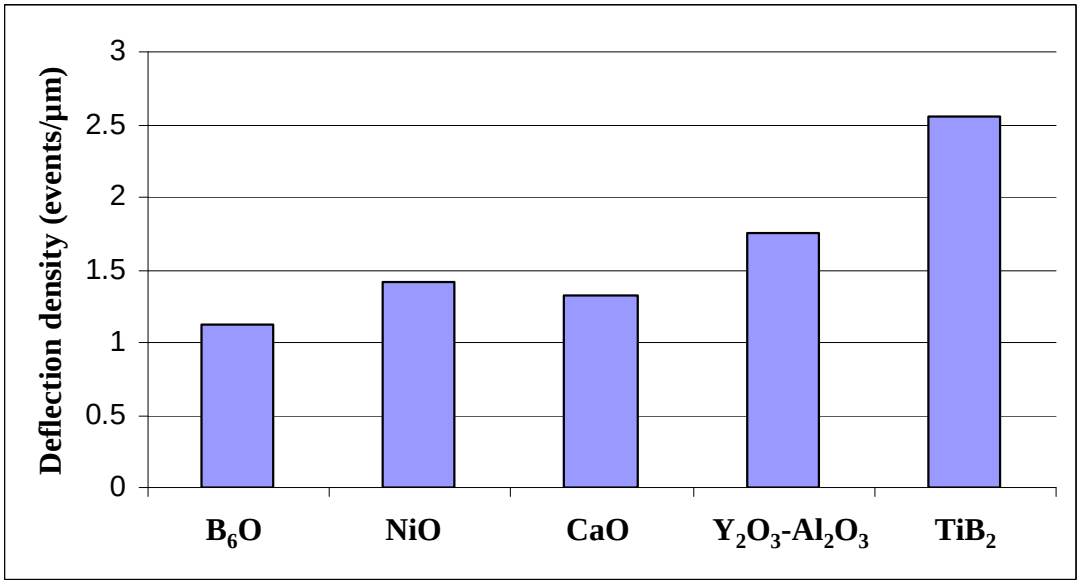


Figure 5-8: Crack deflection density for the boron suboxide materials

In 1983, Faber and Evans published a paper in which the effect that crack deflection around a secondary particle has on fracture toughness is explained. Three generic geometries of the secondary particle were examined, the sphere; the disc and the rod. Faber and Evans explain that fracture toughness is not only affected by the amount of crack which occurs, but also the angle at which these deflections occur. The greater the number of deflections which occur and the higher the angle of deflection out of the plane of the crack, the greater the degree of toughening. For each of these three geometries the increase in relative fracture toughness was calculated as a function of volume fraction of the secondary phase. For the spherical geometry the maximum increase in fracture toughness was about twice that of the pure composite; for the disc, approximately 3.5 times and for the rod geometry, the increase could be as much as 4 times the original fracture toughness.

Although the secondary phases present in boron suboxide composites do not lend themselves to such classical geometries as described by Faber and Evans, the secondary phases could be most closely approximated by the spherical geometry. Although Faber and Evans do predict an increase in fracture toughness of up to twice the original for spherical secondary particles, and although the increase in fracture toughness of the composites is a least twice that of the pure boron suboxide, the increase in fracture toughness of the composites cannot be explained by deflection processes alone.

The maximum increase in fracture toughness predicted by Faber and Evans corresponds to a high volume fraction (between 30 and 40%) of the secondary phase. The volume fraction of the secondary phases in the B_6O composites is far lower than 30%. The total volume of the secondary phases (including B_2O_3) in the B_6O materials is 3.2% for B_6O-CaO; 4.8% for B_6O-NiO; 3.7% for B_6O-Y_2O_3-Al_2O_3 and 23.5% for the B_6O-Y_2O_3-Al_2O_3-TiB_2 composite. An additional discrepancy between the work of Faber and Evans and the current composites is that the calculations of Faber and Evans were based upon the crack deflecting around every particle it encounters along its path. This does not happen in the boron suboxide composites. As an illustration of this, Figure 5-9 shows a crack in the B_6O-Y_2O_3-Al_2O_3-TiB_2 sample which has sheared several TiB_2 grains.

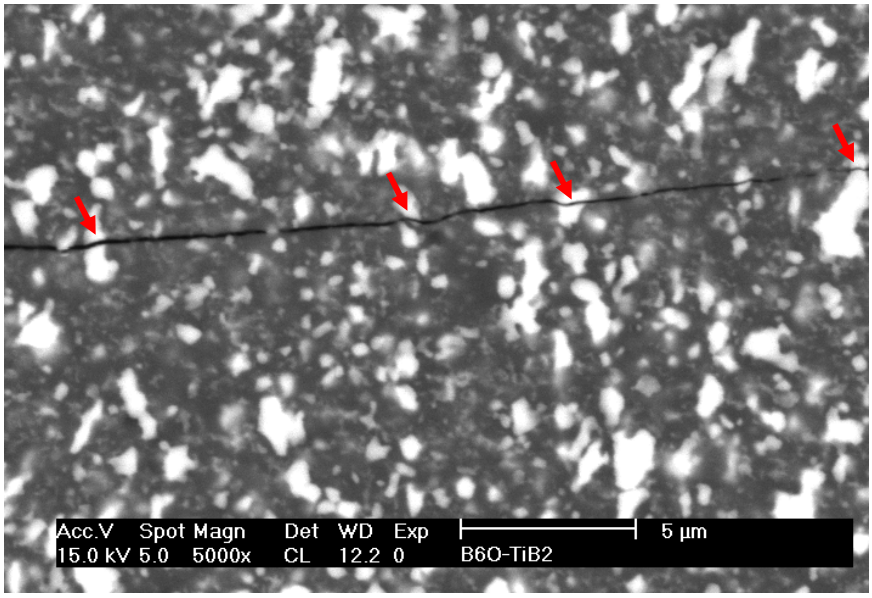


Figure 5-9: A crack running through the B_6O-Y_2O_3-Al_2O_3-TiB_2 sample. The red arrows indicated where the crack has sheared a TiB_2 grain.

The angles of crack deflection present a further discrepancy. In the current composites, when the crack does deflect, the angle of deflection is not much greater than that for pure B_6O. For the B_6O-CaO, the B_6O-NiO and the B_6O-Y_2O_3-Al_2O_3 samples, the only significant improvement in the deflection angles lie between 5 and 10°. For all angles greater than 10°, the deflection angles are very close to that of pure boron suboxide (see Figures 4-11 and 4-12, Section 4.10.1).

Crack deflection does not necessarily happen only along interfaces in the composites as assumed by Faber and Evans. Crack deflection can also result from the crack tip experiencing inhomogeneities in the local stress field. As the different additives in the boron suboxide composites have different coefficients of

thermal expansion (CTE) to the boron suboxide matrix, residual stresses will be set up in the material. These residual stresses can interact with the applied tensile stress to produce a stress field where local stress maxima exist.

Depending upon the size of the secondary phase's CTE compared to the CTE of boron suboxide, the residual stress in the additive can be either compressive or tensile. If the CTE of the additive is larger than that of boron suboxide, tensile residual stresses are established within the additive particle. Conversely, a CTE smaller than that of boron suboxide will produce a compressive stress. For an additive under compressive residual stress, a crack will deflect away from the particle. This will add to the improvement of fracture toughness that crack deflection processes confer to the composite. However, if the secondary phase is placed under tension, a crack will deflect toward the particle. Not only will this increase the deflection experienced by the crack, but it will also raise the possibility of crack arrest in the secondary particle.

Selsing (1961) proposed Equation 5-5 for calculating the residual stresses in a secondary particle. In Equation 5-5, "$\Delta\alpha$" refers to the difference between the CTE of the matrix material and the secondary particle. If $\Delta\alpha$ is negative, then the secondary particle is under tension. "E" is the elastic modulus and "υ" is the Poisson's ratio. The subscripts "m" and "p" refer to the matrix and the particle respectively. "ΔT" is the difference between the temperature where relaxation of residual stresses occur and the processing temperature. Table 5-2 gives the data

used for calculating the residual stresses present in the B_6O-Y_2O_3-Al_2O_3 and B_6O-Y_2O_3-Al_2O_3-TiB_2 ceramics.

$$\sigma_{res} = \frac{\Delta\alpha(\Delta T)}{\frac{1+\upsilon_m}{2E_m} + \frac{1-2\upsilon_p}{E_p}}$$ **Equation 5-5**

Table 5-2: Data used for calculation of residual stress in the composites

	B_6O	TiB_2	Y_2O_3-Al_2O_3-B_2O_3
Thermal expansion coefficient (10^{-6} K^{-1})	5.46[7]	8.32[8]	7.0[9]
Poisson's ratio	0.197[10]	0.108‡	0.2
Elastic modulus (GPa)	540§	565‡	75[11]

For the B_6O-Y_2O_3-Al_2O_3 material, the Y_2O_3-Al_2O_3-B_2O_3 addition is expected to soften at about 800°C (Herrmann, unpublished). Differences in the thermal expansion coefficients between the B_6O matrix and the glass phase will set up residual stresses of 132MPa, which would be tensile in the glass phase. This

[7] Herrmann, unpublished
[8] Munro (2000)
[9] Estimation based upon the work of Rutz (1990)
[10] Shablala (2008)
[11] Assumption. The elastic moduli of many glasses lie between 50 and 100GPa

tensile stress would attract a growing crack towards the secondary particle. However, as this stress is only active over a small area around the secondary particle, the low amount of additive will not increase the amount of deflection that will occur in the ceramic significantly. As the grain boundaries between grains are mostly clean and well-formed (Kleebe *et al*. (2008)), the residual stresses will not reduced the grain boundary strength and hence not increase crack deflection to any great degree as is observed in Si_3N_4 ceramics with oxide additives.

For the B_6O-Y_2O_3-Al_2O_3-TiB_2 sample, the presence of the glass phase will reduce the onset temperature of residual stresses between the B_6O and the TiB_2 to the glass temperature. So for the B_6O-TiB_2 interaction, a residual stress of 881MPa, tensile in the TiB_2 grain, is established with a glass temperature of 800°C. Hence, in the B_6O-Y_2O_3-Al_2O_3-TiB_2 cracks will be more strongly attracted to the secondary particle than for the B_6O-Y_2O_3-Al_2O_3 materials. This supports the observation that there is significantly more deflection for the B_6O-Y_2O_3-Al_2O_3-TiB_2 composite than the B_6O-Y_2O_3-Al_2O_3 composite as well as the observation that the crack shears many of the TiB_2 grains.

If the glass phase was not present in the B_6O-TiB_2 ceramic, the onset of residual stresses would begin almost at the sintering temperature of the composite. Assuming that the relaxation temperature is about 1500°C (significantly lower than the 1850°C sintering temperature), the residual stresses in the theoretical B_6O-TiB_2 would be over 2GPa. This level of residual stress would cause

separation of the B_6O and the TiB_2 grains. This separation would be detrimental to the stability of the ceramic.

This effect has been observed in the B_6O-TiB_2 samples produced by Johnson (2010). These samples were produced by the in situ borothermic reduction of titania. These samples differed from the ones produced in the IKTS as these did not contain any liquid sintering aid, while the IKTS samples contained yttria-alumina additions. Two major differences between the sample behaviour were observed. Firstly, the B_6O-TiB_2 sample without an additive phase was more prone to grain pull-out during polishing. Secondly, indentation induced cracks deflected around the TiB_2 grains for the sample without an additive phase, but was found to generally shear the TiB_2 grains in the IKTS produced sample. So while the stresses induced by differences in CTEs can benefit crack deflection, excessive stress levels could be detrimental.

Regardless of the reason behind crack deflection, the fact remains that the boron suboxide composites do not undergo anywhere near the required amount of crack deflection to explain the increase in fracture toughness that has been measured.

5.5.3 Crack bridging

Crack deflection is often viewed as a synergistic process. Although crack deflection, by itself will increase the fracture toughness of the material, it can also give rise to other toughening processes. One such process is crack bridging.

If there are surviving ligaments (for example, grains) in the wake of the crack, then these ligaments can increase the toughness of the ceramic. As a crack advances through a material, the crack opening displacement increases with increasing distance from the crack tip. The presence of these ligaments will resist such opening. Eventually, the crack opening displacement at the ligament will exceed the critical strain for that ligament and it will fracture (Roesler (2007), Wachtman (2009)).

For the boron suboxide materials the presence of surviving ligaments are limited by the intragranular fracture, limited crack deflection and small grain size. For this reason, in boron suboxide, surviving ligaments are never observed. For the composites, which show an increased amount of crack deflection, crack bridges are observed, albeit very rarely. When examining the cracks from the indentation fracture toughness experiments, often an entire crack would occur without a single bridging event.

The crack bridging which is observed occurs with the secondary phases acting as a ligament. This is consistent with the boron suboxide matrix experiencing transgranular fracture. Due to the limited amount of these phases present in the composites, the amount of crack bridging which can occur is similarly limited. Figure 5-10 gives an indication of the crack bridging occurring in the B_6O-Y_2O_3-Al_2O_3 and B_6O-Y_2O_3-Al_2O_3-TiB_2 ceramics.

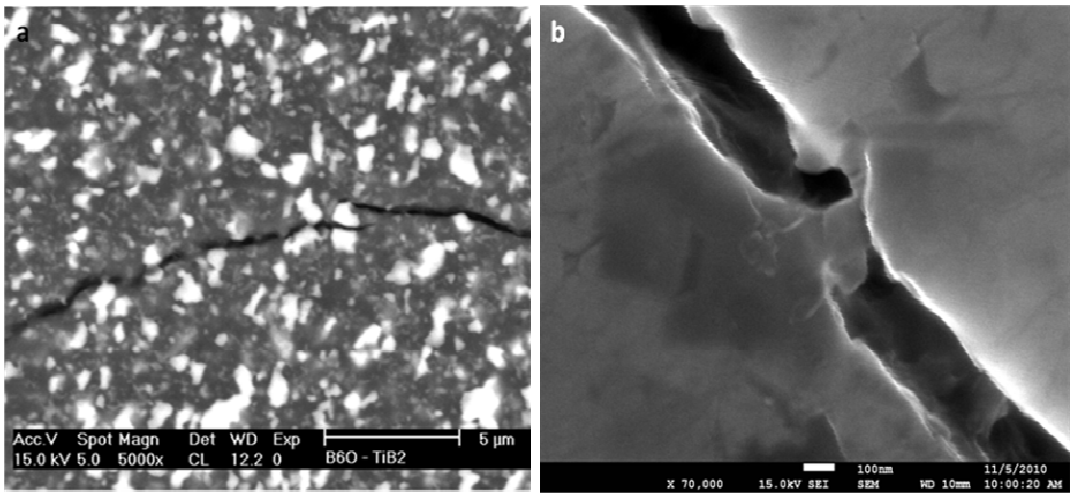


Figure 5-10: Crack bridging in (a) the B_6O-Y_2O_3-Al_2O_3-TiB_2 and (b) B_6O-Y_2O_3-Al_2O_3 composites

Although bridging events are often cited as the cause for the increase in fracture toughness in fibre and whisker reinforced ceramics, due to the extreme rarity of the event in boron suboxide materials, it is not possible that crack bridging plays a significant role in the toughening of the ceramic.

5.5.4 Frictional toughening

Usually associated with crack bridging is the dissipation of energy through friction. When a fiber or grain spanning the crack has broken in a intergranular fashion, it will still bridge the crack, but will no longer be attached to the one surface of the crack. As the crack opening increases, the dissociated grain will slide against its neighbouring grains. This friction between grains will dissipate some of the energy associated with crack opening.

As in crack bridging, this frictional toughening requires intergranular fracture and large grains. Hence, it is difficult for frictional toughening events in small-grained, transgranually-fractured boron suboxide. Frictional toughening is then only associated with the secondary phases present in the boron suboxide materials. Additionally, when a bridge does fracture, it does not always do so in a manner which would cause it to slide against the neighbouring grains. As can be seen in Figure 5-10, when the TiB_2 or Y_2O_3-Al_2O_3 bridges fracture, there would not be much friction against the neighbouring grains. Given that frictional bridging is a rare occurrence in the boron suboxide materials, and that not all the events which do occur will cause friction, frictional toughening will not play a significant role in toughening boron suboxide materials.

5.5.5 Transformation toughening

Transformation toughening is the reason behind the success of zirconia based and zirconia reinforced ceramics. Stabilised zirconia ceramics can have a fracture toughness of up to about 20MPam$^{0.5}$ (Evan, 1990). For transformation toughening to be a possibility, a material must possess a metastable phase of higher density than the stable crystal structure. When the stress field around the crack interacts with the metastable grain, the crystal structure will transform into the larger, stable crystal structure. It is this change in volume which will mechanically clamp the crack tip.

In boron suboxide materials, transformation toughening is not possible. From the work of McMillan *et al*. (1999), boron suboxide is stable and does not possess any crystal structure other than the $R\bar{3}m$ packing. Additionally, the secondary phases are either stable borides or stable borate glasses, which will also not transform. Hence, transformation toughening is not a toughening mechanism which can be expected in boron suboxide.

5.5.6 Crack arrest

It is possible for a crack to be arrested, either temporarily or permanently, in some aspect of the microstructure. This often leads to a shorter overall crack length than if the crack was running in the matrix material.

It has been noted that cracks in the B_6O-Y_2O_3-Al_2O_3-TiB_2 systems arrest within a TiB_2 grain. When a composite material is placed under load, the deformation in the material is inhomogeneous. This is due to differing elastic constants between the additive and the matrix materials. This can reduce the stress in the additive phase. A lower stress can be interpreted as a lower driving force for crack growth.

For the other composites and pure boron suboxide, the crack usually arrests within a pore, this is shown in Figure 5-11. The maximum stress perpendicular to the crack growth direction (σ_{yy}) at the tip of an elliptical crack can be given by Equation 5-6 (Wachtman *et al*. (2009)), where "σ" is the external applied stress, "c" is the crack length and "r" is the radius of curvature if the crack tip.

$$\sigma_{yy} = \sigma\left[1+2\left(\frac{c}{r}\right)^{0.5}\right] \qquad \textbf{Equation 5-6}$$

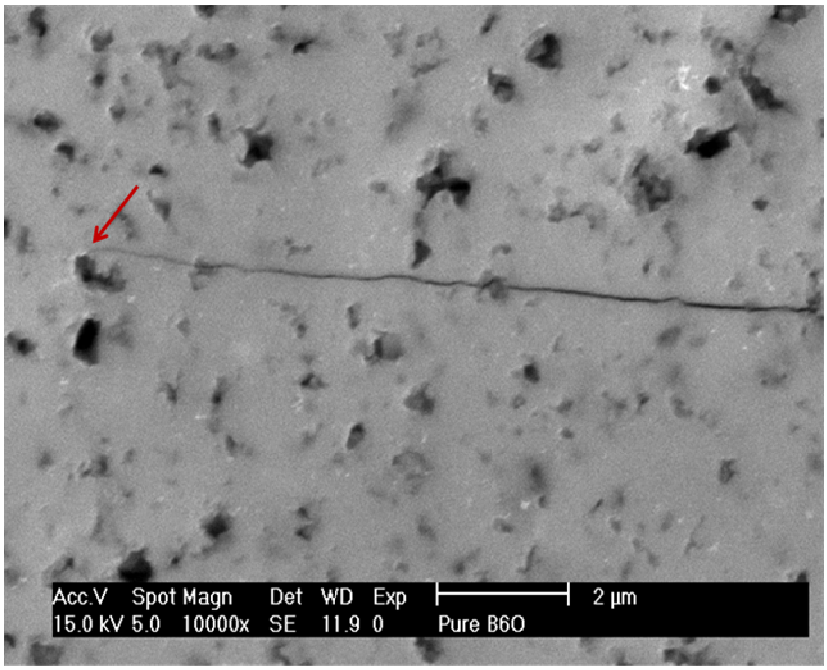


Figure 5-11: Crack arrest by a pore in pure boron suboxide

If the crack tip is small, as in the case for brittle ceramics, then there is a large stress intensity factor, allowing for easy fracture. However, in a pore, the radius of the crack tip becomes the radius of the pore. This drastically reduces the concentration of stress, which is enough to arrest a crack if the applied stress is reduced as in the case of the IFT method.

5.5.7 Surface Energy

As shown in Section 4.8, the pure boron suboxide materials undergo transgranular fracture. In Section 5.5.2 it was discussed that the lack of intergranular fracture would limit the toughness of the pure boron suboxide material, as crack deflection

is limited. Despite the lack of crack deflection, it is still possible for the grain structure to play a role in toughening the ceramic.

Single crystals have a continuous slip plane where the energy for fracture is reduced. Although the slip plane still exists in polycrystalline materials, it plays a far less significant role than in the single crystal. Any grain within a polycrystalline material is orientated with different tilt and twist angles to its surrounding grains. This interrupts the continuity of the slip plane and randomises its orientation to any approaching crack. Without the slip plane for easy fracture, polycrystalline materials should be tougher than its single crystal.

However, for boron suboxide, the fracture toughness of the polycrystalline material is far lower than that of the single crystal. He *et al*. (2002) used the indentation fracture toughness method to determine the fracture toughness of single crystal boron suboxide to be 4.5MPa.m$^{0.5}$. From Section 4.7, the fracture toughness of polycrystalline boron suboxide, as determined by the SEVNB method, is 1.3±0.2MPa.m$^{0.5}$.

One possible reason for the discrepancy in fracture toughness between single crystal and polycrystalline boron suboxide is the presence of twin planes. Twin planes exist in a higher energy state than the rest of the grain, this reduces the energy with a crack must expend when grown along the twin plane. For a material

experiencing transgranular fracture, if the twin plane is of significantly high energy, then an advancing crack will tend to deflect along the twin plane, rather than continue through the material. This is illustrated in Figure 5-12.

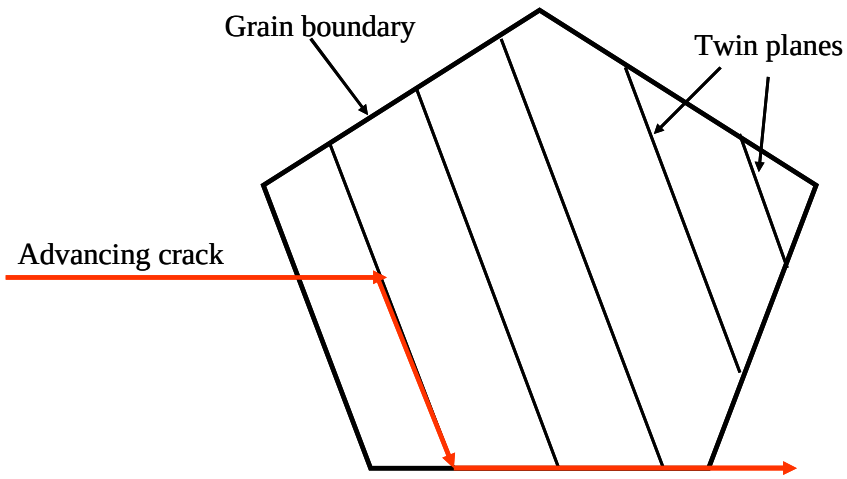


Figure 5-12: Illustration of a transgranular crack deflecting along a twin plane

Boron based materials have a marked tendency to extensive twinning. The presence of twins in the polycrystalline boron suboxide has been validated previously by the work of Shabalala *et al*. (2007) and Kleebe *et al*. (2008). To be a true single crystal, the crystals examined by He *et al*. (2002) would need to have been twin-free as twins are essentially low angle grain boundaries. Whether or not twins are present in the single crystal remains uncertain, as He *et al*. never presented TEM images of their crystals. However, the effort of He *et al*. is similar to the work of Hubert *et al* (1998) and Gladkaya *et al* (2001) who both produced near-stoichiometric boron suboxide in a B_2O_3 rich melt under high pressure. Although the crystals they produced were smaller than that of He *et al*, the

crystals were extensively twinned. The lack of detailed information about the single crystal of He *et al*. makes any comparison of the effects of twinning difficult.

However, for polycrystalline boron suboxide, the direction of the twin planes will be randomised by the grain structure. If a transgranular crack does have a tendency to traverse along the twin planes, then an effect similar to crack deflection should arise. This will increase the fracture toughness of the polycrystalline boron suboxide material. This has not been observed.

A major difference between the polycrystal and single crystal boron suboxide is the oxygen stoichiometry. As mentioned in Section 5.2, the oxygen stoichiometry of the polycrystalline boron suboxide examined is not fully known. However, the stoichiometry of previously hot-pressed B_6O has never exceeded $B_6O_{0.9}$. Often, the reported stoichiometry is far lower, about $B_6O_{0.72}$ to $B_6O_{0.839}$ (Hubert *et al*. (1998)). Comparatively, the stoichiometry of the single crystal is $B_6O_{0.98}$.

This additional oxygen will increase the volume and change the energy of the rhombohedral unit cell. This is often seen in the inclusion of interstitials into a metallic system. As the oxygen atoms serves to strengthen the inter-icosahedra bonds between the various icosahedra that make up the B_6O unit cell by donating electrons to the icosahedra (Lowther (2002)), it is conceivable that a higher

oxygen stoichiometry will produce a better bonded unit cell, which will increase the energy to fracture it. Additionally, from the work of Hubert *et al*. (1998), the higher the oxygen stoichiometry of boron suboxide, the better the crystal structure of boron suboxide conforms to the requirements of Mackay packing. The less distorted this macro-crystal is, the lower its energy. This is converted to a higher energy to fracture the crystal.

However, a change in crystallinity and oxygen content cannot be the only reasons behind the increase in fracture toughness. The polycrystalline pure boron suboxide materials produced by Itoh *et al*. (2000) were found to possess a very low fracture toughness (<1 $MPa.m^{0..5}$) despite a reported high crystallinity and oxygen stoichiometry. Additionally, the conditions proposed for Mackay packing are not seen in the boron suboxide materials with additive phases. This can be observed when assigning the lattice parameters (using a hexagonal unit cell) to the XRD traces for the various boron suboxide materials.

In Figure 5-13, the height of the hexagonal cell (c) is plotted against the length of one of the basal sides (a) for the boron suboxide materials examined and various materials from literature. To clarify the central region of the graph, it was redrawn to exclude the alpha boron and boron carbide materials (Figure 5-14). The B_6O-Y_2O_3-Al_2O_3-TiB_2 composite is excluded from these graphs due to the limited number of B_6O peaks detected during x-ray diffraction.

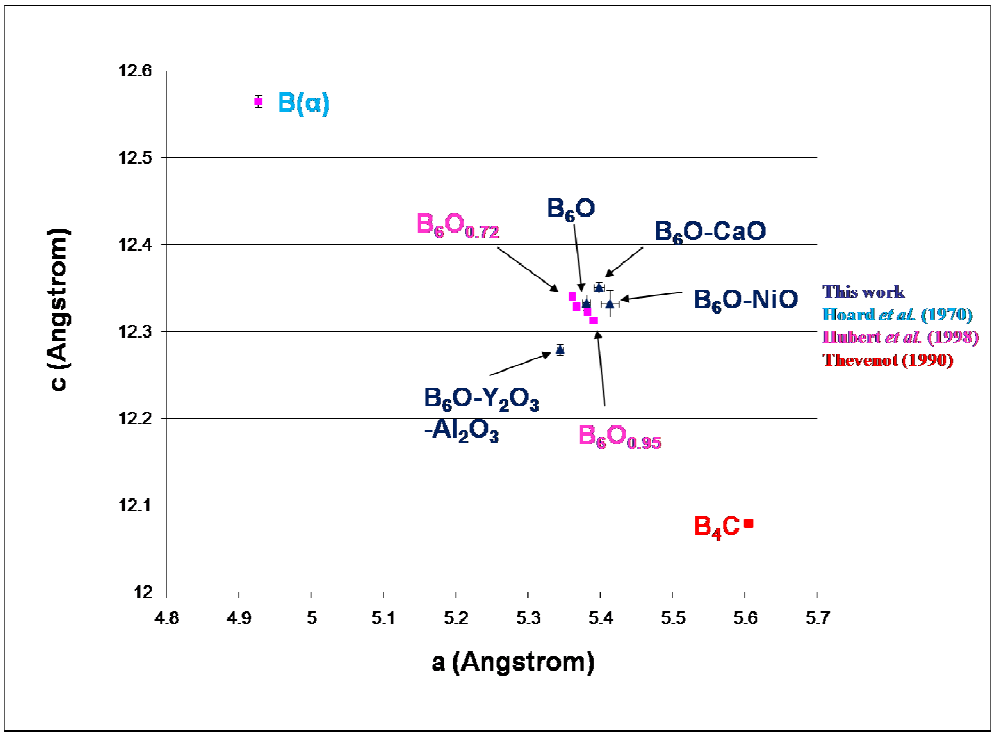


Figure 5-13: Lattice parameter plot of the various boron suboxide materials, boron and boron carbide

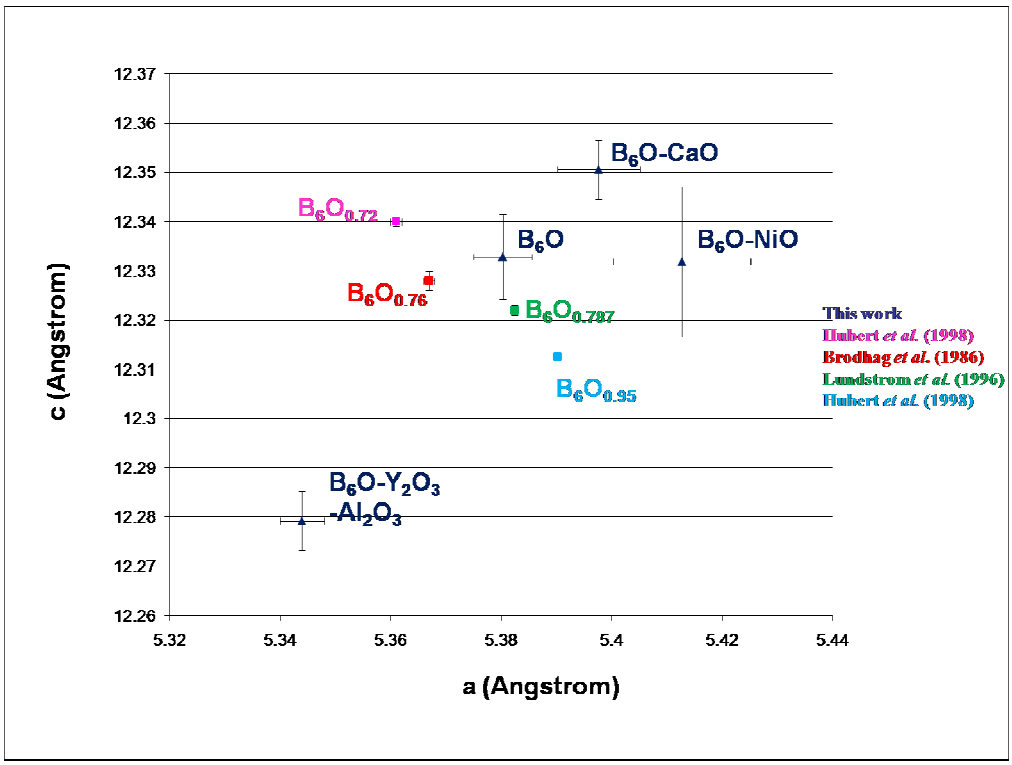


Figure 5-14: Figure 5-12 redrawn, excluding boron and boron carbide

As can be observed from Figures 5-13 and 5-14, the pure B_6O sample produced at the IKTS lies in the B_6O region of the plot. Additionally, from its position, it is obvious that the material is substoichiometric. However, the exact oxygen content is unknown.

As is to be expected, the lattice parameters of the composites are much closer to that of boron suboxide rather than that of pure boron or boron carbide. However, in Figure 5-14, it is evident that the composites are not very closely linked to the B_6O cluster. Additionally, there is not any systematic progression in the a-c ratio which is what would be expected if the additive phases directly affected the oxygen stoichiometry of the B_6O matrix.

Additionally, the additives change the c/a ratio by any significant degree (Figure 5-15). It was proposed by Hubert *et al*. (1998) that with higher stoichiometry, the c/a ratio changes and that, as the ratio approaches 2.26, Mackay packing becomes possible. No such trend is observed for the additives. It is thus unlikely that the presence or absence of Mackay packing is affected by the additive phases.

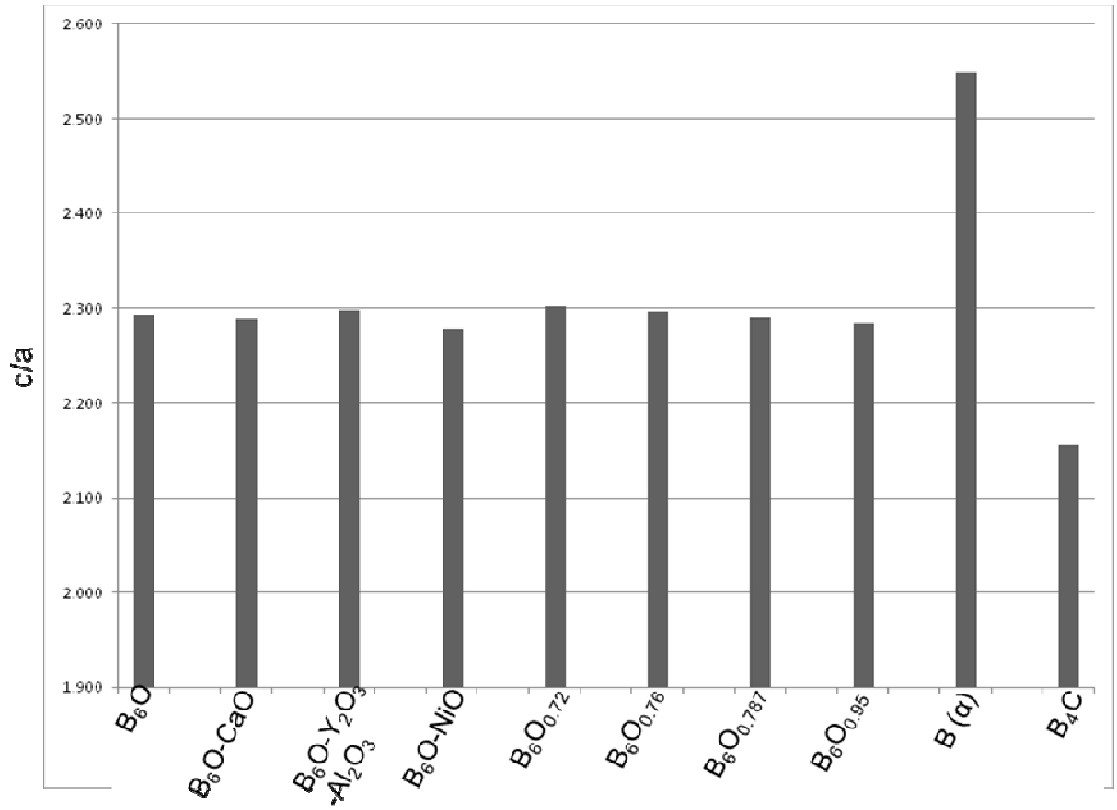


Figure 5-15: c to a ratio for the boron based materials.

Although the additives have been shown to affect the lattice parameters of the host B_6O, there does not seem to be any logical connection between the additives and how they change the lattice constants. An additional, more detailed study into the affect of additives on the lattice parameters of B_6O is necessary. When considering the increase in fracture toughness observed in the B_6O materials with additives, as opposed to the pure boron suboxide and the limited physical toughening mechanisms present, the additives must change the defect structure of the B_6O phase. A change in the defect structure would change the surface energy of the material and hence change its fracture toughness. The exact manner in

which the additives change the fracture toughness of the materials will need to be subject to a more detailed analysis.

6.0 Conclusions and Recommendations

This body of work was primarily directed at determining the reasons behind the previously observed increase in fracture toughness of boron suboxide materials with sintering aids as compared to pure boron suboxide. To this end, the fracture toughness of Spark Plasma Sintered pure boron suboxide and various boron suboxide materials with sintering aids were determined using the SEVNB, IFT and the recently developed COD technique.

Additionally, the indentation size effect of boron suboxide was examined. It was found that pure boron suboxide has a significant indentation size effect. This makes any comparison of hardness measurements, taken under different loads, prone to error.

Compared to the SEVNB method, the IFT method was found to significantly over-estimate the fracture toughness of the composites. The reasons for this were related to deficiencies in the method itself and the microstructure of the composite, especially porosity. The deviation for the COD method was found to depend upon the microstructure. If crack arrest occurred in a pore, the fracture toughness of the ceramic was significantly over-estimated. When the crack tip was visible, the method was found to be accurate.

The toughness of the composites determined by the SEVNB validated the large increase in fracture toughness previously observed. The crack propagation through the materials was examined in order to explain this phenomenon. The failure of the boron suboxide materials was found to be intragranular, regardless of which additive was present in the composite. This, coupled with a limited degree of crack deflection and isolated incidents of crack bridging, branching and frictional events is not sufficient to explain the observed increase in fracture toughness.

It was found that the additions of secondary phases into the boron suboxide materials change the lattice parameters of the boron suboxide crystals. However, no correlation between the additive present and the change in lattice parameters was established.

A more detailed investigation into the effect of secondary phases upon the fracture toughness of boron suboxide is recommended, focusing on the change of lattice parameters induced by the introduction of secondary phases. This would aid in understanding the role of the sintering aids in the toughness of boron suboxide materials. In turn, this may produce a mechanically superior class of boron suboxide materials.

References

Andrews, A. *Development of boron suboxide composites with improved toughness*. PHD thesis, University of the Witwatersrand (2008)

Andrews, A., Herrmann, M., Shabalala, T.C., and Sigalas, I. *Liquid phase assisted hot pressing of boron suboxide-materials* Journal of the European Ceramic Society **28** (2008) PP1613-1621

Anstis, G.R. Chantikul, P. Law., B.R. and Marsahll, D.B. *A critical evaluation of indentation techniques for measuring fracture toughness: I, Direct crack measurements* Journal of the American Ceramic Society **64** No. 9 (1981) PP533-538

Atkinson, C. and Craver, R. V. *Theoretical aspects of fracture mechanics* Progress in Aerospace Science **31** (1995) PP1-83

Bolmgren, H. and Lundström, T. *Structure refinement of the boron suboxide B_6O by the Rietveld method*. AIP conference proceedings **231** (1991) PP197-200

Brodhag, C. and Thevenhot, F: *Hot pressing of various boron phases*. Journal of the Less-Common Metals, **117** (1986) PP175-180

Brookes C.A. *Mechanical properties of cubic boron nitride- a perspective.* Institute of Physics, Conference Series **75** (1986) PP207-220

Cao, M., Jiang, J., Liu, H. and Yuan, J. *A simple method to prepare boron suboxide fibres* Journal of Electroceramics (2006) PP817-820

Chakraborty, I.N., Rutz, H.Z. and Day, D.E. *Glass formation, properties and structure of Y_2O_3-Al_2O_3-B_2O_3 glasses* Journal of Non-Crystalline Solids **84** (1986) PP86-92

Chen, C., He, D., Kou, Z., Peng, F., Yao, L., Yu, R. and Bi, Y. *B_6O-Based Composite to Rival Polycrystalline Cubic Boron Nitride* Advanced Materials **19** (2007) PP4288–4291

Choudhury, I.A. Azuddin, M. Tee, C.H. *Evaluation of fracture toughness of ceramic inserts by indentation techniques.* Proceedings of the 1st International Conference & 7th AUN/SEED-Net Fieldwise Seminar on Manufacturing and Material Processing (2006) PP175-180

Clarke, D.R. *On the equilibrium thickness of intergranular glass phases in ceramic materials* Journal of the American Ceramic Society **70** [1] (1987) PP15-22

Dieter, G.E. *Mechanical metallurgy 2^{nd} edition.* McGraw-Hill. New York. 1976

Evans, A.G. *Perspective on development of high-toughness ceramics* Journal of American Ceramic Society **72** [2] (1990) PP187-206

Evans, A.G. *High Toughness Ceramics*. Materials Science and Engineering, A105/106 (1988) PP65-75

Evans A.G. and Charles EA. *Fracture toughness determinations by indentation*. Journal of the American Ceramic Society 59 (1976) PP371–372

Ellison-Hayashi, C., Zandi, M., Shetty, D., Kuo, P., Yeckley, R. and Csillag, F. *Boron suboxide material and method for its preparation.* U.S Patent 5,330,937 (1994)

Faber K.T. and Evans, A.G. *Crack deflection processes –II. Experiment*. Acta Metallurgica V31 [4] (1983) PP577-587

Fischer, H. and Marx, R. *Fracture toughness of dental ceramics: comparison of indentation and bending method"* Dental Materials **18** (2002) PP12-19

Fischer, H., Waindich, A. and Telle, R. *Influence of preparation of ceramic SEVNB specimens on fracture toughness testing results* Dental Materials **28** (2008) PP618-622

Freemantle, C.S. *The wear studies of boron suboxide based cutting tool materials in machining applications.* MSc dissertation University of the Witwatersrand. (2009)

Gao, F., Hou, L., and He, Y. *Origins of superhardness in icosahedral B_{12} materials.* Journal of Physical Chemistry B **108** (2004) PP13069-13073

Gladkaya, I.S., Dyuzheva, T.I., Ekimov, E.A., Nikolaev, N.A. and Bendeliani, N.A. *Crystal growth at high pressure and the problem of characterization of the interstitial phases in the B-C-O system.* Journal of Alloys and Compounds. **329** (2001) PP153-156

Gong, J., Wu, J. and Guan, Z. *Examination of the indentation size effect in low-load Vickers hardness testing of ceramics.* Journal of the European Ceramic Society **19** (1999) PP2625-2631

Goosey, B.F. and Anderson, S.C. *Method of fabricating boron suboxide articles* US Patent 3,816,586 (1974)

Halitim, F. Ikhlef, N. Boudoukha, L. Fantozzi, G. *Young's modulus and fracture toughness of alumina implanted with Zr^+, Cr^+, Ti^+ and Ni^+. The effect of residual stresses.* Journal of Physics D. Applied Physics **30** (1997) PP330-337

He, D., Daemen, D., Qian, J., Shen, T.D., Zerda, T.W. and Zhao, T *Boron suboxide: As hard as cubic boron nitride* Applied Physics Letters. **81** [4] (2002) PP 643-645

He, D., Shieh, S. and Duffy, T. *Strength and Equation of state of boron suboxide from radial x-ray diffraction in a diamond cell under nonhydrostatic compression.* Physical Review B. (2004) **70** PP1-9

Herrmann, M., Raethel, J., Bales, A., Semp, K., Sigalas, I. and Hoehn, M. *Liquid phase densification of superhard B_6O materials* Journal of the European Ceramic Society **29** (2009) PP2611-2617

Hoard, J. L.; Sullenger, D. B.; Kennard, C. H. L. and Hughes, R. E.. *The structure analysis of β-rhombohedral boron.* J. Solid State Chem. **1** 2 (1990):PP268–277.

Holcombe C. E., Ottis J.H. and Horne, O. *Method for preparing boron suboxide*. US Patent 3,660,031. 1972

Hubert, H., Garvie, L.A.J., Devouard, B., Buseck, P.R., Petusky, W.T. and McMillan, P.F: *High-Pressure, High-Temperature Synthesis and Characterization of Boron Suboxide (B_6O)* Chem. Mater. **10** (1998) PP1530-1537

Hungría, T., Galy, J. and Castro, A. *Spark plasma sintering as a useful technique to the nanostructuration of piezo-ferroelectric materials* Advanced Engineering Materials **11** 8 (2009) PP615-631

Itoh, H. *Preparation of superhard ceramic materials and evaluation of their mechanical properties.* Journal of the Ceramic Society of Japan. **112** [3] (2004) PP121-129

Itoh, H., Maekawa, I. and Iwahara, H. *Microstructure and mechanical properties of B_6O-B_4C sintered composites prepared under high pressure* Journal of Materials Science **35** (2000) PP693-698

Jiang, J., Cao, M., Sun, Y., Wu, P. and Yuan, J. *Star-shaped cyclic-twinning nanowires* Applied Physics Letters **88** (2006) PP163107-1 – 163107-3

Jones, S.L. Norman, C.J and Shahani, R. *Crack-profile shapes formed under a Vickers indent pyramid* Material Science Letters 6 (1987) PP721-723

Johnson, O.T. *Improvement on the mechanical properties of boron suboxide (B_6O) based composites using other compounds as second phase*. MSc dissertation. University of the Witwatersrand (2008)

Kawai, J., Maeda, K., Higashi, I., Takami, M., and Hayashi, Y. *Site determination of oxygen in B_6O by oxygen Kα x-ray-emission spectroscopy.* Physical Review B **42.** [9] (1990) PP5693-5701

Kayhan, I.O. and Inal, O.T. *Synthesis of aluminium infiltrated boron suboxide drag cutters and drill bits.* Journal of Materials Science. **34** (1999) PP4105-4120

Kharlamov, A. I., Kirillova, N. V., Loichenko, S. V. and Kostyuk, B. D. *Properties of boron suboxide $B_{13}O_2$.* Powder Metallurgy and Metal Ceramics **41** [1-2], (2002) PP97-106

King, R.B. *The icosahedrons in inorganic chemistry.* Inorganica Chemica Acta. **198** (1992) PP841-861

Kleebe, H-J., Lauterbach, S., Shabalala, T., Herrmann, M. and Sigalas, I. *B_6O: a correlation between mechanical properties and microstructure evolution upon Al_2O_3 addition during hot pressing.* Journal of the American Ceramic Society. **91** [2] (2008) PP569-575

Kübler, J.J. *Fracture toughness of ceramics using the SEVNB method: From a preliminary study to a standard test method*. From: "Fracture resistance testing of monolithic and composite brittle materials", ASTM STP 1409, Salem, J.A., Quinn, G.D., Jenkins, M. G., eds. American Society for Testing and Materials, West Conshohoken, PA, 2002.

Lawn, B.R. and Wilshaw, T.R. *Quasi-static solid particle damage in brittle solids – I. Observations, analysis and implications*. Acta Metallurgica **V24** (1976) PP936-956

Lee, S., Kim, S.W., Bylander, D.M. and Kleinman, L. *Crystal structure, formation enthalpy and energy bands of B_6O.* Physical Review B **44** 8 (1991) PP3550-3354

Letsalo, T. and Lowther, J.E. *Systematic trends in boron icosahedral structured materials* Physica B (2008) PP. 2760-2767

Liu, X., Zhoa, X., Hou, W. and Su, W. *A new route for the synthesis of boron suboxide B_7O.* Journal of Alloys and Compounds. **223** (1995) L7-L9

Loladze T.N. *Of the theory of diffusional wear* CIRP annals – Manufacturing technology **30** 1 (1981) PP71-76

Lowther, J.E. *Possible ultra-hard materials based upon boron icosahedra.* Physica B **22** (2002) PP173-178

Lundström, T. *Structure and bulk modulus of high-strength boron compounds.* Journal of Solid State Chemistry. **133** (1997) PP82-92

Lundstrom, T. and Andreev, Y.G. *Superhard boron-rich borides and studies of the B–C–N system.* Material. Science. Engineering. A **209** (1996) PP16–22

Makarov, V.S. and Ugai. Y.A. *Thermochemical study of boron suboxide B_6O.* Journal of the Less Common Metals. **117** (1986) PP277-281

Malzbender, J. *Comments on hardness definitions* Journal of the European Ceramic Society **23**, 9 (2003) PP1355-1359

Manupriya, Thind, K.S., Sharma, G., Rajendran, V., Singh, K., Gayathri Devi, A.V., Aravindan, S. *Structural and acoustic investigations of calcium borate glasses.* Phys. Stat. Sol. (a) **203** 10 (2006), PP. 2356-2364

Marshall, D.B. and Lawn, B.R. *Indentation of brittle materials* in "Microindentation techniques in material science and engineering". ASTM STP 889. [ed.] Blau, P.J. and Lawn, B.R. American Society for Testing and Materials, Philadelphia (1986) PP26-46

McMillan, P.F., Hubert, H., Chizmeshya, A., Petuskey, W., Garvie, L. and Devouard, B. *Nucleation and growth of icosahedral boron suboxide clusters at high pressure.* Journal of Solid State Chemistry. **147** (1999) PP281-290

Meacham, B.E. Marshall, M.C. and Branagan, D.J. *Palmqvist fracture toughness of a new wear-resistant weld Alloy* Metallurgical and Materials Transcripts. A **37A** (2006) PP1316-1327

Munz, D. and Fett, T. Ceramics: Mechanical properties, failure behaviour, material selection. Springer, New York (1999)

Niihara, K. Morena, R. and Hasselman, D.P.H. *Evaluation of K_{Ic} of brittle solids by the indentation method with low crack-to-indentation ratios.* Material Science Letters **1** (1982) PP13-16

Oglivy, I.M. Perrot, C.M. Suiter, J.W. *On the indentation fracture of cemented carbides Part 1 – Survey of operative fracture modes* Wear **43** (1977) PP239-252

Ogunmuyiwa, E.N. *Study of sintering and structure-property relationships in boron suboxide (B_6O) – alkaline earth metal oxide, cobalt and nickel compound*. MSc dissertation. University of the Witwatersrand. (2008)

Olofsson, M. and Lundstrom, T. *Synthesis and structure of non-stoichiometric B_6O.* Journal of Alloys and Compounds. **257** (1997) PP91-95

Palmqvist, S. *Occurrence of crack formation during Vickers indentation as a measure of the toughness of hard metals,* Archiv Eisenhüttenwesen, 33 (1962) PP. 629-634 (in German)

Quinn, G.D. "**The fracture toughness Round Robin in Vamas: What we have learnt**," *Fracture resistance testing of monolithic and composite brittle materials, ASTM STP 1409*, J.A. Salem, G.D. Quinn and M.G. Jenkins, Eds., American Society for Testing and Materials, West Conshohocken, PA (2002)

Richerson, D.W., *Modern Ceramic Engineering: Properties, processing and use in design* Taylor and Francis, New York. 2006

Rösler, J., Harders, H. and Bäker, M. *Mechanical behaviour of engineering materials*: *Metals, Ceramics, Polymers and Composites*. Springer, Berlin. 2007

Rutz, H.L., Day, D.E. and Spencer, C.F. jr, *Properties of yttria-aluminoborate glasses*. Journal of the American Ceramic Society **73** [6] 1990 PP1788-1790

Sasai, R., Itoh, H., Fukatsu, H. and Kojima, H. *High pressure consolidation of B_6O-diamond mixtures*. Journal of Material Science **36** (2001) PP5339-5343

Selsing, J. *Internal stresses in ceramics*. Journal of the American Ceramic Society **44**, 8, (1961) P 191

Shabalala, T.C. *The preparation and characterization of boron suboxide (B_6O) based composites***.** PhD thesis. University of the Witwatersrand (2007)

Shabalala, T.C., McLachlan, D.S., Sigalas, I. and Herrmann, M. *Hard and tough boron suboxide based composites* Ceramics International. **34** (2008) PP1713-1718

Shelby, J.E. *Introduction to glass science and technology* 2nd edition. RSC, Cambridge 2009.

Shetty, D.K. Wright, I.G. Mincer, P.N. Clauer, A.H. *Indentation fracture of WC-Co cermets.* Material Science **20** (1985) PP1873-1882

Shrivastava, S. *Indentation size effect in WC-Co*. PhD thesis, University of the Witwatersrand. (2007)

Smolin, M.D., Grebenkina, V.G., Yu, M., Shvartsman, E.I. and Panov, L.I. *Elastodynamic characteristics of boride phases of nickel.* Poroshkovaya Metallurgiya **5** 237 (1984) PP. 86-90

Steinbrech, R.W. *Toughening mechanisms for ceramic materials* Journal of European Ceramic Society **10** (1992) PP131-142

Stevenson, M.E.; Kaji, M., and Bradt, R.C. *Microhardness anisotropy and the indentation size effect on the basal plane of single crystal haematite*. Journal of European Ceramic Society **22** (2002) PP1137-1148

Sung, C-M. and Sung, M. *Carbon nitride and other speculative superhard materials.* Material Chemistry and Physics **43** (1996) PP1-18

Thevenot, F. *Boron carbide – a comprehensive review.* Journal of the European Ceramic Society. **6** (1990) 205-225

Verprek, S. *The search for novel, superhard materials*. Journal of Vacuum Science and Technology A **17** (1999) PP2401-2420

Werheit, H. and Kuhlmunn, U. *FTIR and FT Raman spectra of B_6O.* Journal of Solid State Chemistry. **133** (1997) PP260-263

Wachtman, J.B., Cannon, W.R. and Matthewson, M.J. *Mechanical properties of ceramics (2^{nd} ed.)*. John Wiley, New York (2009)

Wiederhorn, S.M. *Brittle fracture and toughening mechanisms in ceramics.* Annual Review of Material Sciences **14** (1984) PP373-404

Yu, S., Wang, G., Yin, S., Zhang, Y. and Liu, Z. *Nanostructured films of boron suboxide by pulsed laser deposition.* Physics Letters A. **268** (2000) PP442-447

Yu, Z., Jiang, J., Yuan, J. and Zhu, J. *Twin-plane re-entrant edge growth of rhombahedra boron suboxide platelets* Journal of Crystal Growth **312** (2010) PP1789-1792

Yurkov, A.L.; Sarkisyan, T.A.; Ivanov, D.A. and Bradt, R.C. *Final stages of sintering ceramic materials: Effect of residual porosity and microstructure on mechanical characteristics of surface.* Ceramics International **23** (1997) PP389-399

Zlatkin , AT. and Lube, E.L *Estimation of fracture toughness and residual stress in brittle crystals from indentation-induced acoustic emission* Journal of Crystal Growth 118 (1992) PP218-230

Appendix A

A-1: Calculation of B_2O_3 glass densities

Due to a lack of published data, the exact density of the yttra-alumina borate glass present in the B_6O – 1.54vol% Y_2O_3 – 1.45vol% Al_2O_3 composite is unknown. Additionally, the exact composition of the glass is also not certain. However, as stated in Section 3.7, the final sintered composite was assumed to have 1.5wt% B_2O_3 present.

Based upon the work of Rutz *et al*. (1990), it can be shown that there is only a small difference between calculating the density of the composite using the density of the glass and approximating the density using the density of the oxides. The data collected by Rutz *et al*. on the densities of various glasses are presented in Table A2.

In calculating the density of the glass phase, using the density of the oxides, the densities and molecular weights of the oxides are presented in Table A2. The densities of the alumina and yttria additions are that of the crystalline solids. The density of the B_2O_3 addition is of its amorphous phase.

Table A1: Density and molecular weight of the oxides

	Oxide density (g/cm^3)	Molecular weight (g/mol)
B_2O_3	1.84	69.66
Al_2O_3	3.99	101.96
Y_2O_3	5.03	225.82

The density of the glass was calculated using Equation A1, where ρ_g is the density of the glass, x_i is the mass fraction of phase "i" and ρ_i is the density of phase "i".

$$\frac{1}{\rho_g} = \sum \frac{x_i}{\rho_i} \qquad \textbf{Equation A11}$$

In Table A2, the densities measured by Rutz and the densities calculated through Equation A1 are compared.

Table A2: Comparative of the calculated and measured densities of yttria-alumina-borate glasses

Glass number	Composition (mol%)			Measured density (g/cm^3)	Calculated density (g/cm^3)	Difference (%)
	B_2O_3	Al_2O_3	Y_2O_3			
1	65	20	15	3.06	2.73	10.76
2	65	25	10	2.86	2.63	8.02
3	60	25	15	3.08	2.82	8.35
4	55	20	25	3.70	3.10	16.24
5	55	25	20	3.30	3.01	8.76
6	55	30	15	3.12	2.92	6.48
7	55	35	10	2.95	2.82	4.43
8	50	25	25	3.55	3.20	9.98
9	50	35	15	3.16	3.02	4.55

The glass in the B_6O – 1.54vol% Y_2O_3 – 1.45vol% Al_2O_3 composite would have a molar composition of 23.3mol % Y_2O_3 – 38.6mol% Al_2O_3 – 38.1mol% B_2O_3. Since none of the glasses in Table A3 have a composition near the expected composition, a direct adaptation of the work of Rutz is not possible. However, as can be seen in Table A2, the difference between measured and calculated densities is always less than 17%, and usually less than 10%. As the differences between the measured and calculated densities are quite small, it is a reasonable

approximation to use the calculated densities when dealing with the Y_2O_3-Al_2O_3-B_2O_3 glasses within the B_6O composites.

A-2: Calculation of B_2O_3 content of Y_2O_3-Al_2O_3-B_2O_3 glasses

Based upon the work of Chakraborty *et al*. (1986) the B_2O_3 content of the Y_2O_3-Al_2O_3-B_2O_3 glasses found in the B_6O-Y_2O_3-Al_2O_3 and B_6O-Y_2O_3-Al_2O_3-TiB_2 can be estimated.

Assuming that, during sintering, there is no volatisation of either the Y_2O_3 or Al_2O_3 additions; and that there is not segregation of the two oxides, the Y_2O_3:Al_2O_3 ratio in the final composites is 0.6. This is for both the B_6O-Y_2O_3-Al_2O_3 and B_6O-Y_2O_3-Al_2O_3-TiB_2 composites.

This ratio of 0.6 can be plotted on the phase diagram developed by Chakraborty *et al*.. The points of intercepts of this line and the stable glass region give the upper and lower compositions for a stable Y_2O_3-Al_2O_3-B_2O_3 glass. On the phase diagram by Chakraborty *et al*. (Figure A-1), the stable glass region is denoted as "clear glass". From the phase diagram, the upper limit for glass stability is 19mol%Y_2O_3-32%Al_2O_3-51%B_2O_3, while the lower limit is 13mol%Y_2O_3-22%Al_2O_3-65%B_2O_3.

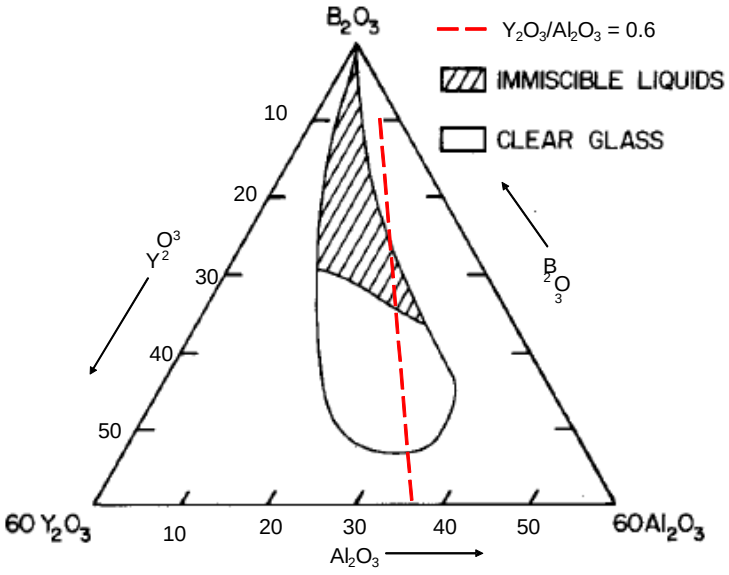


Figure A-1: Y_2O_3-Al_2O_3-B_2O_3 phase diagram from Chakraborty *et al*. (1986)

The region of stability can be extended under certain circumstances. Firstly, magnesium is a known contaminant in the amorphous boron used to produce B_6O. The presence of MgO will stabilise any glass present, allowing for lower B_2O_3 content. Secondly, thin films of glass, such as those in small triple junctions, do not always crystallise (Clarke (1987).

Appendix B

B-1: Hardness measurements

In this appendix, all of the hardness measurements conducted on the various samples is presented.

B-1.1: Indentation size effect

Hardness measurements were performed on three hot-pressed pure boron suboxide samples. The three hot pressed samples are labeled "Pure B_6O (hot-P) 1", "Pure B_6O (hot-P) 2" and "Pure B_6O (hot-P) 1". The recorded hardness (Hv) and average diagonal lengths (d_{ave}) are tabulated in Tables B1 to B6. All of the data are for a load applied for ten seconds.

Table B1: Hardness vales and diagonal lengths for hot-pressed pure boron suboxide under a 100g load

	Pure B_6O (hot-P) 1		Pure B_6O (hot-P) 2		Pure B_6O (hot-P) 3	
	d_{ave} (μm)	$Hv_{0.1kg}$ (GPa)	d_{ave} (μm)	$Hv_{0.1kg}$ (GPa)	d_{ave} (μm)	$Hv_{0.1kg}$ (GPa)
Individual measurements	6.89	38.38	6.39	44.55	6.62	41.57
	6.38	44.69	7.44	32.86	6.96	37.55
	6.67	40.95	7.00	37.13	6.57	42.14
	7.24	34.75	6.34	45.26	6.85	38.77
	6.75	39.93	6.12	48.65	6.83	39.05
Average	6.8 ± 0.3	39.7 ± 3.6	6.7 ± 0.5	41.7 ± 6.5	6.8 ± 0.2	39.8 ± 2.0
Combined diagonal length (μm)	6.7 ± 0.3					
Combined hardness (GPa)	40.1 ± 4.2					

Table B2: Hardness vales and diagonal lengths for hot-pressed pure boron suboxide under a 200g load

	Pure B_6O (hot-P) 1		Pure B_6O (hot-P) 2		Pure B_6O (hot-P) 3	
	d_{ave} (μm)	$Hv_{0.2kg}$ (GPa)	d_{ave} (μm)	$Hv_{0.2kg}$ (GPa)	d_{ave} (μm)	$Hv_{0.2kg}$ (GPa)
Individual measurements	9.71	38.59	9.85	37.50	9.75	38.31
	9.47	40.61	10.57	32.60	9.76	38.19
	10.01	36.31	10.61	32.35	10.22	34.83
	10.54	32.78	10.39	33.70	9.84	37.61
	10.48	33.16	10.39	33.74	9.39	41.26
Average	10.0 ± 0.5	36.7 ± 3.5	10.1 ± 0.5	35.7 ± 3.7	10.1 ± 0.3	35.9 ± 2.3
Combined diagonal length (μm)	10.1 ± 0.4					
Combined hardness (GPa)	36.1 ± 3.0					

Table B3: Hardness vales and diagonal lengths for hot-pressed pure boron suboxide under a 300g load

	Pure B_6O (hot-P) 1		Pure B_6O (hot-P) 2		Pure B_6O (hot-P) 3	
	d_{ave} (μm)	$Hv_{0.3kg}$ (GPa)	d_{ave} (μm)	$Hv_{0.3kg}$ (GPa)	d_{ave} (μm)	$Hv_{0.3kg}$ (GPa)
Individual measurements	12.21	36.64	12.67	34.02	12.89	32.85
	12.18	36.79	12.23	36.52	12.18	36.79
	12.50	34.96	12.08	37.43	12.29	36.13
	12.24	36.43	12.67	34.00	12.66	34.08
	12.21	36.64	12.71	33.78	12.29	36.16
Average	12.3 ± 0.1	36.3 ± 0.8	12.5 ± 0.3	35.2 ± 1.7	12.5 ± 0.3	35.2 ± 1.7
Combined diagonal length (μm)	12.4 ± 0.3					
Combined hardness (GPa)	35.6 ± 1.5					

Table B4: Hardness vales and diagonal lengths for hot-pressed pure boron suboxide under a 500g load

	Pure B_6O (hot-P) 1		Pure B_6O (hot-P) 2		Pure B_6O (hot-P) 3	
	d_{ave} (μm)	$Hv_{0.5kg}$ (GPa)	d_{ave} (μm)	$Hv_{0.5kg}$ (GPa)	d_{ave} (μm)	$Hv_{0.5kg}$ (GPa)
Individual measurements	16.52	33.33	16.09	35.16	16.51	33.39
	16.04	35.38	16.08	35.20	15.90	36.00
	16.66	32.77	16.23	34.55	16.69	32.65
	16.41	33.80	15.93	35.87	16.37	33.96
	16.84	32.09	16.59	33.05	16.28	34.32
Average	16.5 ± 0.3	33.5 ± 1.2	16.2 ± 0.3	35.8 ± 1.1	16.4 ± 0.3	34.1 ± 1.3
Combined diagonal length (μm)	16.3 ± 0.3					
Combined hardness (GPa)	34.1 ± 1.2					

Table B5: Hardness vales and diagonal lengths for hot-pressed pure boron suboxide under a 1kg load

	Pure B_6O (hot-P) 1		Pure B_6O (hot-P) 2		Pure B_6O (hot-P) 3	
	d_{ave} (μm)	Hv_{1kg} (GPa)	d_{ave} (μm)	Hv_{1kg} (GPa)	d_{ave} (μm)	Hv_{1kg} (GPa)
Individual measurements	25.97	26.97	23.17	33.89	23.54	32.83
	24.66	29.91	22.85	34.84	24.08	31.39
	23.05	34.25	24.10	31.32	24.52	30.27
	24.94	29.26	25.99	26.93	23.81	32.10
	25.67	27.62	22.91	34.67	24.55	30.20
Average	24.9 ± 1.1	29.6 ± 2.9	23.8 ± 1.3	32.3 ± 3.3	24.1 ± 0.4	31.4 ± 1.2
Combined diagonal length (μm)	24.3 ± 1.1					
Combined hardness (GPa)	31.1 ± 2.7					

Table B6: Hardness vales and diagonal lengths for hot-pressed pure boron suboxide under a 2kg load

	Pure B_6O (hot-P) 1		Pure B_6O (hot-P) 2		Pure B_6O (hot-P) 3	
	d_{ave} (μm)	Hv_{2kg} (GPa)	d_{ave} (μm)	Hv_{2kg} (GPa)	d_{ave} (μm)	Hv_{2kg} (GPa)
Individual measurements	37.51	25.86	37.55	25.81	35.55	28.80
	36.52	27.29	35.95	28.16	37.30	26.15
	37.63	25.69	33.51	32.40	33.84	31.78
	35.38	29.07	37.13	26.40	36.70	27.02
	34.00	31.48	36.83	26.83	36.72	26.98
Average	36.2 ± 1.5	27.9 ± 2.4	36.2 ± 1.6	27.9 ± 2.7	36.0 ± 1.4	28.2 ± 2.3
Combined diagonal length (μm)	36.1 ± 1.4					
Combined hardness (GPa)	28.0 ± 2.2					

B-2 Hardness and IFT results

In Tables B-7 to B-11, the measurements made during testing the composites for hardness and indentation fracture toughness are recorded. The method used for the measurements is described in Sections 3.11 and 3.12.

Table B7: Hardness measurements for pure boron suboxide

d_1 (μm)	d_2 (μm)	a_1 (μm)	a_2 (μm)	Hv_1 (GPa)	K_{Ic} ($MPa.m^{0.5}$)
25.36	26.23			27.34	
25.12	23.97			30.20	
24.57	23.75			31.17	
26.42	25.69			26.80	
23.96	24.83			30.57	
			Average	29.2	
			Std. dev.	2.0	

Table B8: Hardness and IFT measurements for B_6O – 1.16NiO

d_1 (μm)	d_2 (μm)	a_1 (μm)	a_2 (μm)	Hv_1 (GPa)	K_{Ic} ($MPa.m^{0.5}$)
67.02	67.13	187	191	20.22	4.32
67.41	66.22	191	184	20.37	4.36
67.47	68.11	217	224	19.79	3.46
60.67	60.80	181	206	24.66	3.78
61.22	61.88	212	204	24.01	3.43
			Average	21.8	3.9
			Std. dev.	2.3	0.5

Table B9: Hardness and IFT measurements for B_6O – 1.13CaO

d_1 (μm)	d_2 (μm)	a_1 (μm)	a_2 (μm)	Hv_1 (GPa)	K_{Ic} (MPa.$m^{0.5}$)
58.76	59.36	178	198	26.08	3.87
66.67	62.08	185	172	21.95	4.56
59.73	60.35	188	194	25.23	3.84
65.4	66.9	208	199	20.79	3.85
64.32	64.22	189	159	22.02	4.73
			Average	23.2	4.2
			Std. dev.	2.3	0.4

Table B10: Hardness and IFT measurements for B_6O – 1.54Y_2O_3 – 1.45Al_2O_3

d_1 (μm)	d_2 (μm)	a_1 (μm)	a_2 (μm)	Hv_1 (GPa)	K_{Ic} (MPa.$m^{0.5}$)
69.2	68.86	199	179	19.09	4.47
69.39	68.92	203	194	19.02	4.16
65.02	64.85	193	181	21.57	4.27
66.78	66.05	205	186	20.62	4.09
64.43	64.98	230	205	21.73	3.40
67.52	67.75	215	179	19.88	4.12
			Average	20.3	4.1
			Std. dev.	1.2	0.4

Table B11: Hardness and IFT measurements for $B_6O - 1.57Y_2O_3 - 1.49Al_2O_3 - 18.69TiB_2$

d_1 (μm)	d_2 (μm)	a_1 (μm)	a_2 (μm)	Hv_1 (GPa)	K_{Ic} (MPa.m$^{0.5}$)
56.32	55.83	204	184	28.93	3.49
58.9	58.65	227	199	26.33	3.19
63.42	64.32	212	207	22.30	3.56
64.27	63.41	221	201	22.32	3.52
56.11	56.26	194	207	28.81	3.34
			Average	25.7	3.4
			Std. dev.	3.3	0.2

B-3 SEVNB results

In Tables B-12 through to B-17, the results for the SEVNB tests are recorded. The method of testing is described in Section 3.16. Compositions quoted are in volume percent. The Equations used for calculating the toughness of the boron suboxide based ceramics are:

$$K_{Ic} = \frac{F \cdot S}{B \cdot W^{1.5}} \cdot \frac{3\sqrt{\alpha}}{2} Y^*$$

$$Y^* = 1.964 - 2.837\alpha + 13.71\alpha^2 - 23.25\alpha^3 + 24.13\alpha^4$$

$$\alpha = \frac{A}{W}$$

Two sets of sample made of pure B_6O were tested. The two sets differed in the pressure that was applied during sintering. One of the samples was sintered under a load of 50MPa and the other 70MPa. In Table 12 below, they are marked as B_6OP5 and B_6OP7 respectively.

Table B12: SEVNB data for pure B_6O

Disc	Sample	a (μm)	W (mm)	a/w	B (mm)	Y	Load (N)	K_{Ic} ($MPa.m^{0.5}$)
B_6OP5	1	1078	4.35	0.248	3.00	1.840	34.76	1.11
	2	975	4.29	0.227	3.05	1.819	50.35	1.52
	3	913	4.20	0.217	3.12	1.810	53.16	1.58
	4	1058	4.18	0.253	3.09	1.846	39.20	1.30
	5	964	4.22	0.228	3.10	1.820	40.41	1.24
							Average	1.4
							Std dev.	0.2
B_6OP7	1	966	4.24	0.228	3.08	1.819	50.41	1.55
	2	1004	4.35	0.231	3.01	1.822	34.95	1.06
	3	983	4.02	0.245	3.08	1.837	39.85	1.38
	4	1010	3.96	0.255	3.00	1.849	34.76	1.30
							Average	1.32
							Std dev.	0.2
							Overall average	1.3
							Overall std. dev	0.2

Table B13: SEVNB data for $B_6O - 1.54Y_2O_3 - 1.45Al_2O_3$

Sample	a (μm)	W (mm)	a/w	B (mm)	Y	Load (N)	K_{Ic} ($MPa.m^{0.5}$)
1	1125	3.86	0.291	3.11	1.900	51.67	3.20
2	1116	3.86	0.289	3.02	1.897	53.51	3.39
3	1078	3.93	0.274	3.11	1.874	58.38	3.37
4	1081	3.84	0.281	3.10	1.884	62.47	3.80
5	1123	3.88	0.289	3.13	1.897	63.84	3.87
6	1082	3.95	0.274	2.97	1.874	57.08	3.42
7	1209	4.01	0.302	2.95	1.917	58.07	3.67
8	1035	4.08	0.254	2.89	1.847	60.54	3.36
9	1192	3.94	0.303	3.03	1.919	62.58	3.97
10	996	3.84	0.260	2.89	1.854	59.69	3.70
						Average	3.6
						Std dev.	0.3

Table B14: SEVNB data for $B_6O - 1.57Y_2O_3 - 1.49Al_2O_3 - 18.69TiB_2$

Sample	a (µm)	W (mm)	a/w	B (mm)	Y	Load (N)	K_{Ic} ($MPa.m^{0.5}$)
1	1129	4.05	0.279	3.12	1.881	51.34	2.86
2	1064	4.01	0.265	3.11	1.862	49.71	2.71
3	959	3.99	0.240	3.05	1.832	49.69	2.61
4	959	4.04	0.238	3.04	1.829	63.17	3.25
5	1154	4.12	0.280	3.09	1.883	58.73	3.23
6	1158	4.03	0.287	3.12	1.893	49.61	2.83
7	1026	4.08	0.251	3.14	1.844	51.78	2.63
8	1043	4.04	0.258	3.05	1.852	55.63	3.01
9	870	3.97	0.219	3.05	1.812	56.56	2.83
10	1129	4.05	0.279	3.12	1.881	51.34	2.86
						Average	2.9
						Std dev.	0.2

Table B15: SEVNB data for B_6O – 1.13CaO

Sample	a (μm)	W (mm)	a/w	B (mm)	Y	Load (N)	K_{Ic} ($MPa.m^{0.5}$)
1	1398	3.93	0.356	3.13	2.030	37.38	2.65
2	1438	3.89	0.370	3.07	2.065	31.10	2.36
3	1149	4.22	0.272	3.16	1.871	46.04	2.34
4	1127	4.11	0.274	3.11	1.874	54.36	2.93
5	1133	4.01	0.283	3.17	1.887	47.71	2.68
6	1351	4.12	0.328	3.06	1.967	46.95	2.95
7	1161	3.89	0.298	3.10	1.912	46.00	2.87
8	1260	3.99	0.316	3.06	1.944	35.16	2.24
						Average	2.6
						Std dev.	0.3

Table B5: SEVNB data for B_6O – 1.16NiO

Disc	Sample	a (μm)	W (mm)	a/w	B (mm)	Y	Load (N)	K_{Ic} ($MPa.m^{0.5}$)
1	1	874	4.05	0.216	3.04	1.809	47.92	2.31
	2	836	4.10	0.204	3.13	1.800	49.81	2.22
	3	1287	4.15	0.310	3.03	1.932	49.57	2.96
	4	1002	4.19	0.239	3.02	1.831	48.23	2.37
	5	952	4.18	0.228	3.03	1.819	61.68	2.94
	6	833	4.06	0.205	2.94	1.801	49.60	2.39
	7	967	4.06	0.238	3.03	1.829	52.11	2.67
	8	1029	4.05	0.254	3.12	1.847	52.61	2.73
	9	1096	4.01	0.273	3.15	1.873	47.39	2.60
							Average	2.6
							Std dev.	0.3
2	1	970	4.18	0.232	3.18	1.824	61.47	2.84
	2	1142	4.24	0.269	3.18	1.867	49.60	2.46
	3	992	4.16	0.238	3.15	1.830	49.54	2.35
	4	1087	4.21	0.258	3.18	1.852	55.03	2.69
	5	1437	4.22	0.340	3.17	1.994	46.47	2.79
	6	1133	4.21	0.269	3.20	1.867	47.96	2.39
	7	941	4.19	0.224	3.18	1.816	48.21	2.16
							Average	2.5
							Std dev.	0.3
						Overall average		2.6
						Overall std. dev		0.3

B-4: Crack opening displacement

Analysis of the crack opening displacement (COD) of boron suboxide based materials was performed in accordance to Section 3.15. The formulae used to calculate the intended fracture toughness are:

$$\frac{\delta}{K} = \frac{\sqrt{b}}{E'}\left(\sqrt{\frac{8}{\pi}\frac{x}{d}} + A_1\left(\frac{x}{d}\right)^{3/2} + A_2\left(\frac{x}{d}\right)^{5/2}\right)$$

$$A_1 \cong 11.7\exp[-2.063(a/d-1)^{0.28}] - \frac{0.898}{a/d-1}$$

$$A_2 \cong 44.5\exp[-3.712(a/d-1)^{0.28}] - \frac{1}{(a/d-1)^{3/2}}$$

For the Y_2O_3-Al_2O_3-B_6O composite, the calculated fracture toughness is 4.3MPa.$m^{0.5}$, with a R^2 fit of 76.5%. Figure B1 shows the COD analysis of the composite. Each of the colours represents a different crack.

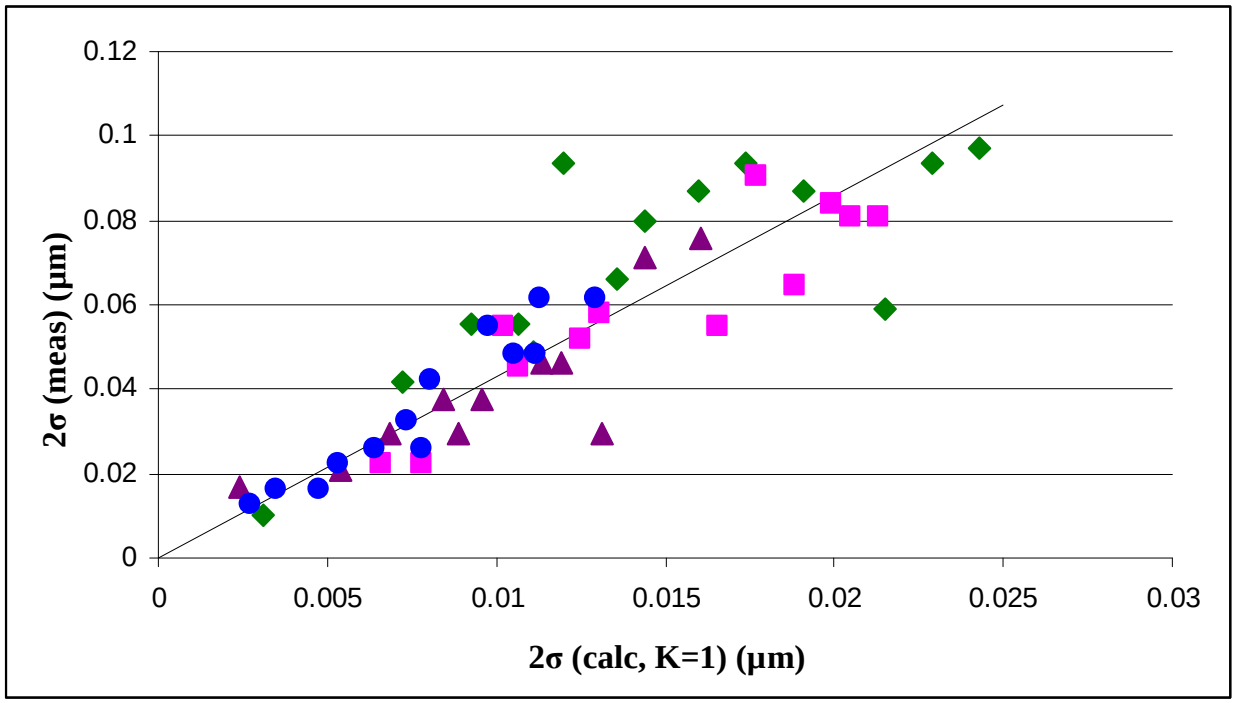


Figure B1: COD analysis for B_6O-Y_2O_3-Al_2O_3

Figure B2 is the COD analysis for the B_6O-NiO composite. The fitted fracture toughness is 4.1MPa.$m^{0.5}$. The R^2 value for the fit is 89.5%. Each of the colours represents a different crack.

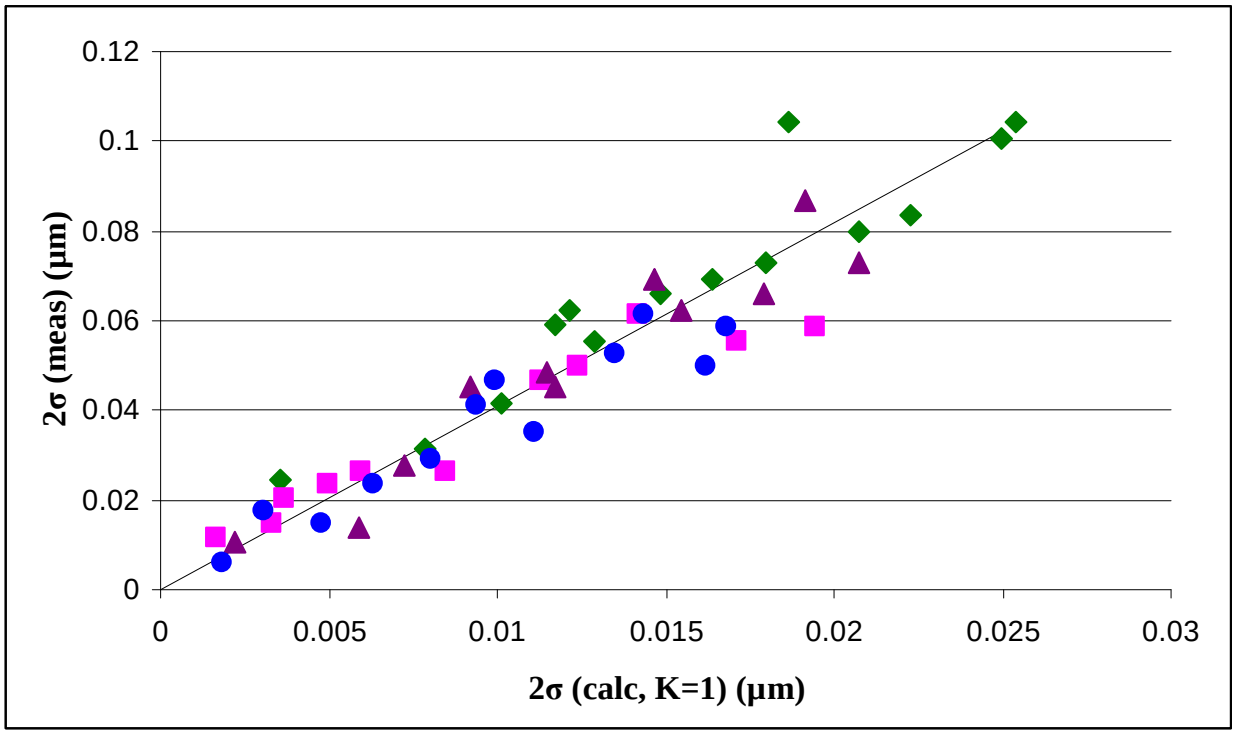


Figure B2: COD analysis for B_6O-NiO

The COD analysis for B_6O-CaO is shown in Figure B3. The calculated fracture toughness for this material is 3.6MPa.m$^{0.5}$, with a R^2 fit of 88.5%. Each of the colours represents a different crack.

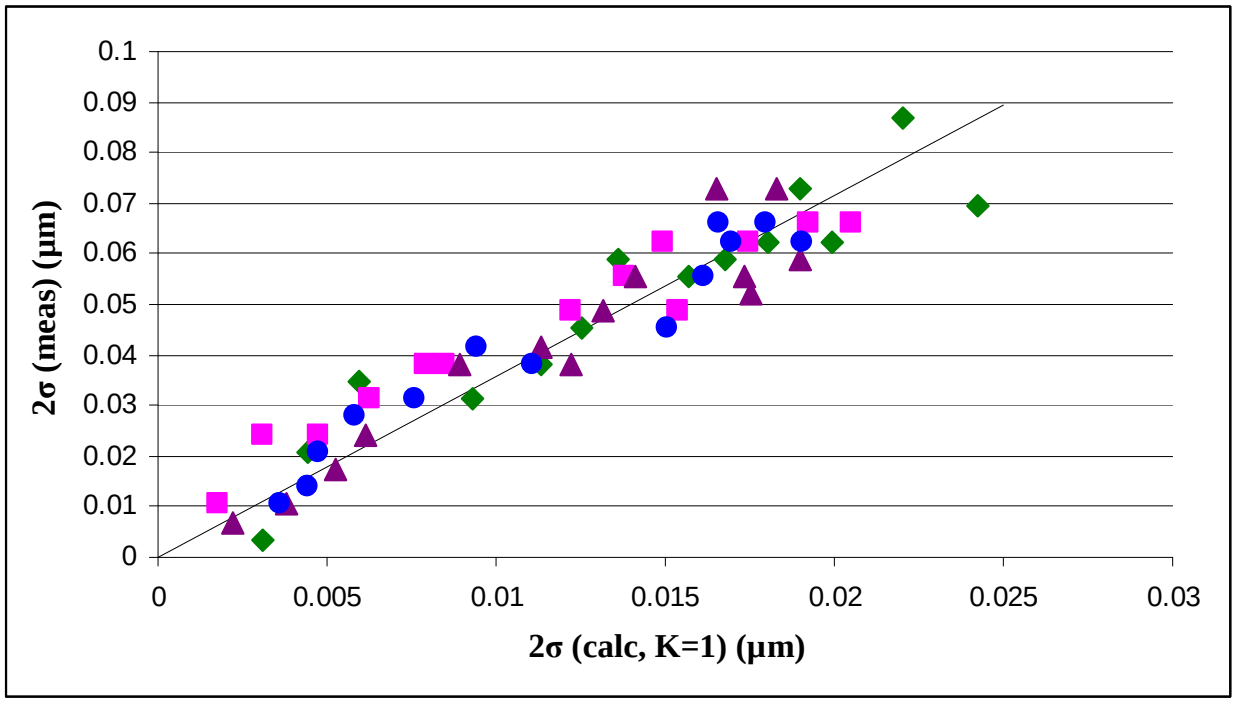


Figure B3: COD analysis for B_6O-CaO

Figure B4 is the COD analysis for the B_6O Y_2O_3-Al_2O_3-TiB_2composite. From the gradient of the curve the fracture toughness of the composite, measured by the COD analysis is 2.9MPa.$m^{0.5}$. The fit of the curve (R^2) was calculated to be 69.8%. Each of the colours represents a different crack.

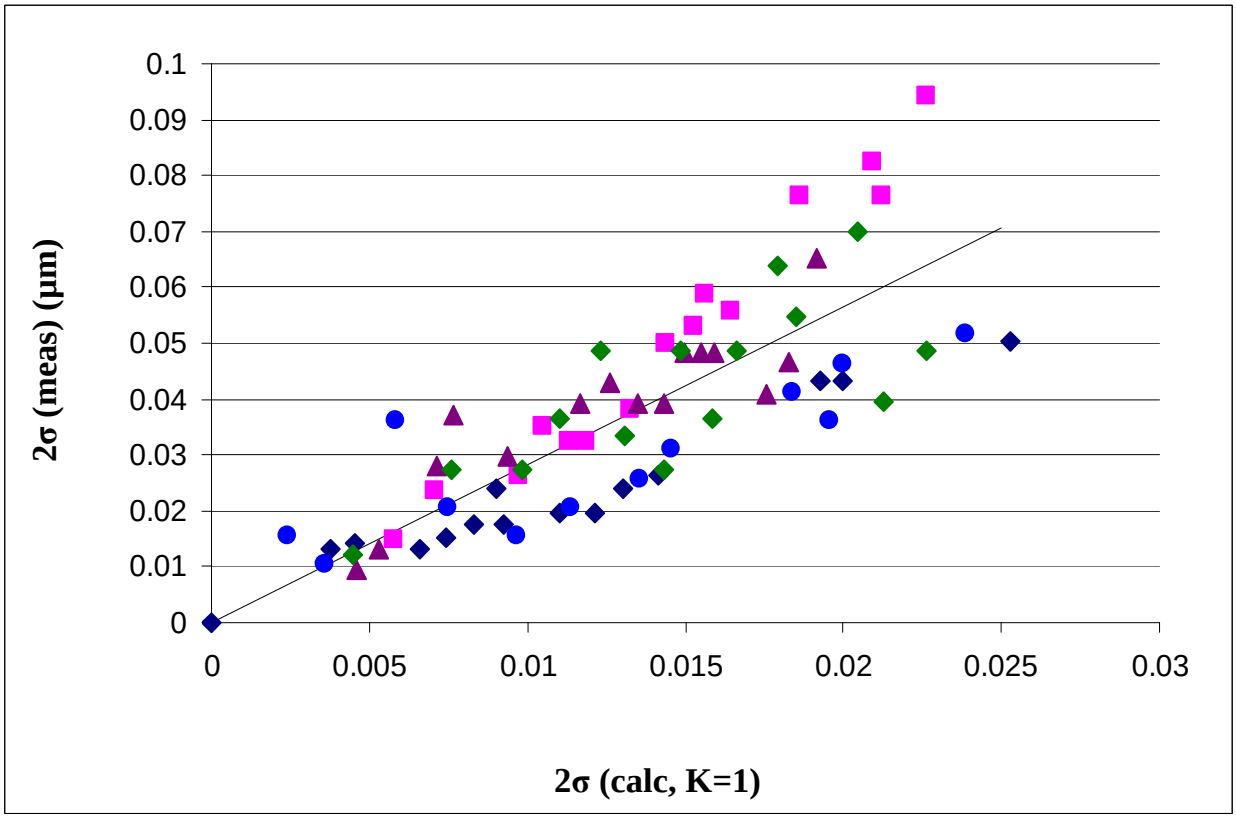


Figure B4: COD analysis for theTiB_2-Y_2O_3-Al_2O_3 –B_6O composite. $K_{Ic,\ COD}$ = 2.8MPa.$m^{0.5}$

Appendix C:

C-1: Lattice parameters:

From the XRD traces of the boron suboxide materials, the lattice constants were calculated using linear regression. Due to a limited number of boron suboxide peaks available in the B_6O-Y_2O_3-Al_2O_3-TiB_2 sample, it was not possible to determine the lattice constants for this material. No angular correction was done.

Table C1: Lattice constants for the boron suboxide materials.

	a (Å)	**error a (Å)**	**c (Å)**	**error c (Å)**	**c/a**
B_6O	5.380	0.005	12.333	0.009	2.292
B_6O-CaO	5.398	0.007	12.351	0.006	2.288
B_6O-Y_2O_3-Al_2O_3	5.344	0.004	12.279	0.006	2.298
B_6O-NiO	5.413	0.012	12.332	0.015	2.278